2014

Large Area Conformal Infrared Frequency Selective Surfaces

Jeffrey D'Archangel
University of Central Florida

LARGE AREA, CONFORMAL INFRARED FREQUENCY SELECTIVE SURFACES

by

JEFFREY ALLEN D' ARCHANGEL
B.S. Saginaw Valley State University, 2009
M.S. University of Central Florida, 2011

A dissertation submitted in partial fulfillment of the requirement
for the degree of Doctor of Philosophy
in the College of Optics and Photonics: CREOL & FPCE
at the University of Central Florida
Orlando, Florida

Fall Term
2014

Major Professor: Glenn D. Boreman

ABSTRACT

Frequency selective surfaces (FSS) were originally developed for electromagnetic filtering applications at microwave frequencies. Electron-beam lithography has enabled the extension of FSS to infrared frequencies; however, these techniques create sample sizes that are seldom appropriate for real world applications due to the size and rigidity of the substrate. A new method of fabricating large area conformal infrared FSS is introduced, which involves releasing miniature FSS arrays from a substrate for implementation in a coating. A selective etching process is proposed and executed to create FSS particles from crossed-dipole and square-loop FSS arrays. When the fill-factor of the particles in the measurement area is accounted for, the spectral properties of the FSS flakes are similar to the full array from which they were created. As a step toward scalability of the process, a square-patch design is presented and formed into FSS flakes with geometry within the capability of ultraviolet optical lithography.

Square-loop infrared FSS designs are investigated both in quasi-infinite arrays and in truncated sub-arrays. First, scattering-scanning near-field optical microscopy (s-SNOM) is introduced as a characterization method for square-loop arrays, and the near-field amplitude and phase results are discussed in terms of the resonant behavior observed in far-field measurements. Since the creation of FSS particles toward a large area coating inherently truncates the arrays, array truncation effects are investigated for square-loop arrays both in the near- and far-field. As an extension of the truncation study, small geometric changes in the design of square-loop arrays are introduced as a method to tune the resonant far-field wavelength back to that of the quasi-infinite arrays.

To my children, Heaven and Maxwell.

ACKNOWLEDGMENTS

My tenure as a doctoral student and candidate has been quite rewarding under the leadership of Dr. Glenn Boreman. I am grateful for his mentorship as well as his compassion during a few difficult personal times. I appreciate that Dr. Winston Schoenfeld agreed to chair my dissertation committee and also acknowledge that his laboratory class in clean room fabrication was a significant help in my research. I also acknowledge the rest of my dissertation committee, Dr. Patrick LiKamWa, Dr. Pieter Kik, and Dr. Brian Lail for stimulating discussions concerning my work as well as other research topics.

I am thankful for the guidance and camaraderie of past and current members of our research group, the Infrared Systems Laboratory. For their efforts to bring me up to speed on various fabrication processes, simulations, and characterization methods, I thank Dr. Jeffrey Bean, Dr. Brian Slovick, Lt. Col. Louis Florence, Alex Dillard, Dr. Peter Krenz, Dr. David Shelton, Dr. James Ginn, Dr. Samuel Wadsworth, and Dr. Ed Kinzel. For their helpful discussions and critical contributions to my work, I thank Dr. Eric Tucker and Robert Brown.

My background in Electromagnetics and Mathematics upon entering graduate school has been significant toward success in the academic hurdles of my doctoral program. Foremost, I acknowledge Dr. Hsuan "Frank" Chen at Saginaw Valley State University for his tutelage in Optics; his lectures and experimental training have been instrumental in my academic achievements. There are several other Professors at Saginaw Valley State University as well as Delta College whom I thank for their contributions to my understanding of the subjects relating

to Optics: these are Dr. Marian Shih and Dr. Michael Faleski in Physics, Dr. Jonathan Leonard in Electrical Engineering, Prof. David Redman in Mathematics, and Prof. Hideki Kihata in Photography.

As an undergraduate student, I spent over two years working in Research and Development at the Dow Chemical Company, which left me well-prepared for the thin film fabrication and characterization that would take place in my graduate research. I am forever indebted to Dr. Mark Bernius for creating this opportunity, and also for strengthening my research skills by allowing me to take the lead on several optical sensing projects. Additionally, I thank Dr. Melissa Mushrush, Dr. Rebekah Feist, Doug Wirsing, Jeff Mitchell, Dr. Simon Yeung, Dr. Buford Lemon, Bob Haley, Dr. Beth Nichols, Dr. Jennifer Gerbi, Dr. Joseph George, Dr. Rentian Xiong, and Emily Hill for their friendship, assistance with learning fabrication and characterization techniques, and advice concerning graduate school during my time at Dow.

In 2011, I was awarded the SMART Scholarship, which is funded by the United States Department of Defense and administered by the American Society for Engineering Education. I wholeheartedly thank all who were involved in choosing me for this prestigious honor. In particular, I am grateful to Dr. Jose Colon who saw my potential as a government scientist and initially acted as my mentor in the program.

In 2012, I moved to the University of North Carolina at Charlotte to continue my research in the Infrared Systems Laboratory, while remaining a student in the CREOL program at the University of Central Florida. The technical and administrative staff in Charlotte has treated me like one of their own students, and I am quite grateful for this. In particular, kind assistance from Scott Williams, Erik LaRuffa, Dr. Lou Deguzman, Dr. Robert Hudgins, and Mark Clayton is

acknowledged. Back at the University of Central Florida, I would like to thank several people who helped with my continuity as a CREOL student; these include Rachel Franzetta, Matthew Petrone, Dr. Winston Schoenfeld, and Dr. David Hagan. Additionally, I express my gratitude to the SMART Program Office for being understanding of the necessity for my relocation.

Ten years ago, I was a pizza delivery guy without much prospect of ever becoming anything else. I thank God for bringing direction to my life. I express gratitude to the only two people who supported and believed in me back then, when I had the random and crazy idea to go back to college: my wife Brandi and my grandmother Ruth.

Finally, with all my being, I recognize the hard work, patience, and unconditional love of my wife over the past five years. Without her efforts, none of my accomplishments would have been even remotely possible. I acknowledge the fact that she has unselfishly put many of her wants and aspirations aside such that I may focus on advancing my career. I look forward to returning the favor.

TABLE OF CONTENTS

LIST OF FIGURES

LIST OF ACRONYMS

AFM	atomic force microscope
BCB	benzocyclobutene
BOE	buffered oxide etch
CAD	computer-aided design
DDR	diffuse component of directional reflectance
FEM	finite-element method
FSS	frequency selective surface
FTIR	Fourier transform infrared
FWHM	full width at half maximum
HDR	hemispherical directional reflectance
HFSS	high frequency structure simulator
IPA	isopropyl alcohol
IR-VASE	infrared variable angle spectroscopic ellipsometry
KOH	potassium hydroxide
LWIR	long wave infrared
MCT	mercury cadmium telluride
MIBK	methyl isobutyl ketone
NMP	N-methyl pyrrolidinone
OAP	off-axis parabola
PEC	perfect electrical conductor

PMMA	poly(methyl methacrylate)
RF	radio frequency
RIE	reactive ion etch
RPM	revolutions per minute
RTA	rapid thermal annealer
SDR	specular component of directional reflectance
SEM	scanning electron microscope
s-SNOM	scattering-scanning near-field optical microscope
TE	transverse electric
TM	transverse magnetic
VASE	variable angle spectroscopic ellipsometry

CHAPTER ONE: INTRODUCTION

This dissertation presents current research in frequency selective surfaces (FSS), which are patterned structures that have been previously studied due to their resonance at microwave, and more recently, optical frequencies. The engineered resonant properties afforded by FSS lead to abundant utility as selective electromagnetic filters with frequency dependent transmissivity, reflectivity, and absorptivity. Size limits placed on the total area of infrared FSS samples due to fabrication methods severely restrict the potential field of applications. As a prospective solution, this dissertation explores the possibility of creating a large area, conformal coating comprised of miniature infrared FSS arrays. The fabrication process is thoroughly explored, as well as the changes in spectral resonances that are characteristic of array truncation. Overall, a design – fabricate – test methodology is adopted, leading to a systematic progression of the investigative research and the conclusions drawn from the work.

The structure of this dissertation is as follows. This introductory chapter familiarizes the reader with the concept of FSS, the extension of their utility from radio frequency (RF) to optical frequencies, and the motivation for the creation of a large area conformal infrared FSS coating, which is the topic of this dissertation. Chapter Two details the approach taken to the research performed in preparation of this dissertation, including the design and simulation via finite-element modeling (FEM), fabrication by various thin-film processing and lithographic techniques, and characterization by both near- and far-field instrumentation. Chapter Three presents seminal results showing the feasibility of the flake-based approach to create a large area

coating; both the fabrication procedure and spectral characterization of the flakes and full array are discussed. In Chapter Four, square-loop arrays, an FSS design often employed in the this dissertation, are investigated both in the near-field using scattering-scanning near-field optical microscopy (s-SNOM) and in the far-field using Fourier transform infrared (FTIR) spectroscopy. Chapter Five describes an investigation into array truncation effects in square-loop infrared FSS, which is relevant to the idea of a flake-based coating because the creation of flakes inherently truncates the arrays. As an extension to the results presented in Chapter Five, Chapter Six presents finite FSS designs that are modified geometrically in an attempt to reduce the effects of truncation on the far-field spectral response of truncated arrays. Since fabrication by electron-beam lithography is very slow and expensive, Chapter Seven presents square-patch FSS particles released from an array with dimensions which can be reproduced by optical-projection lithography, a much faster and cheaper approach. This dissertation concludes with Chapter Eight, which summarizes the presented research and closes with a discussion of future work.

1.1 Introduction to Frequency Selective Surfaces

Frequency selective surfaces are typically considered a planar arrangement comprised of unit cell elements with periodicity in two dimensions. The unit cell elements are either conductive structures or apertures within a conductive layer. Early on, FSS were studied at RF in the form of perforated conductive sheets [1, 2, 3] or arrays of conductive plates [4, 5]. An original application of FSS was to reduce the radar cross section of antennas at frequencies outside their band of operation [6]. To that end, FSS were investigated for radome design [7, 8]. Wire grids and metal meshes for use at infrared frequencies were introduced around the same time as the advent of FSS. In most cases, the terms *wire grid* and *metal mesh* refer to structures that can be considered synonymous with FSS. Wire grids were shown to be useful as far infrared

filters [9, 10] as well as polarizers in the far-infrared [11] and even near-infrared [12]. Metal meshes were studied as mirrors for far-infrared lasers [13, 14] and for interferometric applications [15].

Frequency selective surfaces possess resonant properties, which vary according to the geometry of the conductive or aperture elements, the inter-element spacing, and the material properties of the elements and surrounding medium. As a brief example of this resonant behavior, a square-loop array design with resonant properties at RF will be presented. Figure 1 shows a square-loop unit cell; the FSS array consists of a plurality of these unit cells extending along the x and y axes. As can be seen in the figure, the square loop is surrounded in a medium which appears as a transparent box. In this case, the square loop is defined as a perfect electrical conductor (PEC), while the surrounding medium is vacuum. This figure is taken directly from a simulation in Ansys high frequency structural simulator (HFSS), which is the electromagnetic modeling tool used in this dissertation, discussed in detail in later chapters. In this particular simulation, the PEC loop is defined as a square with sides 5 mm long, with a periodicity of 15 mm. The thickness (0.01 mm) and line width (0.01 mm) of the loop are purposely made very small with respect to the design wavelength.

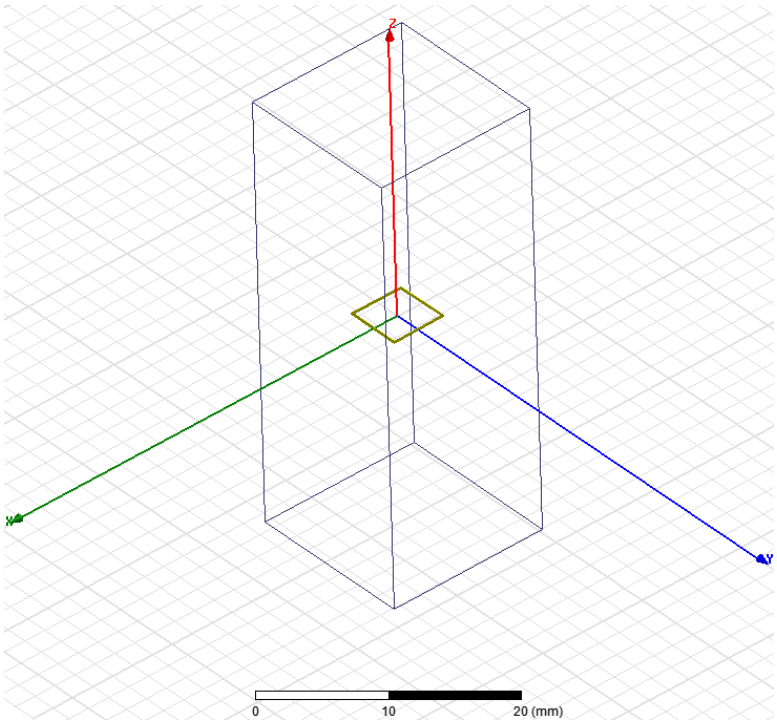

Figure 1. Unit cell design for a square-loop FSS array, taken from Ansys HFSS.

The simulated spectral results of the square-loop design portrayed in Figure 1 are shown in Figure 2. The values plotted in the figure correspond to the power transmitted through and reflected by the FSS structure as a function of wavelength. The FSS is observed to have a resonant condition at wavelengths near 18.5 mm, as can be inferred from the sharp drop in transmitted power along with the sharp increase in reflected power. Such is the characteristic response of an RF FSS composed of conductive elements; at resonance, high current distributions mimic a metallic sheet [16]. It is noted that if the conductive loop were replaced by an aperture of the same size within a thin conductive sheet, the resonant condition would invert via the principle of Babinet, corresponding to a sharp rise in the power transmitted along with a sharp drop in the power reflected. Figure 2 is plotted with units of wavelength on the abscissa to highlight the strong correlation between the perimeter of the square loop (20 mm) and the

resonant wavelength (~18.5 mm), which approaches equality in this example because the square-loop elements are treated as PEC and are suspended in free space. The slight deviation between the perimeter and the resonant wavelength is because the conductive element has finite thickness and width, and is placed within an infinite array.

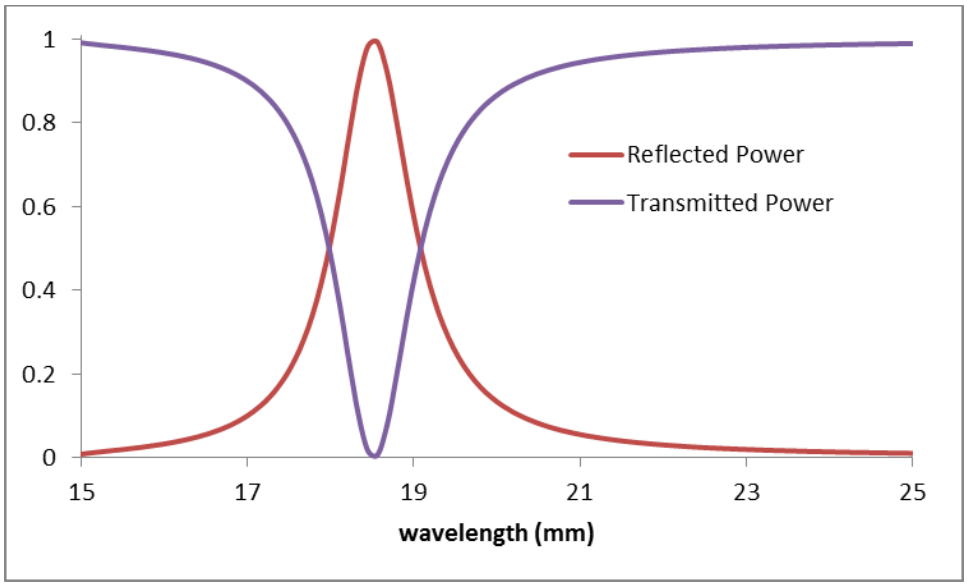

Figure 2. Simulated spectral response in terms of reflected and transmitted power for the structure shown in Figure 1.

The electromagnetic resonance characteristic of FSS yields a spectral response that is different from that which can be found in nature or created by planar thin films. In recent times, prominent research has been carried out in the field of metamaterials. The term *metamaterial* refers to artificial materials that have been engineered with an electromagnetic response attributed to sub-wavelength structure. Recently, the term *metasurface* has been coined for planar metamaterial surfaces which are thin with respect to the design wavelength [17, 18, 19]. Since FSS possess resonance based on sub-wavelength geometry, and this resonance is different than

would be provided by the material properties of the constituent films, FSS are considered analogous to metasurfaces in many communities [20, 21, 22, 23, 24, 25, 26].

1.2 Frequency Selective Surfaces at Infrared

Given the previous success of FSS as RF filters, the dimensions were scaled down for resonance in the infrared. While RF FSS are typically fabricated with metal foil etching or electroplating, these methods were not feasible for infrared applications due to the finite pattern resolution. The decreased dimension sizes afforded by modern lithography techniques such as electron-beam lithography allowed FSS to be fabricated as resonant structures at infrared frequencies.

Dipole arrays were fabricated with resonance in the near and mid infrared and variations in element size, periodicity, and substrate were investigated with respect to the resonant response [27, 28, 29, 30]. More complicated FSS structures were investigated with resonance in the near and mid infrared as well, such as crossed-dipole arrays [30, 31, 32], tripole arrays [31] crossed-slot arrays [32, 33, 34], and square-loop arrays [35], among many others. Additionally, the use of meander line polarizers, another RF FSS structure, was extended into the mid infrared as an alternative to standard quarter wave plate polarizers [36, 37, 38]. In addition to their use as filters, FSS at near and mid infrared frequencies have been used to generate polarized emission [39, 40], alter the reflected phase in tunable reflectarrays [23], and modify the emissivity of blackbody sources [24].

Infrared FSS tend to borrow heavily from the standard FSS designs; however, they behave differently than the RF counterparts due to the differences in material properties between the regimes. Conductors at RF can often be assumed as PEC, while at infrared they possess finite

conductivity, which must be accounted for in the modeling. Furthermore, the metal properties are dispersive at infrared such that frequency dependence of the conductivity must be included in the simulations to obtain predictive results. Dielectrics tend to be transparent at RF, while at infrared most dielectric materials possess strong absorption bands, again leading to optical properties that must be included in the modeling. Overall, the dispersive optical properties of materials at infrared lead to wider bandwidth of FSS resonance [26] and a much higher degree of absorptivity at resonance due to propagation within the skin depth of the metallic components in the FSS geometry [41].

1.3 Motivation for Large Area, Conformal Infrared Frequency Selective Surfaces

As the techniques required to create infrared FSS rely heavily on microelectronics processing equipment, infrared FSS are usually fabricated upon standard semiconductor wafers. This restricts the field of possible applications because of the small size and rigid nature of the wafer substrates. Thus, the standard fabrication processes yield FSS samples that are not only relatively small in area but are also rigid and thus can only be utilized in planar surface applications. Such sample sizes are likely to be acceptable for the enhancement of small devices and as components in optical systems with relatively small beams, but not for large-scale applications. The advancement of large-scale applications using infrared FSS depends highly upon the ability to incorporate them into large-scale conformal coatings.

There exists only a limited number of ways for a large area, conformal FSS-based spectrally engineered coating to be applied to an object. First, a sheet could be fabricated which could be laid on or wrapped around the object. Additionally, small FSS particles could be manufactured which are adhered to the object (the route taken in this dissertation). Lastly, the coating could be self-assembled on the object itself. It is noted that the last of these routes toward

application is currently unfeasible for large and arbitrary structures, as self-assembly techniques have only been shown at small scales and often require surface treatments such as patterning or templating beforehand.

Fabrication of FSS on flexible substrates, which may theoretically be attached or wrapped around arbitrary objects, has been demonstrated at the laboratory scale. Here, FSS and associated structures have been fabricated upon flexible polyimide films [42, 43, 44], polyethylene naphthalate films [45], and polypropylene films [46], as well as upon freestanding silicon nitride membranes [47]. It is important to note that these examples have been shown at the laboratory scale, and in most cases have required wafer fabrication and subsequent removal to create the final flexible samples. While flexible, these FSS are still small compared to the required surface areas for large area applications. It is noted that with the current interest in wearable RF-type structures, it is very possible that infrared FSS or related structures will be shown in textiles soon, offering another example of a wrapping-type conformal, large area solution. Additionally, roll-to-roll nano-imprint technology should offer additional demonstrations of flexible large area, conformal FSS (or related structures) in the near future.

A new method to produce large-scale conformal FSS-based coatings will be described in detail in this dissertation. This approach utilizes etching processes to create small particles embedded with finite arrays of FSS elements [48]. It is envisioned that the particles would be dispersed in a binder to be used in a hand-painted or sprayed-on coating. It is noted that a thorough literature search has been conducted on prior research involving the dispersal of sub-arrays or even unit cell particles of FSS or metamaterials; at the time of the writing of this dissertation, no comparably technology exists in the open literature. The binder of choice would ideally be transparent over the infrared spectral band of interest, although absorptivity bands

could presumably be used to enhance the performance. Ultimately, the FSS flakes would likely be randomly oriented in the coating; they could have any resultant angular orientation and could land face-up or face-down. The random angular orientation requires the use of FSS elements and periodicity with symmetry, such that s-polarization and p-polarization can exhibit equal spectral response at normal incidence. Since the FSS particles could land on either side, the fabricated designs must be such that the structure is symmetric about the center plane in the direction normal to the surface to be coated. (If a ground plane and dielectric standoff layer are included in the design, the particles must be fabricated symmetric about the ground plane.) An additional desired criterion is that the angular response of the FSS should be robust with respect to angle of incidence, since a conformal coating is desired.

1.4 Prior Publication Disclosure

Portions of Chapter Three have been published in Ref. 48. Portions of Chapter Four have been published in Ref. 76. Portions of Chapter Five have been published in Ref. 87. Portions of Chapter Seven have been published in Ref. 95.

CHAPTER TWO: RESEARCH APPROACH

This chapter describes the approach taken in the investigative research discussed in this dissertation. In general, the research takes an iterative approach following a continuous process of design, fabrication, and characterization. The design of FSS structures typically begins as a basic FSS unit cell element (such as a crossed-dipole or a square-loop) placed on a substrate, with or without the inclusion of a dielectric standoff layer and ground plane. Designs are then simulated in Ansys HFSS, a full wave electromagnetic solver using FEM. At this point, the designs are optimized via parametric iteration of the geometry, with the typical goal being a strong resonant condition at one or more wavelengths. The next step is the fabrication of the FSS arrays, which relies heavily upon lithographic techniques developed by the microelectronics industry. During the material deposition stages of the fabrication, witness samples are collected such that the optical constants of the thin films constituting the FSS structures can be measured and input directly into the next iteration of the simulation. The final phase of each iteration is experimental characterization. Typically, the results of a successful FSS array are shown by FTIR spectroscopy; however, other techniques such as ellipsometry and s-SNOM often contribute to a greater understanding of the physics involved as well as better corroboration with the electromagnetic simulations.

2.1 Design and Simulation

The simulation of the FSS structures takes place in Ansys HFSS. The geometry is established with a computer-aided design (CAD)-type interface, and the software uses FEM to compute the high frequency electrical behavior of the simulated structures. FSS are normally modeled using the Floquet port method. This method is used solely for the analysis of planar, periodic structures with modal excitation (such as plane wave illumination), and allows the infinite structure to be analyzed by considering only a single unit cell [16, 6]. The unit cell is housed in master and slave boundaries, where the field at the slave boundary is matched to the field at the master boundary, except for the appropriate phase shift occurring with changes in the incident angle of illumination. An integral part of the simulation is the inclusion of frequency dependent optical material properties, due to the finite conductivity of metals as well as the losses and dispersion of dielectrics at infrared frequencies [49, 50]. Previous experience has proven that it is critical to extract the optical properties of the actual deposited layers via ellipsometry. These properties can be fed directly into the simulation [51], greatly increasing the predictive capability since many materials have infrared optical properties that can be significantly affected by detailed processing conditions.

The spectral results of Floquet port models in HFSS are interpreted in terms of the scattering or s-parameters, which are well known in microwave circuit theory. The s-parameters are computed for each Floquet mode that is allowed to propagate. Here, the s-parameters concerning the Floquet modes commonly known as transverse electric (TE) and transverse magnetic (TM) plane waves will be discussed. In the simulations presented in this dissertation, the s-parameters correspond to a two port network, where the incident and reflected fields are thought of in terms of the incoming and outgoing waves. The outgoing waves can be described in terms of the incoming waves as follows.

$$b_1 = a_1 S_{11} + a_2 S_{12} \quad (1)$$

$$b_2 = a_1 S_{21} + a_2 S_{22} \quad (2)$$

Here, a_1 and a_2 are the incoming waves at ports 1 and 2, while b_1 and b_2 are the outgoing waves at ports 1 and 2. The above equations can be arranged in matrix form as follows, in which the s-parameters are expressed in the so-called s-matrix.

$$\begin{bmatrix} b_1 \\ b_2 \end{bmatrix} = \begin{bmatrix} S_{11} & S_{12} \\ S_{21} & S_{22} \end{bmatrix} \begin{bmatrix} a_1 \\ a_2 \end{bmatrix} \quad (3)$$

In the simulations discussed within this dissertation, excitation comes only from the incident side, at port 1, such that a_2 is driven to zero. Thus, S_{11} corresponds to the ratio of the reflected wave b_1 over the incident wave a_1 and S_{21} corresponds to the ratio of the transmitted wave b_2 over the incident wave a_1. By definition, these terms are known in the optics community as the field reflection and transmission coefficients, *r* and *t* respectively.

$$S_{11} = \frac{b_1}{a_1} = r \quad (4)$$

$$S_{21} = \frac{b_2}{a_1} = t \quad (5)$$

The quantities that can be measured directly in the far-field are the reflectivity and the transmissivity of the FSS, which in terms of the s-parameters are given as follows.

$$R = |S_{11}|^2 \quad (6)$$

$$T = |S_{21}|^2 \quad (7)$$

As the s-parameters and derived quantities vary with wavelength, the simulated spectral characteristics are obtained by the inclusion of a discretized frequency sweep at a single angle of incidence.

In much of the work discussed here, the Floquet port method is a sufficient and accurate predictor of the electromagnetic response of infrared FSS. In certain situations however (such as finite FSS array analysis) the Floquet port method consumes greater computational resources than are locally available. Simulations using the Floquet port method utilize the s-parameters to obtain the far-field spectral parameters, such as reflectivity, transmissivity, and absorptivity. For simulations that cannot utilize Floquet ports, this approach is no longer valid. When Floquet ports cannot be used, absorptivity in the structure is calculated by way of the volume loss density, a term that appears in the derivation of Poynting's Theorem. We begin by stating Maxwell's equations in differential form.

$$\nabla \cdot \boldsymbol{D} = \rho \quad (8)$$

$$\nabla \cdot \boldsymbol{B} = 0 \quad (9)$$

$$\nabla \times \boldsymbol{E} = -\frac{\partial \boldsymbol{B}}{\partial t} \quad (10)$$

$$\nabla \times \boldsymbol{H} = \boldsymbol{J} + \frac{\partial \boldsymbol{D}}{\partial t} \quad (11)$$

Here, $\boldsymbol{D}$ denotes the electric flux density, ρ denotes the volume charge density, $\boldsymbol{B}$ denotes the magnetic field intensity, $\boldsymbol{E}$ denotes the electric field intensity, $\boldsymbol{H}$ denotes the magnetic flux density, and $\boldsymbol{J}$ denotes the electric current density. The field quantities are shown in bold to designate them as vector fields. The vector fields appearing in Maxwell's equations are related to each other via the constitutive relations, shown here for the case of isotropic materials.

$$\boldsymbol{D} = \varepsilon \boldsymbol{E} \quad (12)$$

$$\boldsymbol{B} = \mu \boldsymbol{H} \quad (13)$$

$$\boldsymbol{J} = \sigma \boldsymbol{E} \quad (14)$$

Here, ε is the permittivity, μ is the permeability, and σ is the conductivity of the materials that the fields are interacting with.

Poynting's Theorem is derived through manipulation of Maxwell's Equations via vector identities. Equation 10 is dotted by $\boldsymbol{H}$ and Equation 11 is dotted by $\boldsymbol{E}$ as follows.

$$\boldsymbol{H} \cdot \nabla \times \boldsymbol{E} = -\boldsymbol{H} \cdot \frac{\partial \boldsymbol{B}}{\partial t} \quad (15)$$

$$\boldsymbol{E} \cdot \nabla \times \boldsymbol{H} = \boldsymbol{E} \cdot \boldsymbol{J} + \boldsymbol{E} \cdot \frac{\partial \boldsymbol{D}}{\partial t} \quad (16)$$

Equations 15 and 16 can be united, using the vector identity $\nabla \cdot (A \times B) = B \cdot \nabla \times A - A \cdot \nabla \times B$ as follows.

$$\nabla \cdot (\boldsymbol{E} \times \boldsymbol{H}) = \boldsymbol{H} \cdot \nabla \times \boldsymbol{E} - \boldsymbol{H} \cdot \nabla \times \boldsymbol{E} \quad (17)$$

$$\nabla \cdot (\boldsymbol{E} \times \boldsymbol{H}) = -\boldsymbol{H} \cdot \frac{\partial \boldsymbol{B}}{\partial t} - \boldsymbol{E} \cdot \frac{\partial \boldsymbol{D}}{\partial t} - \boldsymbol{E} \cdot \boldsymbol{J} \quad (18)$$

The partial derivative terms in Equation 18 can be manipulated as follows, using the product rule.

$$\boldsymbol{H} \cdot \frac{\partial \boldsymbol{B}}{\partial t} = \frac{1}{2}\mu\left(\frac{\partial \boldsymbol{H}}{\partial t} \cdot \boldsymbol{H} + \boldsymbol{H} \cdot \frac{\partial \boldsymbol{H}}{\partial t}\right) = \frac{\partial}{\partial t}\left(\frac{1}{2}\mu \boldsymbol{H} \cdot \boldsymbol{H}\right) = \frac{\partial}{\partial t}\left(\frac{1}{2}\mu \|\boldsymbol{H}\|^2\right) \quad (19)$$

$$\boldsymbol{E} \cdot \frac{\partial \boldsymbol{D}}{\partial t} = \frac{1}{2}\varepsilon\left(\frac{\partial \boldsymbol{E}}{\partial t} \cdot \boldsymbol{E} + \boldsymbol{E} \cdot \frac{\partial \boldsymbol{E}}{\partial t}\right) = \frac{\partial}{\partial t}\left(\frac{1}{2}\varepsilon \boldsymbol{E} \cdot \boldsymbol{E}\right) = \frac{\partial}{\partial t}\left(\frac{1}{2}\varepsilon \|\boldsymbol{E}\|^2\right) \quad (20)$$

Substituting Equations 19, 20, and 14 into Equation 18 yields the following, after re-arranging.

$$\nabla \cdot (\boldsymbol{E} \times \boldsymbol{H}) + \frac{\partial}{\partial t}\left(\frac{1}{2}\mu \|\boldsymbol{H}\|^2\right) + \frac{\partial}{\partial t}\left(\frac{1}{2}\varepsilon \|\boldsymbol{E}\|^2\right) + \sigma \|\boldsymbol{E}\|^2 = 0 \quad (21)$$

By integrating Equation 21 with respect to volume, and applying the divergence theorem to the first term, Poynting's Theorem is obtained.

$$\oiint_S (\boldsymbol{E} \times \boldsymbol{H}) \cdot d\boldsymbol{S} + \frac{\partial}{\partial t}\iiint_V \left(\frac{1}{2}\mu \|\boldsymbol{H}\|^2 + \frac{1}{2}\varepsilon \|\boldsymbol{E}\|^2\right) dV + \cdots \quad (22)$$

$$\cdots + \iiint_V \sigma \|\boldsymbol{E}\|^2 \, dV = 0$$

Equation 22 is an expression of conservation of energy for power flow within a volume. The first term represents the power leaving the volume through surface $\boldsymbol{S}$, the second term represents the rate of storage of electric and magnetic energy within the volume, and the final term represents the power lost due to absorptivity.

The expression inside the integrand of the final term of Equation 22 is known as the volume loss density, which is calculated directly from the HFSS simulations using the field calculator tool provided in the software. The volume loss density has units of W/m^3. Integration with respect to the volume of interest gives units of W, representing the power absorbed in the simulated geometry.

$$P_{abs.} = \iiint_V \ \sigma \|\boldsymbol{E}\|^2 \, dV \qquad (23)$$

To determine the proportion of power absorbed by the structure, one must know the incident power, which is determined by knowledge of the incident electric field strength E_0 (the default value is 1 V/m), the cross-sectional area a, and the angle of incidence, θ_i.

$$P_0 = \frac{c\epsilon_0}{2} |E_0|^2 a \cos\theta_i \qquad (24)$$

Here, c is the speed of light and ε_0 is the vacuum permittivity. The absorptivity is defined as the proportion of the incident power that is absorbed by the structure.

$$A \stackrel{\text{def}}{=} \frac{P_{abs.}}{P_0} \qquad (25)$$

It is noted that the method put forth for obtaining absorptivity for the finite arrays was verified by performing the same calculation in a Floquet port setup and comparing the absorptivity with unity minus the reflectivity for a structure containing an opaque ground plane.

For the simulation of finite arrays, perfectly matched layers are used on the boundaries of the computational domain. The only exception is underneath the ground plane, where a PEC is automatically implemented. Perfectly matched layers are artificial materials generated in HFSS, which nearly completely absorb incident electromagnetic fields at most angles. In the many of the simulations using perfectly matched layers discussed in this dissertation, plane wave excitation is set to 60 degrees off-normal angle of incidence, corresponding to the measurements in the near-field and far-field. In an example given in an HFSS tutorial regarding radiation absorbing boundaries, the reflection of incident radiation at 60 degrees was reduced -42 dB by implementation of a perfectly matched layer [52].

2.2 Fabrication

The fabrication of infrared FSS structures normally requires sub-micron resolution; this was initially made possible only by lithographic patterning processes previously advanced by the microelectronics community for integrated circuits. Infrared FSS structures are typically patterned by electron-beam lithography, although additional lithographic processes may be applied. In this work, patterning is carried out in an additive technique by lithographic exposure of positive resists followed by metallization and liftoff. (Alternatively, patterning can be accomplished by a subtractive process using lithography followed by etching). The additive process for the case of electron-beam lithography is shown briefly in Figure 3. As can be seen in the figure, the process starts with a substrate coated with resist. Exposure by an electron-beam patterns the resist by altering its properties; the beam is scanned using a prescribed geometry. The sample is then developed in a chemical solution, leaving the intended pattern as open areas in the positive-toned resist. Next, a thin film is deposited over the entire structure. Finally, the

sample is placed in a chemical solution that removes the resist and only the intended pattern of the material of interest is left on the substrate.

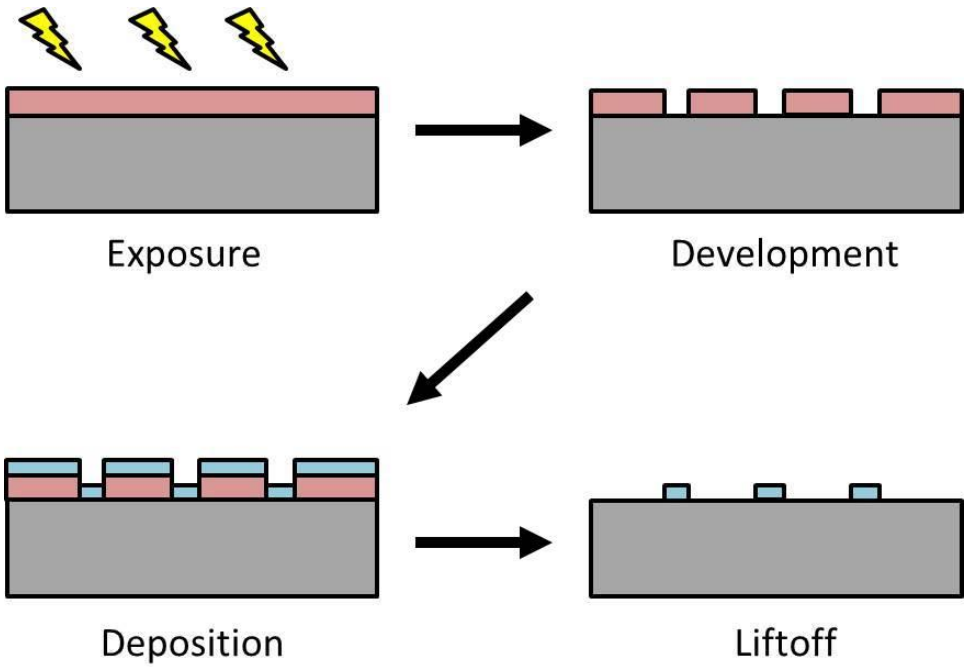

Figure 3. Diagram showing the general procedure for patterning by lithography, metallization, and liftoff.

2.2.1 Lithographic Processes

Lithography, in various forms, is the basis for patterning all structures defined in this work. The lithographic processes considered here are electron-beam lithography and optical-projection lithography. In lithography, a pattern is formed on the sample by developing a layer that has been exposed to energy with spatial variation in irradiance (much like film-based photography). All conventional lithography techniques involve the exposure of resists: these materials are sensitive to energetic particles such as photons, electrons, or ions. Resists are typically polymeric materials that are deposited onto the substrate via spin coating. Once the resists are properly exposed, the intended pattern is created by a development process (normally

a wet chemistry step). In the work described here, an additive lithographic process creates a temporary layer of patterned resist that will be used to make permanent structures through later metallization and liftoff.

Originally, optical lithography took place via contact printing [53]. In this process, a patterned mask is placed in contact with a resist-coated substrate. Ultraviolet light is shone through the mask to expose the resist. Later on, proximity lithography was introduced, where a small air gap is placed between the mask and the substrate [53]. This is done to decrease the physical defects created by placing the mask in direct contact with the sample, but the change makes resolution slightly poorer due to optical interference effects. Later on, projection lithography was introduced, a technique which places a patterned mask (called a reticle) in the object plane of a well-corrected imaging system, while the resist coated substrate is placed in the image plane where a 5:1 or 10:1 magnification reduction of the reticle is imaged. The optical-projection method allows the reticle itself to be fabricated much more cheaply than a photo mask, due to the 5× or 10× increase in geometric dimensions. The advantages of optical lithography are that it is low cost and fast, although the resolution is still an order of magnitude worse than that attainable by electron-beam lithography. The form of optical lithography discussed in this dissertation is optical-projection lithography, as detailed in the discussion of square-patch infrared FSS fabrication in Chapter Seven. The tool used in this case is a GCA 6300C DSW stepper, which uses 5× reduction reticles and g-line (λ=436 nm) exposure.

In electron-beam lithography, the resist is exposed by an electron beam, which is highly focused and scanned across the sample according the exposure pattern that is input to the tool. The foremost advantage of electron-beam lithography is the spatial resolution. Dedicated electron-beam lithography systems are capable of achieving line widths of approximately 10 nm

[54]. Unsurprisingly, the serial nature of this process corresponds to lengthy exposure times. Electron-beam lithography is highly expensive considering the exposure times, initial cost of the tool, and routine maintenance. The electron-beam lithography fabrication detailed in this report was accomplished using two different systems. The first tool used was a Leica EBPG5000+ system (Chapters Three, Four, and Seven), while the second tool used was a JEOL JBX-9300FS system (Chapters Five and Six). In the experiments discussed here, no notable difference in quality was observed between the two tools; however, it is noted that varying the dosing current is much less complicated on the Leica system, allowing some exposures to complete much faster.

A few different resists have been utilized during the research contributing to this dissertation. All of the resists used here have been of the positive-tone variety, which means that the areas exposed to energy are dissolved in the development process, leaving open spaces in the resist layer. ZEP 520A-7 (Zeon Corporation) was the electron-beam resist used in Chapters Three, Four, and Seven, while poly(methyl methacrylate) (PMMA)-A7 (Microchem) was the electron-beam resist used in Chapters Five and Six. ZEP 520A-7 was developed in ZEP-RD (Xylene-based solvent, Zeon Corporation) and lifted off by N, N-dimethylacetimide, while PMMA-A7 is developed in equal parts isopropyl alcohol (IPA) and methyl isobutyl ketone (MIBK), and lifted off by N-methyl pyrrolidinone (NMP) or Remover-PG (NMP with added surfactants, Microchem). Qualitatively, both electron-beam resists have the same resultant resolution, although it is noted that ZEP 520A-7 requires about half the electron-beam dose of PMMA-A7, but is also an order of magnitude more expensive. For the work discussed in Chapter Seven, S1805 was used as a photoresist (Microchem). S1805 is developed in MF-319 (Microchem) and lifted off using the same chemistry as PMMA-A7.

Over the past decade, several novel parallel lithography techniques have been demonstrated at the laboratory and industrial scale that could someday overtake electron-beam lithography as the preferred high-resolution technique for infrared FSS structures. One very promising example is nano-imprint lithography, which takes a master replica and stamps it onto the sample by various methods to create the lithographic process [55]. As this dissertation is centered on large area fabrication, the prospect of fabrication by nano-imprint lithography (or other emerging parallel processes) was certainly attractive; however, workable solutions using this technique via in-house or collaborative efforts were lacking. Fabrication of infrared FSS using an Imprio 100 (Nano Imprints) nano-imprint tool housed in the clean room at UNC Charlotte was briefly considered, but the amount of process engineering which was apparent moving forward was overwhelming compared to the value this work would add to the dissertation.

2.2.2 Thin Film Deposition

Thin films can be deposited a multitude of ways, which are nominally separated into the categories of chemical and physical processes. In chemical thin film deposition processes, a liquid or gaseous precursor is employed and by various methods, a chemical change creates a solid film on the sample. Methods of chemical thin film deposition include electroplating, spin coating, chemical bath deposition, chemical vapor deposition, and atomic layer deposition. Physical thin film deposition techniques employ physical methods such to create thin solid films. Normally, a very pure material source is placed in an energetic environment under vacuum to drive particles from the source to the sample. Methods of physical thin film deposition include

thermal (resistive) evaporation, electron-beam evaporation, molecular beam epitaxy, and sputtering.

The chemical thin film deposition technique used in this work is spin coating. (While the act of spinning a liquid on a substrate is clearly physical, here, spin coating is deemed a chemical deposition technique due to the processing that comes after the material is spun on the substrate.) In spin coating, a fluid is placed at the center of the sample, which is then rotated at high speeds to form a thin film coating. Spin coating apparatus allow the input of spin routines; typically, this consists of an initial spreading step at about 500 revolutions per minute (RPM) for a few seconds, followed by a high-speed (1000 – 5000 RPM) step which brings the film to the desired thickness. In most cases, the sample is then heated in some manner to evaporate the residual solvents. In the case of polymers, a subsequent heating step is required to cure the polymeric thin film coating. The thickness and quality of the spin-coated film depends on the spin speed recipe, the substrate, the thermal processing, and the chemical makeup of the liquid to be spun. The majority of resists and many other materials (such as polymeric dielectrics) are deposited by this method. The main advantage of spin coating over other thin film deposition methods is that it is relatively inexpensive, because it does not require vacuum or energetic environments to create the film. Additionally, thin films deposited by spin coating allow a high degree of planarization over patterned structures; this is not possible with the other deposition methods discussed in this dissertation. The disadvantage of spin coating is that most materials of interest simply cannot be deposited by this method. In the work discussed here, spin coating will be used to deposit lithographic resists as well as Benzocyclobutene (BCB), which is commonly used as a dielectric material in the infrared.

As BCB is referenced quite often in the following chapters, its deposition method is described in detail here. BCB is spin coated using processes not unlike that of any other spin-coated material. As a highly utilized dielectric for implementation in infrared FSS designs, the thickness of BCB must be accurately controlled; thickness variation is achieved to a greater extent by mixing with the solvent mesitylene and to a lesser extent by changing the spin routine. After the spinning process, residual solvents are driven out of BCB by a 3 minute hot plate bake at 115 degrees C, while polymerization takes place at 250 degrees C in an inert environment. The process for BCB has evolved during the course of this dissertation. During the early stages of this dissertation, curing took place by placing a metal container over the hotplate and flowing N_2 into the sample area. Here, the temperature was ramped up to 250 degrees C, held for 5 minutes, and ramped down. The curing process has been improved significantly through the use of a rapid thermal annealer (RTA), which has a control loop to heat more precisely than a hotplate and offers added control over the gaseous sample environment via mass flow controllers. For BCB, a recipe has been implemented in the RTA to heat the sample slowly to the curing point and hold this temperature accurately for 5 minutes, in a controlled environment of N_2.

Electron-beam evaporation is used in this work for the deposition of many metal and dielectric materials, such as Au, Cr, SiO_2, and Ti. (Ti is utilized as an adhesion layer for Au). In this technique, an electron beam is generated, steered, and focused onto the source material to be deposited. The kinetic energy imparted by the beam causes the source material to evaporate or sublime, while the sample placed in the chamber collects a portion of the evaporant in the form of a thin film. This process can only occur under vacuum, requiring somewhat sophisticated vacuum and process control apparatus. An advantage of electron-beam evaporation over some of the other physical deposition methods (such as magnetron sputtering) is that the evaporant flux is

quite directional, allowing for the process of liftoff to occur more easily than in the case of a less directional flux. The directional flux leads to a thickness gradient when coating large samples. If needed, the thickness gradient can be mediated by rotating the sample during the deposition; however, rotation is not an option when the end goal is liftoff of the deposited films.

Thermal or resistive evaporation uses apparatus quite similar to that of electron-beam evaporation. In fact, the vacuum deposition chamber used in much of this work contains the apparatus for both electron-beam and thermal evaporation. For thermal evaporation, electric current is passed through a resistive circuit that houses the substance to be deposited. Consequently, the resistive material heats up, eventually heating the source material to the point of evaporation or sublimation. While the directionality of the flux in this method is highly dependent upon the geometry of the source material and the device that holds it, in most cases the directionality is similar to that of electron-beam evaporation. Thus, thermal evaporation can be used for liftoff processing.

In the work discussed in this dissertation, thermal evaporation is used to deposit Al and ZnS. Aluminum, used as a conductive material for FSS elements and ground planes, is deposited in an alumina-lined basket of wound Ni-Cr alloy wire. ZnS is a dielectric material that is quite valuable in the infrared due to high transparency over a very large bandwidth. In line-of-sight evaporation of ZnS, spitting or streaming of the source material is known to cause defects in the deposited films. To avoid such defects, a baffled box was used in the fabrication runs described in this dissertation. The baffled boxes (R. D. Mathis Company) are made of molybdenum, and contain three compartments. Two side compartments hold the ZnS pellets, while a center compartment remains empty. As the ZnS sublimes, the flux moves from the side compartments

toward the center, and is ejected out of a circular aperture above the center compartment, leading to a uniform, defect-free film since this process eliminates the possibility of spitting.

2.2.3 Etching

The creation of a flake-based FSS coating described within this dissertation requires etching both to define the shape of the flakes as well as to release them from the substrate. Etch processes for thin film fabrication are commonly categorized as wet or dry processes. As the name implies, wet etching is accomplished by placing the sample in the appropriate liquid chemical environment. Dry etching is accomplished by energetic particle bombardment in a vacuum chamber. Etch processes are characterized in terms of selectivity as well as anisotropy. Selectivity refers to the ability to etch certain materials while leaving other materials (on the same sample) relatively unaltered. Anisotropy refers to the ability to etch directionally into the sample or substrate, either due to directional particle bombardment in dry etching or along crystal planes in wet etching.

Wet etching is generally more selective than plasma etching; as a result, each material to be etched has a particular set of corresponding chemicals that allow for selective removal. Additionally, wet etching has the ability to achieve near perfect anisotropy in crystalline materials. In the work detailed here, wet etching is utilized only for the etching of SiO_2 and Cr. SiO_2 is etched by buffered oxide etch (BOE). In the formation of FSS flakes, which will be detailed later, the sacrificial layers of SiO_2 must be removed to release the flakes from the substrate. Additionally, Cr is etched by wet processes to aid in the formation of FSS flakes by etching the ground plane in between adjacent flakes.

In plasma (dry) etching, a plasma is created in the presence of a pure gaseous mixture that bombards the sample. Depending on the degree of directionality of the process, thin film structures may be patterned using plasma etching. Patterning is accomplished by placing a mask layer on top of the sample. The mask layer is defined lithographically and has features that are approximately the size and shape of the intended geometry underneath. Ideally, the mask layer is fabricated from a material that is not etched by the plasma process. Since plasma processes are highly energetic, in most cases this is not possible, so typically a mask material is used that has an etch rate less than the material to be etched. A main advantage of plasma etching over wet etching is increased process repeatability. Additionally, plasma etching may be and stopped or started immediately, which is not generally possible in wet etching. Also, in certain situations a high degree of anisotropy can be achieved on non-crystalline samples.

In this work, plasma etching of BCB is used to define the size and shape of the FSS flakes. Here, plasma etching of BCB has been carried out utilizing SiO_2 as the etch mask material. When etching BCB, a partial pressure of CF_4 or SF_6 must be introduced into the O_2, otherwise, the process will become self-passivating and eventually stop [56]. In this work, BCB has been etched using a combination of CF_4 and O_2 in a Branson P2000 barrel etcher and using a combination of SF_6 and O_2 in a Surface Technology Systems Advanced Oxide Etcher. More specific procedural details will be included in Chapter Three (where CF_4 is used) and Chapter Seven (where SF_6 is used).

2.3 Characterization

For FSS structures, characterization is arguably the most important step in the design – fabricate – test paradigm. FTIR characterization of fabricated samples typically confirms

whether they yield the intended spectral response, while ellipsometric characterization of witness samples yields the optical constants of the fabricated thin film materials, which are utilized in the electromagnetic simulations. The experiments presented in this dissertation use both far-field and near-field characterization techniques to yield insight into the physical phenomena of interest. In the far-field, standard FTIR spectrometry is used to confirm the intended optical response and ellipsometry is used to determine the optical constants and thickness of the materials of interest. In the near-field, s-SNOM is used to map the local electric fields in the vicinity of resonant infrared FSS structures.

2.3.1 Material Characterization by Ellipsometry

Ellipsometry is a characterization technique that utilizes the change in the polarization of light upon interaction with a surface to determine information about the optical properties of the sample under test. The information which can be inferred from ellipsometry is the complex refractive index (n and k) and related quantities as well as the thickness of thin film layers. Ellipsometry is extremely useful in this dissertation, since the measured optical constants are input into the frequency dependent electromagnetic simulations and these constants along with the thickness are used to determine the quality and accuracy of the thin-film deposition.

Ellipsometry exploits the polarization nature of light at planar interfaces to achieve these important results. The polarization of the incident light can be split into two orthogonal orientations, s-polarization and p-polarization. To understand this convention, consider a propagating beam at a single interface. An imaginary plane, which is normal to the interface and contains the propagation vector of the incident light, is known as the plane of incidence. The orientation of s-polarized light (also known as TE polarization) is such that the electric field is

polarized normal to the plane of incidence and parallel to the interface. The orientation of p-polarized light (also known as TM polarization) is such that the electric field is polarized within the plane of incidence.

At an interface between two media, light can be either transmitted or reflected. In terms of s-polarized and p-polarized light, the transmission and reflection at a single interface are computed by the Fresnel coefficients. Since the ellipsometers used in this dissertation work in reflection mode, only the reflection coefficients are discussed here. The Fresnel reflection coefficients at a single interface are given as follows [57].

$$r_{12}^{p} = \frac{\tilde{N}_2 \cos\phi_1 - \tilde{N}_1 \cos\phi_2}{\tilde{N}_2 \cos\phi_1 + \tilde{N}_1 \cos\phi_2} \quad (26)$$

$$r_{12}^{s} = \frac{\tilde{N}_1 \cos\phi_1 - \tilde{N}_2 \cos\phi_2}{\tilde{N}_1 \cos\phi_1 + \tilde{N}_2 \cos\phi_2} \quad (27)$$

Here, *s* and *p* denote the orthogonal polarization states, $\tilde{N}_1$ and $\tilde{N}_2$ correspond to the complex refractive indices in medium 1 and 2, ϕ_1 corresponds to the angle of incidence (from normal) in medium 1, and ϕ_2 corresponds to the refracted transmitted angle (measured from normal) in medium 2. Equations 26 and 27 refer to field quantities. The quantities measured directly by ellipsometry are the reflected intensity values, which are the squared modulus of the field quantities, given as follows [57].

$$R_{12}^{p} = \left|r_{12}^{p}\right|^2 \quad (28)$$

$$R_{12}^{s} = \left|r_{12}^{s}\right|^2 \quad (29)$$

The quantities in Equations 26 through 29 are based on a single interface between two bulk materials, which is not typically the case in ellipsometry. Instead, stratified thin film structures are analyzed using cascading matrix methods employed in the modeling software corresponding to the ellipsometry apparatus. The instrument manipulates polarization optics both at the source and the detector to report the data in terms of the ellipsometric constants, ψ and Δ. They are defined as follows [57].

$$\tan\psi = \frac{|r^p|}{|r^s|} \quad (30)$$

$$\Delta = \delta_1 - \delta_2 \quad (31)$$

Here, r^p and r^s are the generalized (extended to any number of thin-film layers) reflection coefficients, δ_1 represents the phase difference between the incident p-polarized and s-polarized light and δ_2 represents the phase difference between the reflected p-polarized and s-polarized light. Equations 30 and 31 are commonly combined as follows [57].

$$\tan\psi\, e^{j\Delta} = \frac{r^p}{r^s} \quad (32)$$

The ellipsometric measurement systems utilized in this dissertation are a pair of variable angle spectroscopic ellipsometers (VASE) from J. A. Woollam. The VASE tool measures the range 0.3 μm to 2 μm, while the infrared-VASE (IR-VASE) measures the range 1.7 μm to 30 μm. The VASE has an interrogation beam approximately 2 mm in diameter in the vertical direction while the IR-VASE has a 1 cm diameter interrogation beam in the vertical direction. Considering that the sample is rotated on a horizontal goniometer to set the angle of incident

irradiance, the horizontal diameter of the interrogation beam scales inversely by the cosine of the angle of incidence. These instruments typically determine the ellipsometric constants at three separate angles of incidence to increase confidence in the oscillator-based modeling. The angles of measurement are best chosen near the Brewster angle where p-polarized light exhibits no reflection, since near this angle there is the greatest sensitivity between the two reflected polarization states.

The thin film stack is modeled in J. A. Woollam VASE software and the optical constants of the films are derived in the software using dispersion relations for transparent materials and oscillator models such as Gaussian, Drude, or Tauc-Lorentz for lossy or metallic materials. It is important to note that causality is enforced during this process, yielding optical constants that are Kramers-Kronig consistent. The goal of ellipsometry for this work is to obtain the frequency dependent optical constants of the constituent materials in the infrared FSS designs. The measurement of optical constants is of the utmost importance due to the fact that materials are very dispersive in the infrared, with properties that can change due to the thin film processing conditions. Additionally, it is noted that ellipsometry offers a non-destructive method to obtain the thickness of deposited thin films, which is highly accurate for dielectric materials. Ellipsometry may be employed on the sample after each deposition in the fabrication process. Alternatively, witness samples can be collected during the sample deposition, such that the precise optical constants can be incorporated into the simulations while the actual sample remains in a clean room environment.

While the electromagnetic simulation software requires the optical properties to be input in terms of conductivity or loss tangent, the J. A. Woollam software outputs the optical constants in terms of the complex refractive index or relative permittivity, given as follows.

$$\tilde{N} = n + jk \quad (33)$$

$$\tilde{\varepsilon}_r = \varepsilon_r' + j\varepsilon_r'' \quad (34)$$

Here, n is the real part of the complex refractive index while k is the imaginary part. Likewise, ε_r' is the real part of the relative permittivity and ε_r' is the imaginary part. The relation between refractive index and relative permittivity is as follows.

$$\tilde{\varepsilon}_r = \tilde{N}^2 = n^2 - k^2 + j2nk \quad (35)$$

Depending on the boundary conditions used in HFSS, the material properties are input in terms of the real part of the permittivity and either the loss tangent or the conductivity, defined as follows, in terms relating to Equation 34.

$$\tan\delta = \frac{\varepsilon_r''}{\varepsilon_r'} \quad (36)$$

$$\sigma = 2\pi f \varepsilon_r'' \quad (37)$$

Here, $\tan\delta$ refers to the loss tangent and f refers to the frequency of interest, related to the wavelength of interest by $c = f / \lambda$.

2.3.2 Far-Field Sample Characterization

Most of the applications one could imagine for a large area, conformal infrared FSS coating as described in this dissertation relate to properties of the treated surface in the far-field.

Surface appearance in the infrared is often measured in the far-field by FTIR or laser-based systems; this dissertation utilizes FTIR systems extensively for far-field characterization. FTIR is a spectroscopy technique based on post-processing of broadband interferograms. Originally developed for absorptance measurements, the FTIR obtains spectral information such as the power reflected by and transmitted through the sample; these are commonly termed reflectivity and transmissivity. Conservation of energy dictates that these quantities, along with absorptivity (the proportion of incident power absorbed by the sample), are equal to unity for a given wavelength and angle of illumination.

$$R(\lambda) + T(\lambda) + A(\lambda) = 1 \quad (38)$$

Here, *R(λ)*, *T(λ)*, and *A(λ)* correspond to the spectral reflectivity, transmissivity, and absorptivity, respectfully. A common figure of merit in this work will be the spectral absorptivity, since the resonant modes observed in the near-field in infrared FSS tend to lead to absorptive behavior in the far-field. The majority of designs discussed here will involve a ground plane, which is an optically thick, reflective substrate layer, driving the transmissivity term to zero. Hence, the spectral absorptivity can be calculated simply from the spectral reflectivity.

$$A(\lambda) = 1 - R(\lambda) \quad (39)$$

An additional figure of merit, which is frequently considered in the infrared regime, is emissivity. Emissivity is the ratio of an object's ability to emit radiation compared to that of an ideal blackbody. Kirchhoff's law of thermal radiation dictates an object in equilibrium has emissivity equal to its absorptivity. Thus, the spectral emissivity is equivalent to absorptivity for

an object in thermal equilibrium, and can be calculated from the spectral reflectivity measured by FTIR in the same manner.

$$\varepsilon(\lambda) = 1 - R(\lambda) \quad (40)$$

The FTIR used in Chapters Three and Seven of this work is a Perkin-Elmer micro-FTIR spectrometer with microscope attachment, yielding a biconical reflectance geometry. The microscope attachment has a 600 μm diameter circular aperture in the optical train, which corresponds to approximately 100 μm diameter at the sample surface. Due to the reflective focusing optics of the microscope, the angles measured by the tool in reflectivity mode are between 10 degrees and 25 degrees from normal. The tool is equipped with an in-line video camera, which has been especially helpful in this dissertation since it allows for visual confirmation of small interrogation areas.

Two additional FTIR based systems have been utilized for sample characterization in this dissertation. First, the previously mentioned IR-VASE apparatus was used in Chapter Five to determine the s-polarized specular reflectivity at 60 degrees off normal for the quasi-infinite and truncated array samples. Additionally, a hemispherical directional reflectance (HDR) tool was used in Chapter Seven to characterize the samples designed to tune the effects of array truncation (SOC-100, Surface Optics Corporation). Here, a 2π hemispherical ellipsoid is used to uniformly illuminate the sample with a blackbody source. A moveable focusing mirror and beam blocker are used to measure the specular (SDR) and diffuse (DDR) components which sum both in reflectance and solid angle to yield the HDR.

2.3.3 Near-Field Sample Characterization

While most applications rely on the far-field spectral response of infrared FSS structures, there is merit in measurement of the near-field quantities as well. The most straightforward application of near-field measurements is the corroboration of simulations. HFSS is a full-wave electromagnetic solver using FEM, which by definition obtains to the far-field results by computation of quantities in the near-field mesh. Thus, it is useful to measure the local electric field and compare with that computed in the simulations. Taking the argument a step further, for designs that are difficult or computationally expensive to simulate, near-field mapping techniques offer valuable insight that cannot be conveniently obtained by other means. It is additionally noted that while s-SNOM has been used here primarily as an engineering tool, the 10s of nm spatial resolution is much smaller than the diffraction limited resolution of standard optical systems. For this reason, near-field scanning instruments are useful for a multitude of interesting technical studies that will not be discussed in this dissertation.

Over several years, an s-SNOM has been constructed in-house, based on an apparatus used in previous collaborations where optical antennas were investigated [58, 59, 60]. The apparatus is capable of interpreting the electromagnetic fields near structures by analyzing the scatter from an atomic force microscope (AFM) cantilever hovering very close to it in tapping mode. The AFM system used in this apparatus is an Innova system from Bruker Corporation. We have found that reliable data sets are obtained using Arrow-NCPt AFM tips (NanoWorld). These are coated with a platinum-iridium for high reflectivity, and have a resonance frequency near 285 kHz.

Figure 4 shows the current configuration of the s-SNOM apparatus, as it illuminates a square-loop type FSS. The s-polarized incident beam is that of a CO_2 laser normally operating at

10.6 μm (L4S, Access Laser Company). The beam impinges upon a ZnSe beam splitter and a portion of it is directed toward the sample area, where it is focused onto the sample using an off-axis parabolic (OAP) reflector. A beam waist of approximately 50 μm is present in the plane of the sample. The incident beam is restricted to 60 degrees from normal incidence due to the presence of the AFM cantilever.

The interaction of light with sub-wavelength inhomogeneities leads to the occurrence of evanescent fields [61]; such is the case for infrared FSS structures which resonate at or near the frequency of the excitation laser. These evanescent resonant fields are typically confined close to the FSS; however, the presence of the AFM cantilever well within the exponential decay length allows a portion of the evanescent fields to be coupled into free space, back into the s-SNOM system. It is noted that the AFM cantilever preferentially scatters those evanescent fields which are polarized in the direction normal to the surface of the sample [25, 58, 59, 62]. In this manner, the Pt-coated cantilever acts as an antenna, preferentially scattering fields along the axis of its shaft [63].

The scattered sample beam impinges upon the beam splitter and is passed through a wire grid polarizer before being focused on a liquid N_2 cooled mercury cadmium telluride (MCT) detector. In its usual configuration, the wire grid polarizer passes only the polarization state corresponding to the field normal to the sample. The orthogonally polarized excitation and detection scheme is believed to reduce noise by eliminating reflected or scattered radiation that is polarized the same as the incident beam. To measure both amplitude and phase of the field, the sample beam is combined with a reference beam in a Michelson (homodyne) configuration. The reference leg of the interferometer contains a quarter wave plate for attenuation and the reference

mirror is placed on a piezo actuator (P-841, Physik Instrumente) for fine control of the reference phase.

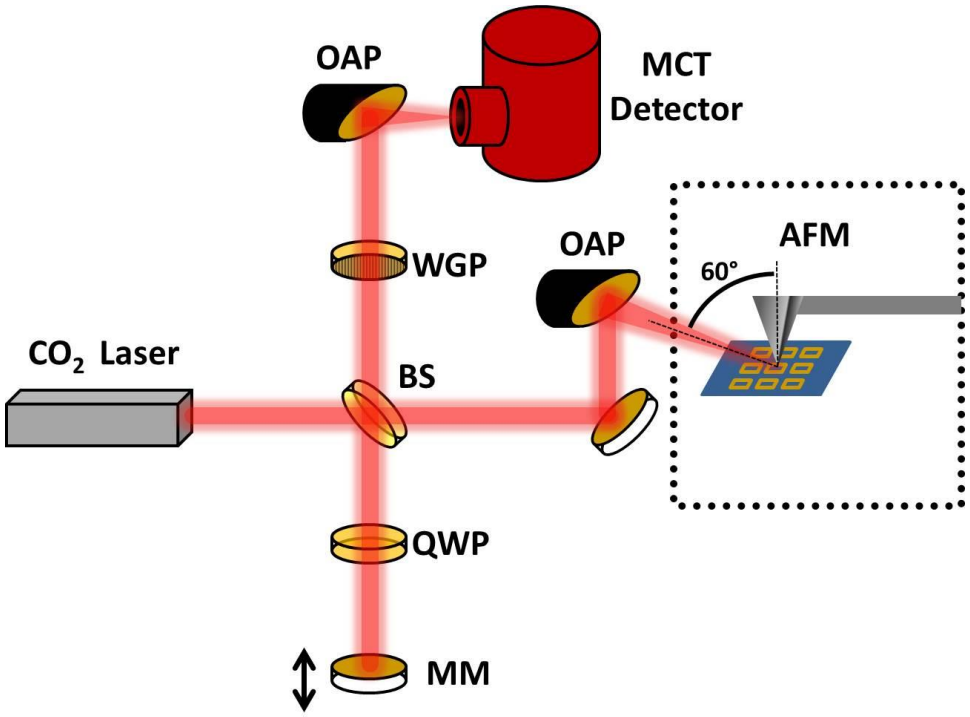

Figure 4. Schematic of the s-SNOM apparatus.

The sample sits on a moveable stage controlled by the AFM hardware and the optical signal is recorded as the sample scans in the x and y direction. The detected optical signal at each x and y coordinate on the sample is proportional to the interferometric intensity received at the detector [25].

$$S_d \propto \left|E_{scat} + E_{ref}\right|^2 = |E_{scat}|^2 + \left|E_{ref}\right|^2 + 2\left|E_{scat}E_{ref}\right| \cos\phi + I_b \qquad (41)$$

Here, E_{scat} is the scattered electric field, E_{ref} is the electric field of the reference beam, ϕ is the phase of the scattered field relative to the reference field, and I_b is a background intensity from reflections or scattering which is unrelated to the local electric field of interest. The signal output from the MCT detector is demodulated by a lock-in amplifier (Signal Recovery). The lock-in amplifier analyzes the signal at a harmonic of the AFM cantilever dither frequency (typically the second harmonic) which removes the constant reference beam intensity term and greatly reduces the background noise existing at lower frequencies in the signal spectrum. In the experiment, the reference phase is adjusted by fine movement of the reference mirror. By taking consecutive scans over the same sample area at different reference mirror positions, several data sets of the following form (at each point in x and y on the sample) are obtained [62].

$$S_d = A + B\cos(\phi + \delta) \quad (42)$$

Here, δ is the additional phase increase or decrease by tuning of the reference leg, adjusted for each measurement [62]. At this point, only S_d and δ are known at each x and y position on the sample.

The data sets are fitted to a sinusoid using a least squares fit which is processed in Matlab. The raw data can be expressed as a column matrix as follows, with respect to the reference phase, at each x and y position on the sample.

$$\overleftrightarrow{S_d} = \begin{bmatrix} S_d(\delta_1) \\ S_d(\delta_2) \\ \vdots \\ S_d(\delta_N) \end{bmatrix} \quad (43)$$

Here, it is noted that the range of δ_1 to δ_N typically covers at least one full cycle in phase, and doesn't include any large gaps in the progression of phase. Both of these conditions generally reduce potential errors in the fitting. A linear combination of basis functions expressing a sinusoidal cycle can be depicted in matrix form as follows.

$$\overleftrightarrow{A} = \begin{bmatrix} 1 & \cos(k_0\delta_1) & \sin(k_0\delta_1) \\ 1 & \cos(k_0\delta_2) & \sin(k_0\delta_2) \\ \vdots & \vdots & \vdots \\ 1 & \cos(k_0\delta_N) & \sin(k_0\delta_N) \end{bmatrix} \quad (44)$$

Here, $k_0 = 2\pi / \lambda_0$, the free-space wave-vector. It is noted that both sine and cosine terms are implemented because the maximum amplitude with respect to the reference phase is not necessarily known *a priori*. To find the best fit coefficients of the basis functions, which will lead to the description of the amplitude and relative phase we seek, the following overdetermined matrix equation must be solved.

$$\overleftrightarrow{A}\overleftrightarrow{x} = \overleftrightarrow{S_d} \quad (45)$$

The least-squares fit in matrix form is expressed as follows.

$$\overleftrightarrow{x} = \left(\overleftrightarrow{A}^{\dagger}\overleftrightarrow{A}\right)^{-1}\overleftrightarrow{A}^{\dagger}\overleftrightarrow{S_d} \quad (46)$$

Here, † denotes transposition.

The fit yields a function of the following form at each x and y coordinate on the sample

$$S_d = \xi_1 + \xi_2 \cos\delta - \xi_3 \sin\delta \quad (47)$$

Here, ξ_1, ξ_2, and ξ_3 are coefficients from the least squares fit, with ξ_2 and ξ_3 containing information about the amplitude and relative phase of the local electric field. We wish to express the data in terms of amplitude and relative phase of the electric field at each x and y coordinate on the sample, analogous to Equation 42, as follows.

$$S_d = S_0 + S_A \cos(\phi + \delta) \quad (48)$$

Here, S_0 is a constant "DC" offset term and S_A corresponds to the local electric field amplitude. Using trigonometry, Equation 48 is expanded as follows.

$$S_d = S_0 + S_A \cos\phi \cos\delta - S_A \sin\phi \sin\delta \quad (49)$$

Comparing Equations 47 and 49, the functions we seek (the constant term, the amplitude term, and the relative phase term) can be calculated as follows.

$$S_0 = \xi_1 \quad (50)$$

$$S_A = \sqrt{\xi_2^2 + \xi_3^2} \quad (51)$$

$$\phi = \tan^{-1}\left({}^{-\xi_3}/_{\xi_2}\right) \quad (52)$$

Typically, the data are expressed in terms of amplitude and relative phase. Additionally, an animation may be constructed showing the local electric field fluctuation upon the structure with advancing phase.

The experimental description discussed here has assumed that the data sets at each reference phase value have been obtained over the exact same sample area for each scan, but this is not always the case. Often, the sample is observed to translate a few hundred nm or rotate slightly as a full data set is obtained. The effects of sample movement are mitigated using an image registration routine. Here, the first AFM height image is used as a reference, and subsequent height images are registered to it using a publicly available Matlab image registration script [64]. The script generates a spatial transform matrix for each AFM height data set, which is then applied to each corresponding electric field data set, effectively eliminating the sample drift.

The data acquisition and processing described here are related closely to the concept of phase-shifting interferometry, which was introduced for near-field data processing by Deutsch, Hillenbrand, and Novotny [62]. The main difference is that in their work, the reference phase was advanced in equal steps with corresponding field values recorded at each step; amplitude

and phase images were extracted using an algorithm developed for optical surface metrology [65]. It is noted that there exist alternative near-field detection strategies to the homodyne method employed here. Heterodyne methods have been utilized, where the reference beam is frequency-shifted with respect to the sample beam, usually by way of acousto-optic modulation [66]. The pseudo-heterodyne technique has also been implemented for near-field signal recovery, wherein the phase of the reference beam is modulated, providing sidebands in the detected spectrum via frequency mixing [67]. The advantage of both mentioned alternatives to homodyne strategies is a greater reduction of background noise. However, this background scattering is much more pronounced in measurements of weakly resonant and non-resonant structures and much less influential in near-field measurements of strong optical resonances such as those reported in this dissertation.

CHAPTER THREE: PROOF OF CONCEPT FOR FLAKE-BASED INFRARED FREQUENCY SELECTIVE SURFACE COATING

A large area conformal infrared FSS coating has been proposed in this dissertation, which consists of miniature infrared FSS arrays released from a much larger original array. A proof of concept for this idea is presented and discussed within this chapter. The method is based on a selective etching process that includes both wet and dry steps. The spectral reflectivity of the collected miniature FSS arrays is compared to the original full array from which they were formed. It is seen that the spectra of the collected particles have similar features as compared to the full array, with strength of resonance diminished by the non-unity proportion of the particles in the field of view of the measurement instrument [48].

3.1 Fabrication Throughput for Infrared Frequency Selective Surface Flakes

The formation of a flake-based large-area coating is carried out by fabricating a typical FSS array and using selective etching techniques to define the size and shape of flakes as well as to release them from the substrate. The FSS array is created by standard thin-film deposition and electron-beam lithography processes. An etch mask is fabricated on top of the completed structure, allowing the area in between adjacent flakes to be etched while leaving the intended flake area untouched. To release the flakes from the original substrate, a sacrificial layer is used. This layer acts to support the FSS until the point that it is etched away to release the flakes from the substrate. After the FSS particles are released, the solution is drawn through a filtered

syringe. The filter collects the flakes, and this collected material is pressed onto a clean Si wafer for further characterization.

The fabrication process began with a clean substrate. Standard 3" Si wafers were rinsed thoroughly with acetone, methanol, and IPA before plasma cleaning in a Branson P2000 barrel etcher for two minutes in an O_2 plasma. Figure 5 is a schematic showing an example single FSS layer flake before etching. The final formation of flakes requires a sacrificial layer of SiO_2 between the FSS and the Si wafer. In all fabrication runs, this layer was 150 nm and deposited by electron-beam evaporation. The first layer of BCB was applied via spin coating and curing in an inert environment of N_2. The Au elements were formed by direct-write electron-beam lithography, metallization by electron-beam evaporation, and liftoff. It is noted that an adhesion layer of Ti was applied in situ before the Au deposition. Here, ZEP 520A-7 was used as electron-beam resist, the exposed areas were developed using ZEP-RD, and liftoff occurred in N, N-dimethylacetamide. The lithographic exposure took place using the Leica system that was described previously. Liftoff was followed by an additional layer of BCB, again applied by spin coating and curing in an inert environment.

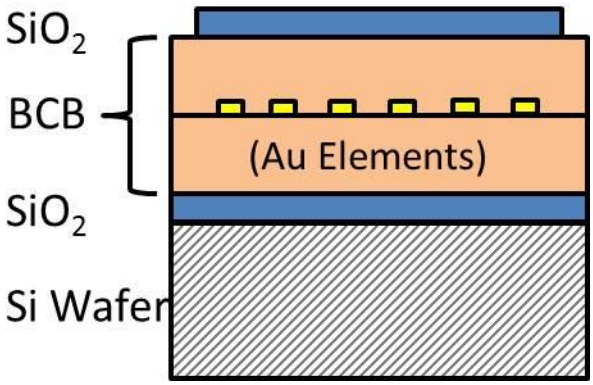

Figure 5. Schematic showing a generic thin film stack of a single FSS flake structure before the etching processes.

The intended flake size and shape was defined by the creation of a 150 nm thick SiO_2 etch mask placed above the entire structure, fabricated again by electron-beam lithography and liftoff. It is noted that in a production environment this step could easily be completed using photolithography. The mask was composed of squares with 20 μm edges, corresponding to roughly a 10×10 array of the FSS elements discussed here. The areas not protected by the etch mask were removed in the barrel etcher by a CF_4:O_2 plasma; this process left areas protected by the etch mask relatively unchanged. For reference, the procedure of etching and subsequent release of the flakes (for the square-loop FSS particles containing two layers of elements symmetric about a ground plane) is shown in Figure 6. The FSS-embedded flakes were defined in size and shape by the plasma etch, which quickly removed the exposed BCB while slowly etching the SiO_2 mask. The goal was to etch in between the flakes down to the sacrificial SiO_2 layer with the etch mask still intact, to protect the sub-arrays for subsequent processing steps.

Plasma etching was carried out in a Branson P2000 barrel etcher, which was mentioned earlier. In this work, it was determined after several experiments that at 200 W, a ratio of CF_4:O_2 of approximately 1:3 lead to an etch rate of roughly 150 nm per minute. It should be mentioned that plasma etching BCB in a barrel-type etcher is not recommended due to poor etch uniformity, lack of directionality, and lack of temperature control [56]. More repeatable results can be obtained with a reactive ion etch (RIE) tool [68]; however, this type of apparatus was not available at the time of these experiments. Owing to the single-layer element design, the plasma etch for the crossed-dipole flakes occurred in one step. The square-loop FSS particles consisted of two element layers separated by a ground plane, requiring additional processing steps as shown in Figure 6. First, the BCB was etched down to the ground plane. Then, the ground plane in areas between the flakes was removed by a wet etch in Chrome Etch (Ashland Specialty

Chemical Company) for 60 seconds. Finally, the BCB sections in between the intended square-loop flakes were etched down to the sacrificial SiO_2 layer.

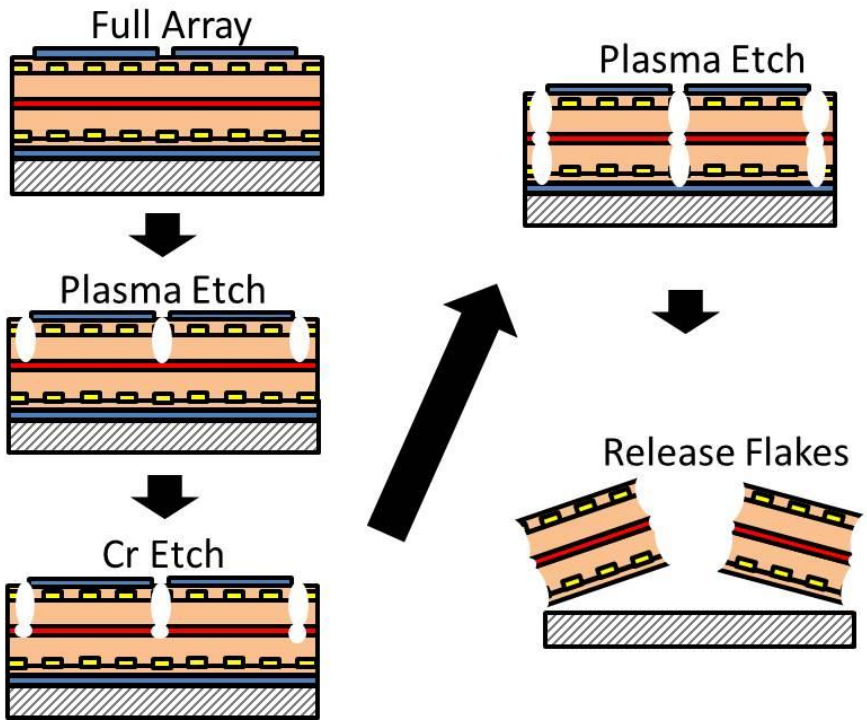

Figure 6. Diagram showing the etching processes used to create the FSS particles. In particular, the process corresponding to the square-loop FSS flakes is shown.

After the flake geometry was defined by the etch mask and the area in between the flakes was etched down to the sacrificial layer, they were released from the substrate by placing the sample in BOE. This process is well known to selectively etch SiO_2 while etching Si at a lower rate [69]. The sample was submerged in BOE under ultrasonic agitation, and the flakes were released from the substrate after about 5 minutes. Progress of this process could be seen as the solution became cloudy due to the proportion of released flakes. As will later be evidenced in scanning electron microscope (SEM) images, the exposure of the Cr ground plane and the BCB layers to the BOE did not have a catastrophic effect, which implies that the BOE etched the SiO_2

much more aggressively than the BCB and Cr. After the FSS particles were released from the substrate, the solution was drawn up through a syringe with a nylon screen filter attached to the nozzle. The chosen screen (Small Parts, Part No. B000FMUL41) had square openings of 11 μm, about half the size of the fabricated flakes. The filtered end of the syringe was pressed against a clean Si wafer, transferring the majority of the FSS flakes in the process. The wafer containing released flakes was placed on a 180° C hot plate for a few seconds to evaporate any remaining liquid BOE. The clean Si wafer was the final destination of the flakes, and all observations and measurements were conducted with the flakes clinging to the wafer.

3.2 Material Considerations

Resonant infrared FSS often consist of a conductive element stood off from a ground plane using a dielectric material, in a design strategy reminiscent of the circuit analog FSS absorber from microwave theory [6]. Due to dispersion of the material properties at optical frequencies, the design materials chosen for fabrication significantly influence the spectral response. For the purposes of FSS flake fabrication, the choice of materials to be used is even more critical since several etching steps take place in the process. The use of ultrasonic agitation for the liftoff of metallized elements as well as the final flake release in BOE further requires that the materials used must have good adhesion properties with respect to each other.

As an example of the importance of material choices in the design influencing the fabrication, the initial FSS flake formation scheme is presented here, which had catastrophic failure during the etch processes. Initially, the FSS design was a single layer crossed-dipole array (with dielectric layers on both sides). The crosses were constructed of Al and the dielectric was Si; both were deposited via electron-beam evaporation. SiO_2 was again used as both a sacrificial

layer underneath the intended flakes and as a protective hard mask above the intended flakes. The flakes were to be defined by placing the sample in a heated bath of potassium hydroxide (KOH) and then released in BOE. (KOH is well known to etch Si at a much greater rate than SiO_2). Several fabrication runs were attempted using this process, and in all cases, only one or two flakes (an infinitesimally small portion of the original sample area) survived the processing conditions. Those flakes that survived were quite strange looking and appeared to suffer partial delamination, with many of the Al elements removed. As an example, a photograph of one of the few surviving flakes from this process is shown in Figure 7. It was eventually determined that the main failure mode during the etch processing was due to the topography which existed throughout the structures. The KOH was able to penetrate the Si underneath the etch mask as well as the Al elements due to topographical variations caused by the thickness of the cross elements. Once the KOH reached the Al elements, rapid failure occurred since the solution etches Al at an even higher rate than Si.

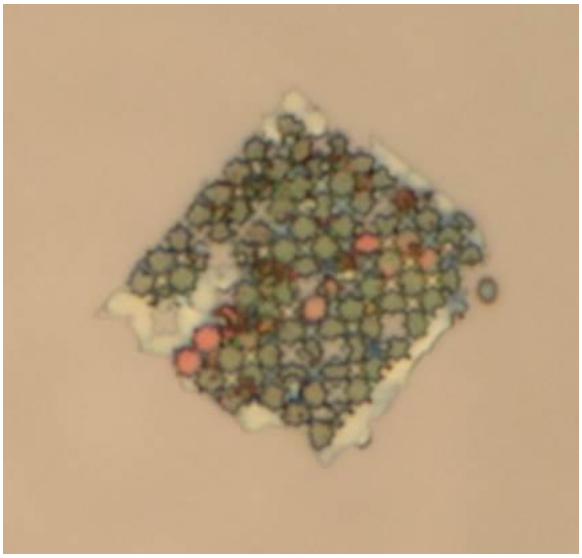

Figure 7. Photograph of one of the few FSS flakes that survived the initially proposed etching process. The dimensions of the flake are approximately 20 μm × 20 μm.

The resolution to the problems arising from topography was realized by utilizing a material that could planarize the top surface of the FSS elements. For various reasons, the BCB polymer CYCLOTENE 3022-35 (from The Dow Chemical Company) was chosen as the dielectric layer. First, it allows planarization over the FSS elements [70]. Also, while it exhibits absorption bands in the 8 μm – 13 μm range, it also permits some wide regions of transparency in the infrared [50]. In addition, our laboratory has already developed successful in-house processing capabilities for BCB, and it had previously been proven to be a useful material in the infrared for FSS [71], antennas [72], and transmission line designs [73].

The BCB curing process requires a N_2-fed enclosure to create an inert environment. For the fabrication of the square-loop flakes, the essential symmetry about the ground plane required various thicknesses of BCB. This was accomplished by adding controlled amounts of mesitylene (Arcos Organics) to the BCB. The mass of each component was measured on a digital scale, and the required thicknesses were realized after a few iterations involving fabrication and thickness determination via ellipsometry. The thickness of BCB was also altered by changing the RPM during the spin coating deposition; however, this technique at times had a negligible effect due to the already relatively thin dimensions of the desired films.

While the choice of Au for the FSS elements was made purely because of its relatively high conductivity at infrared frequencies, the choice for Cr as the ground plane material was determined by the fabrication requirements. Ideally, the ground plane would be a perfect reflector over the spectral range of interest. Chromium is only slightly less reflective than Au. A recent measurement of an optically thick Cr ground plane yielded 95.3% reflectivity at 10 μm near normal incidence, as referenced to a Au reflectivity standard. The chief advantage of Cr as a

ground plane in this work is that it adheres well to BCB and that BCB adheres well to it. This is important in the work described here because there are several ultrasonic processing steps involved. In previous and subsequent efforts, Au and Al were attempted as ground plane materials, but the fabricated structure fell apart during liftoff in the ultrasonic bath. Additionally, Cr is easily wet etched, making it perhaps the ideal ground plane material for use in the fabrication of dual-layer FSS particles using BCB as the dielectric material.

3.3 Crossed-Dipole Flakes

A crossed-dipole design was demonstrated first because it is a simple structure and generally has not experienced problems with liftoff processes in past work. Additionally, it is a structure with square symmetry, which is important given the random nature of the eventual flake distribution. The crossed-dipole FSS has a fundamental resonance corresponding to the length of the dipole that scales proportional to $\lambda/2$ (effective wavelength in the medium), although this initial work was mostly concerned with developing an acceptable fabrication process. A circuit analog has been derived for the crossed-dipole [26]. The design input to the simulation (and subsequently the intended fabrication) was as follows; see Figure 8 for reference. For the crossed-dipole array, the elements were created from Au, with a dipole length of 1.4 μm and a periodicity of 1.8 μm. The line width was 300 nm and the element thickness was 75 nm. A 2 nm Ti layer was deposited beforehand to promote adhesion between the BCB and Au. The elements sat upon a 250 nm layer of BCB and another 250 nm layer of BCB was deposited above the elements. The crossed-dipole array was simulated upon a Si wafer substrate, which was the environment after collection.

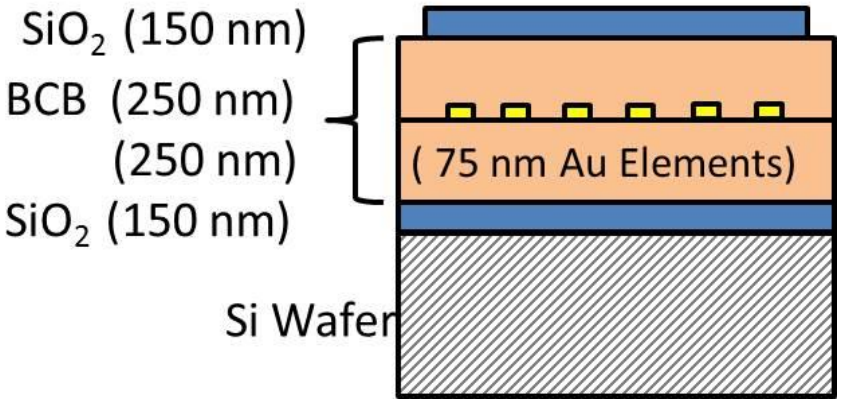

Figure 8. Schematic of a crossed-dipole flake, showing the thickness of each layer.

The fabricated flakes were observed using a Zeiss Ultra-55 SEM. Even though the conductive Au elements were encased in the dielectric BCB, SEM imaging provided an acceptable level of contrast. The dielectric layers were susceptible to charging during SEM imaging; this was mitigated to some extent by changing the accelerating voltage of the electron beam while observing the image in real time. Figure 9 is an SEM micrograph of a single crossed-dipole flake. It can be seen in the figure that the fabricated result is a sufficient example of the intended design. (It is noted that the crossed-dipole design included a ring around the perimeter of each flake that was not populated with Au elements. Lithographically defined alignment marks were included during the crossed-dipole patterning, for later alignment of the etch mask). The figure shows that the inclusion of an unpopulated ring of material around the flake perimeter leads to crisp, well-defined edges. Figure 9 also depicts a slight perimeter line, which indicates an expected undercut due to the isotropic plasma etch caused by the non-ideal barrel etch process.

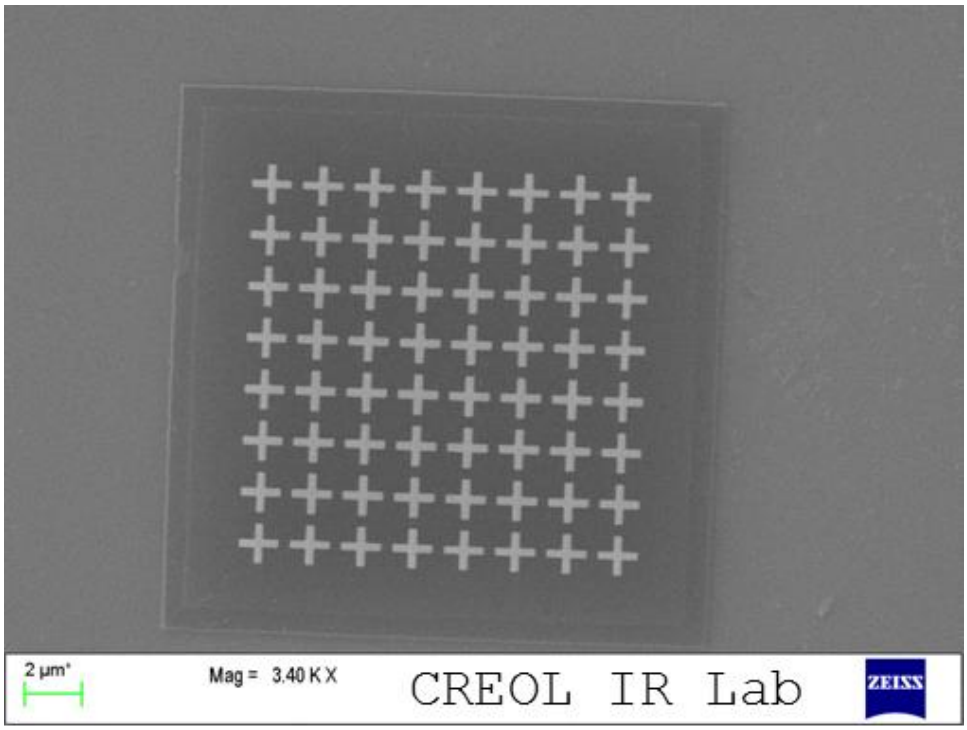

Figure 9. SEM micrograph of a single crossed-dipole flake.

FTIR measurements were taken on areas with the greatest number of the collected flakes, using the instrument with the microscope attachment discussed previously. Figure 10 shows the spectral reflectivity of an area containing crossed-dipole flakes, plotted in blue, on the scaled right axis. The full array of crossed-dipole FSS was measured as well; this is plotted in green on the left axis. In addition, the HFSS simulation (which is of the infinite FSS array) is plotted in red against the left axis. As can be seen in the graph, the spectral reflectivity in all three cases has approximately the same shape, with a peak in the reflectivity near 5 μm and a sharp drop in the reflectivity toward the shorter wavelengths. It is noted that since the distribution of the flakes is random, the amplitude of the features in the reflectivity spectrum varies proportionally depending on the coverage of the measurement area by the flakes.

The spikes in reflectivity seen in Figure 10 near 8 μm and 9.5 μm correspond directly to absorption bands in the BCB [50, 74]. Since this FSS design is fabricated without a ground plane, the absorption peaks appear to manifest themselves as increases in reflectivity due to the rapid variation in the real part of the refractive index of BCB near the loss bands. It is noted that to generate the figure, a new crossed-dipole full array was fabricated since the sacrificial SiO_2 layer of the sample that moved forward in the fabrication would have altered the reflectivity spectra due to the Reststrahlen features in SiO_2.

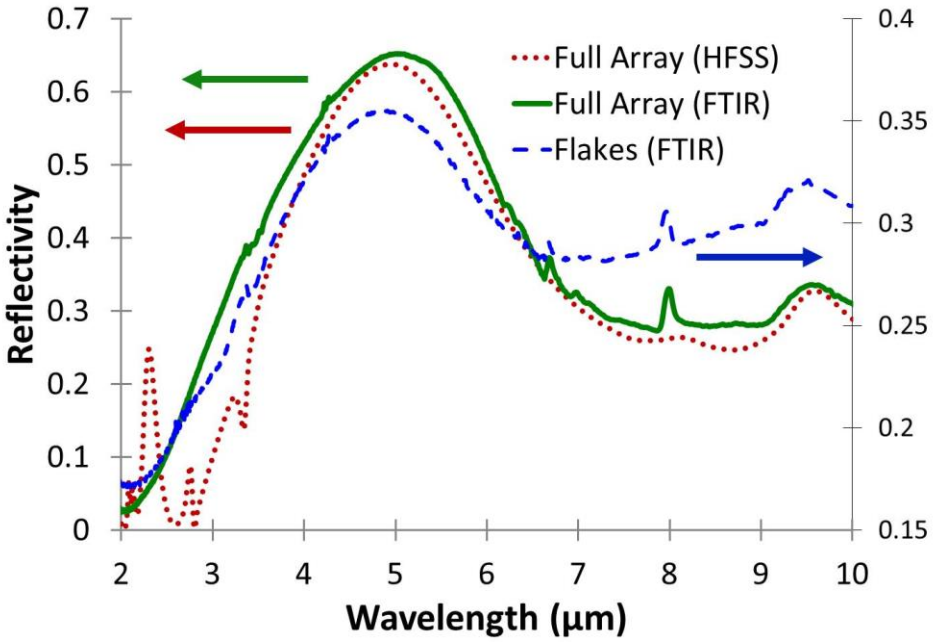

Figure 10. Spectral reflectivity of the crossed-dipole flakes versus that of the full array. Measured reflectivity of the flakes (in blue) is plotted on the right axis, while the measured reflectivity of the full FSS array (in green) and the simulated full array reflectivity (in red) are plotted on the left axis.

3.4 Square-Loop Flakes with Ground Plane Symmetry

After showing the fabrication throughput concept was feasible with crossed-dipole FSS, a square-loop FSS utilizing a standoff layer and ground plane was attempted. The inclusion of the ground plane resolves the potential issues stemming from two transparent FSS-embedded particles lying on top of each other. Square-loop FSS designs possess a fundamental resonance wavelength that scales proportional to the perimeter of the loop, although again at this point in the research plan, the focus was more on development of the fabrication method. A circuit analog has been derived for square-loop FSS [35]. In general, the resonance of the square-loop FSS is broader than that of the crossed-dipole FSS. This is due to the element geometry itself as well as the decreased inter-element spacing relative to crossed-dipole designs [6]. For the same reasons, a square-loop FSS tends to behave in a more omnidirectional manner than crossed-dipole FSS. Figure 11 is a schematic showing a single-square-loop FSS particle before etching. For the square-loop FSS, the inclusion of the ground plane along with a layer of dielectric underneath the elements creates a resonant cavity. The ground plane acts as a good reflector, while the dielectric layer serves to create cavity resonance conditions at wavelengths that correlate to resonant modes in the far-field spectra. As was the case with the crossed-dipole FSS, the square-loop FSS included an overlayer of the dielectric for both structural stability and protection of the elements during processing. The flake fabrication throughput was similar to that of the crossed-dipole flakes, with the addition of a wet Cr etching step for the ground plane and an additional plasma etch for the BCB layers underneath the ground plane.

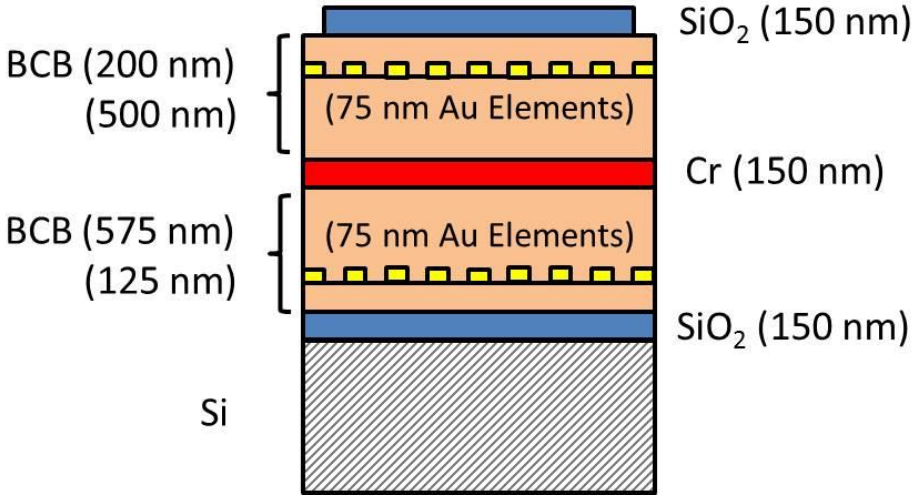

Figure 11. Schematic of a square-loop flake, showing the thickness of each layer.

Figure 12 is an SEM micrograph of a single square-loop flake, showing a fabricated example of the flake design. The difference between this and the previous FSS flake fabrication (the crossed-dipole flake in Figure 9) is the inclusion of a ground plane and the removal of the guard ring (the perimeter ring unpopulated with elements) around the perimeter of the defined flakes. For the crossed-dipole flakes, the alignment of the etch mask to the FSS elements facilitated inclusion of the guard ring since alignment marks could be included in the crossed-dipole lithography. Here, the opaque ground plane prohibits convenient alignment of the etch mask to the FSS elements. It is clear that the inclusion of square-loop elements in the open areas of the SiO_2 etch mask has added complexity to the BCB etching process, although it is not believed that the jagged edges of the square-loop flakes would create problems with possible implementation in a binder or in the eventual application as a coating. As will be shown later by experimental data, the serrated edges do not critically inhibit the resonance of the array. Figure 12 also shows (toward the right of the image) an agglomeration of Au elements that have been left over by the BCB etch process.

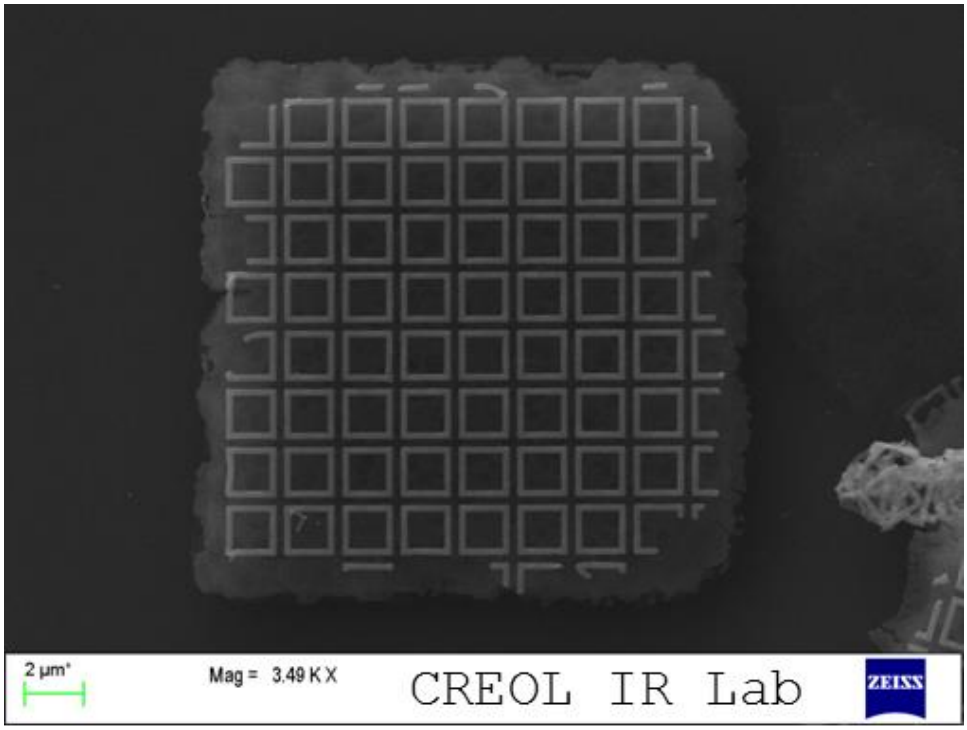

Figure 12. SEM micrograph of a single square-loop flake.

Figure 13 depicts a square-loop flake on its edge, such that the cross-sectional structure can be seen. This figure shows that the thickness of the entire assembly is roughly that of the intended 1.55 µm thick total stack. It is clear that the Au elements are mostly immersed in BCB, and that the structure of the flake is symmetric about the Cr ground plane. Again, the rough edges created from the square-loop fabrication process are shown along with some Au elements left over from the BCB plasma etch. The square patch visible in the bottom-right is an artifact left over from one of the Au lift-off steps. The exposed sections of the Cr ground plane appear porous in this image, which is assumed to be a result of exposure to the wet Cr etch.

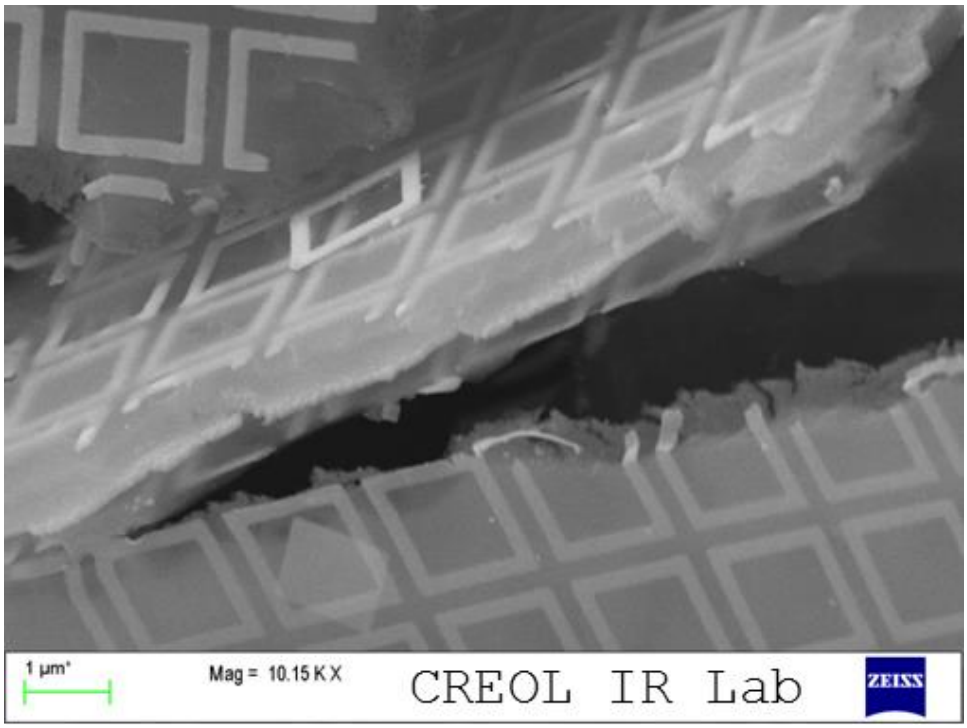

Figure 13. Cross-sectional SEM micrograph showing a square-loop flake on end.

Figure 14 shows the measured and simulated spectral reflectivity data sets for the square-loop flakes. Again, the measured (green) and simulated (red) spectral reflectivity of the full FSS array is plotted on the left axis while the measured spectral reflectivity of an area containing the FSS flakes (blue) is plotted on the right axis. It can be seen that all three data sets have a similar spectral shape, with high reflectivity centered near 7 µm and decreasing reflectivity toward 3 and 11 µm. As was the case with the crossed-dipole FSS, the discrepancy between the full array and the flakes is primarily due to the proportion of flakes filling the input field of the FTIR. The topic of fill factor will be discussed in the following section. The drop in reflectivity seen in Figure 14 near 8 µm and 9.5 µm corresponds directly to absorption bands in the BCB [50, 74].

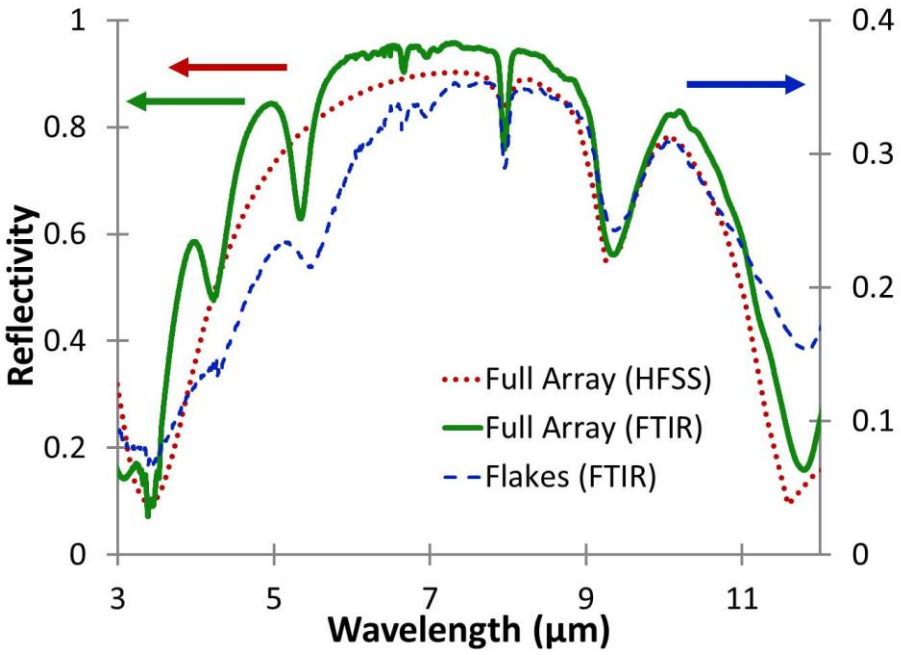

Figure 14. Spectral reflectivity of the square-loop flakes versus the full array. Measured reflectivity of the flakes (in blue) is plotted on the right axis, while the measured reflectivity of the full FSS array (in green) and the simulated full array reflectivity (in red) are plotted on the left axis.

3.5 Discussion

Since the fabrication method yielded a random distribution of flakes, sample areas with high concentrations were sought out for measurement. Figure 15 is an SEM micrograph showing a section of the collected field of square-loop FSS flakes, with areas of high and low flake concentrations. The image confirms that the flakes are roughly uniform in size, and that they have a tendency to lie flat unless one or more flakes overlap. The bright areas are due to charging of the dielectric layers.

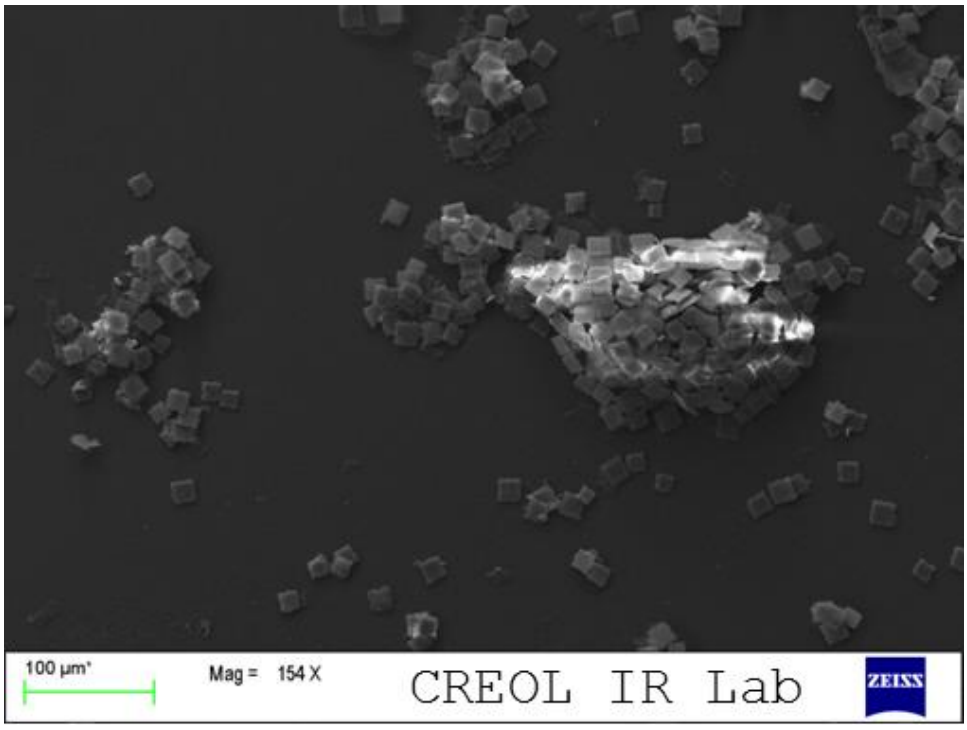

Figure 15. SEM micrograph showing a typical assortment of square-loop flakes after collection.

Figure 16 is an SEM micrograph depicting a selection of square-loop flakes filling an area that is roughly the size of the input field of the FTIR microscope that measures spectral reflectivity. (At the sample plane, this is a circular area with a diameter of approximately 100 µm). This image shows the same ragged edges and loose elements that have been observed in the square-loop fabrication process in previous figures. From images such as this, it is estimated that in areas of high concentrations of flakes, the majority of them are situated within ±15° from normal incidence, which is within the angular spread of the FTIR reflectivity measurement. An estimate of the spatial fill factor of flakes in this image can be made by placing a grid over the image and comparing the flake-filled sections to the voids. In Figure 16, this technique yields a spatial fill factor of roughly 65%, although this estimate is diminished when considering those

flakes at angles too large for the FTIR to measure a specular reflection. It is noted here that the reported angular distribution and spatial fill factor are heuristic.

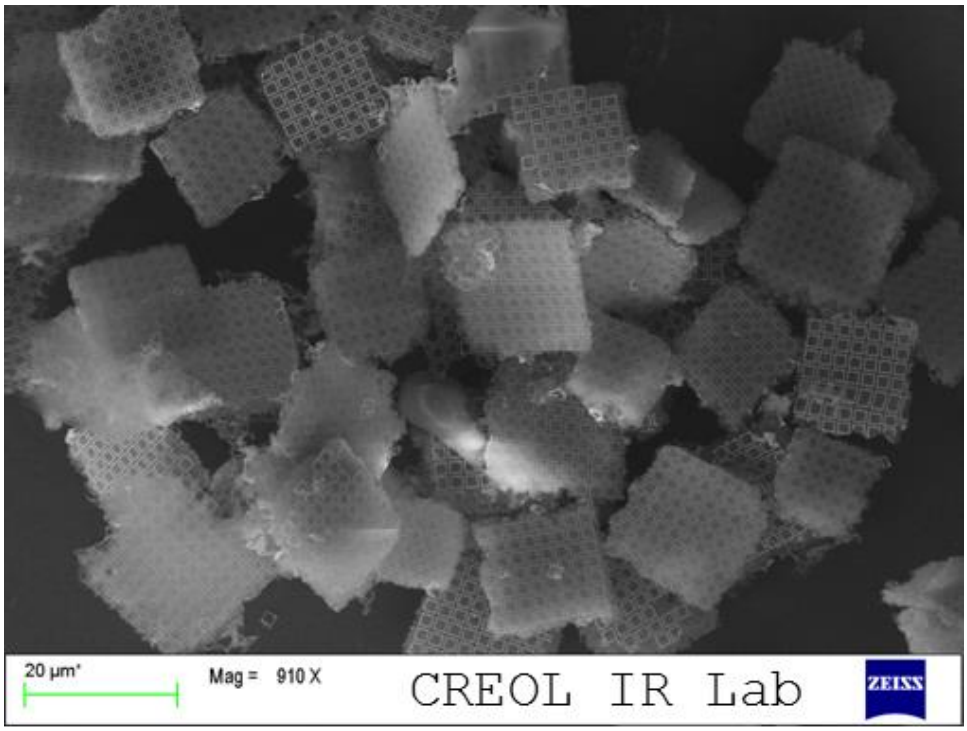

Figure 16. SEM micrograph showing a high density of square-loop flakes occupying an area approximately the size of the FTIR microscope measurement area.

The FSS-embedded flakes discussed in this chapter have included simple elements with square symmetry, such as crossed dipoles and square loops. The work thus far has been primarily concerned with the feasibility of producing these flakes and making meaningful measurements. As such, no specific spectral response has been required and none has been sought. The analysis of FSS typically considers an infinite-by-infinite array of unit cells, using the Floquet method. Thus, the design of one unit cell dictates the entire array. The FSS flakes contain a finite-by-finite array of unit cells (on the order of 10×10). Since the FSS response is contingent upon its placement in an array as well as the element geometry and the material properties of the

structure, it is expected that the electromagnetic response of the finite arrays will diverge from that of the infinite arrays. The RF literature indicates that the spectral response of FSS on the order of 10×10 unit cell elements is not significantly different from an infinite array of unit cell elements [6, 75, 76]. Thus, it is apparent that the results of design and simulation of infinite-by-infinite arrays can, to first order, predict the spectral properties of the truncated arrays. For purposes of a proof of concept, this chapter assumes the response of the infinite array be the baseline for comparison of the fabricated flakes. (An investigation into the effects of array truncation in infrared FSS is presented in Chapter 5).

Figures 10 and 14 both show that the spectral reflectivity contrast between the areas of high and low reflectivity for the flakes is attenuated as compared to the full array measurements and simulations. This is due to a combination of the fill factor of flakes within the FTIR field, the effects of flakes overlapping, and the presumed effects of array truncation. The spatial fill factor is representative of the collection method. In fill factor considerations, the crossed-dipole flakes have the disadvantage of a row of elements being removed from each side due to the guard ring, although the guard ring gives the advantage of a much cleaner fabrication process. Since the crossed-dipole flakes were fabricated without a ground plane, the overlap of flakes leads to a problem much more complex than has been simulated, as the spectral response is now affected electromagnetically by the overlap.

Both the crossed-dipole and square-loop flakes share the issue of an induced angle of incidence upon overlap. Although it is difficult to quantify, Figure 16 seems to indicate that a majority of the square-loop FSS particles lay near normal incidence, within the 10 degree to 25 degree (half angle) FTIR field of view. To further consider the effects of angular distribution, the square-loop FSS array was simulated in HFSS with respect to varying angle of incidence. This is

shown in Figure 17. As can be seen in the figure, the reflectivity spectrum of the square-loop design is quite robust with respect to angle of incidence. This is somewhat expected due to the small inter-element spacing [6]; however, there exists a slight dip at ~5.5 μm that is seen to grow with increasing angle of incidence. A similar dip in reflectivity is observed in Figure 14, which may to some degree be attributed to the non-normal, average incidence angle of the measured aggregate.

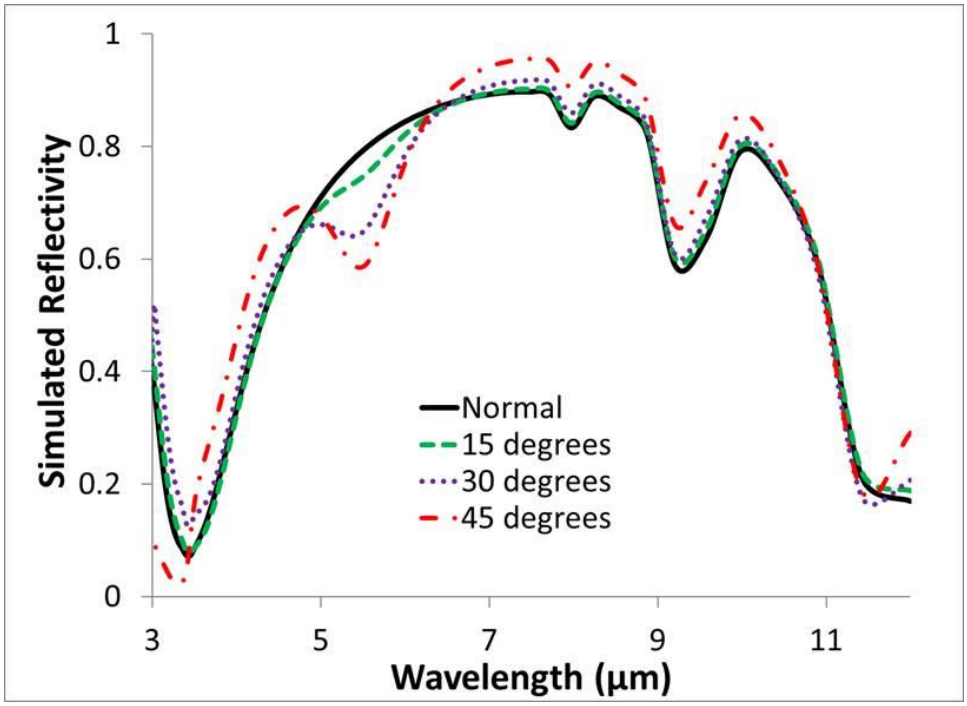

Figure 17. Simulated reflectivity versus incident angle for the square-loop FSS array.

CHAPTER FOUR: NEAR-FIELD INVESTIGATION OF SQUARE-LOOP INFRARED FREQUENCY SELECTIVE SURFACES

Experimental research involving infrared FSS has historically been focused on far-field properties, as most designs are intended toward filtering applications or spectral modification in the far-field regime, although recent publications have seen a trend toward near-field research. Characterization of infrared FSS samples in the far-field is typically carried out using robust turnkey systems such as FTIR, whereas near-field measurement systems are often custom built and complex in terms of operation. Near-field measurements on infrared FSS are valuable for various reasons. One example is the corroboration of far-field simulations using finite-element analysis, where it is the local electric field that truly dictates the far-field results. Moreover, near-field measurements can yield insight into complex FSS phenomena that are difficult to simulate. The aim of this chapter is to introduce the utility of near-field measurements in infrared FSS research. Specifically, square-loop FSS will be studied, as this type of design is considered in the FSS flake results shown in the previous chapter. Additionally, the near-field results presented here set the precedent for the more detailed investigation which will be presented in Chapter Five regarding the effects of array truncation in square-loop infrared FSS.

This chapter presents the measurements and simulations of the near-field and far-field optical response of two separate square-loop designs [77]. This set of structures was designed to be resonant under the conditions of the s-SNOM apparatus that was described in Chapter Two as operating with 10.6 μm excitation at 60 degrees off-normal angle of incidence. The s-SNOM results show resonance in two different square-loop structures in terms of local electric field

amplitude and phase. In both cases, the results are generally consistent with HFSS simulations. Furthermore, far-field measurements from FTIR yield additional insight into the resonant conditions of the two square-loop FSS structures. This work shows that the s-SNOM is capable of analyzing the near-fields on infrared FSS structures and gives promise to efforts that would attempt to analyze more complex structures.

4.1 Design and Fabrication

The square-loop infrared FSS structures presented in this section were designed in HFSS using the Floquet port method. This involved variation of the geometric parameters until the optimum resonance conditions were met. Here, strong far-field absorptivity in the simulations corresponded to strong resonance in the near-field. Two designs were investigated. The first design had a fundamental resonance at 10.6 μm, while the second design had a harmonic resonance at 10.6 μm. *Harmonic* in this case means that for the particular structure, illumination at 10.6 μm was effectively double the fundamental resonant frequency. In both cases, the structures were designed to be resonant at 60 degrees angle of incidence. Both designs used a periodicity of 5 μm. The fundamentally resonant loops had loop edge lengths of 2.0 μm, while the harmonically resonant loops had edge lengths of 3.75 μm. The designs chosen for fabrication are shown by the simulated results presented in Figure 18. Here, the absorptivity at 10.6 μm, 60 degrees angle of incidence is plotted with respect to the edge length of the square-loop unit cell element. It can be seen that the design exhibits peaks in absorptivity due to resonant conditions at edge lengths of 2.0 μm and 3.75 μm. The inset graphics of Figure 18 show the simulated local electric field 25 nm above the square loops; a dipolar behavior is noted for the 2.0 μm loops while a quadrupolar behavior is noted for the 3.75 μm loops. (The inset simulations are meant to

be purely qualitative: blue corresponds to positive field values, while red corresponds to negative field values).

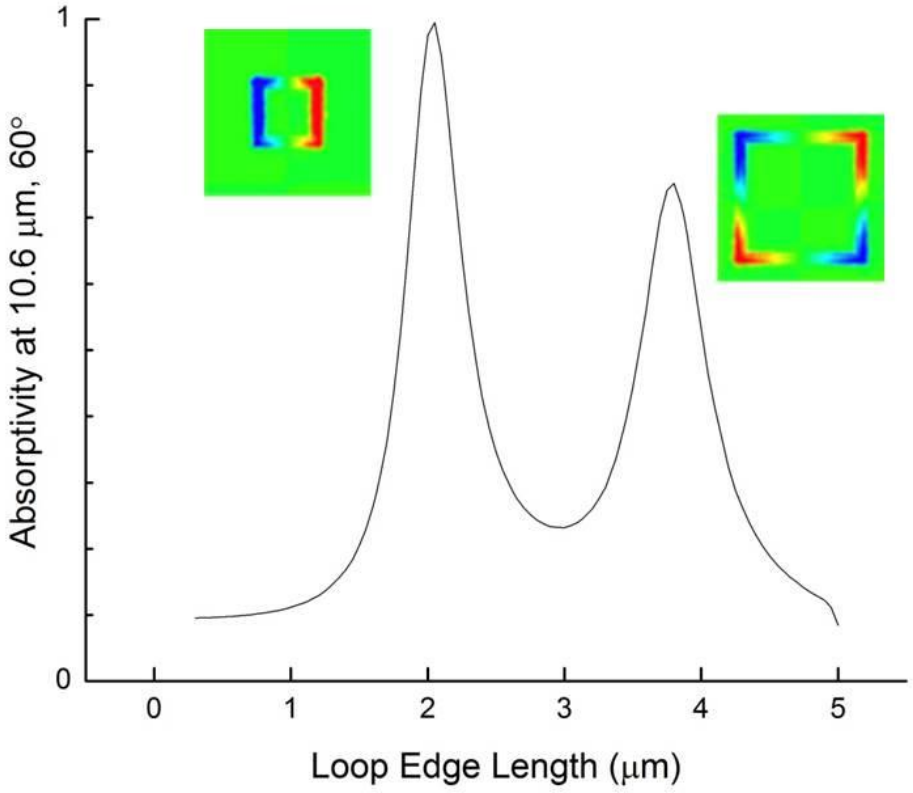

Figure 18. Simulated absorptivity at 10.6 μm, 60 degrees angle of incidence with respect to square-loop edge length. Insets depict simulated electric field 25 nm above the loops, showing dipolar behavior for an edge length of 2.0 μm and quadrupolar behavior for an edge length of 3.75 μm.

Representative SEM images depicting the fabricated FSS arrays can be seen in Figure 19. The designs used an optically thick Al ground plane, a 1.2 μm thick dielectric standoff layer of BCB, and 75 nm thick Al square-loop elements. The FSS structures were fabricated on clean Si wafers; each array comprised an area of 2 mm × 2 mm. The Al ground plane as well as the Al element material was deposited by thermal evaporation out of an alumina lined filament. The BCB was deposited via spin coating and curing in an inert environment. The elements were

created by electron-beam lithography, metallization, and liftoff, using the Leica EBPG 5000+ system described previously.

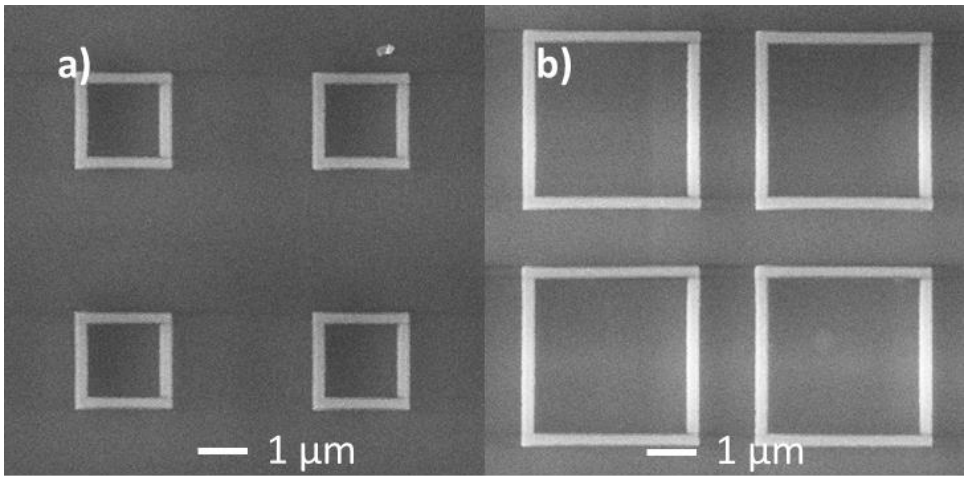

Figure 19. SEM micrographs of the 2.0 µm square-loop FSS structures (a) and 3.75 µm square-loop FSS structures (b).

4.2 Near-Field Results

The local electric field for the square-loop samples was investigated spatially using s-SNOM with 10.6 µm excitation. The measured and simulated near-field signal polarized normal to the sample is shown in Figure 20, for the 2.0 µm square loops. The measured values show a strong resonant signal with a good qualitative agreement to the simulated results. The simulations were carried out using Floquet analysis to approximate the quasi-infinite arrays. With strong amplitude on either side of the square loops and corresponding phase transition from one side to the other, Figure 20 shows a dipolar field distribution corresponding to the fundamental resonant mode for a square-loop FSS. As will be seen in many of the near-field measurements shown in this dissertation, the amplitude appears to be stronger near the top of the loops as compared to the bottom. This behavior is observed because when the lower sections are

being scanned, the upper sections of the loop are shadowed by the AFM cantilever. Some discrepancy is noted between theory and experiment for the reported phase values. To a certain extent, this is because of the phase wrapping, where very small fluctuations between $+\pi$ and $-\pi$ are accentuated due to the sign flip. Additionally, it is noted that the phase values reported are considerably less reliable over regions where the amplitude approaches zero. Moreover, a portion of the discrepancies observed between theory and experiment can be attributed to the differences in excitation phase. Experimentally, the s-SNOM scans the sample while keeping the excitation and AFM cantilever stationary, whereas the simulations use plane wave excitation with a phase gradient in excitation across the sample due to the angle of incidence. Thus, each point in the experimental data is excited with the same phase, while the simulations have variation in excitation phase from the top to the bottom of the loops.

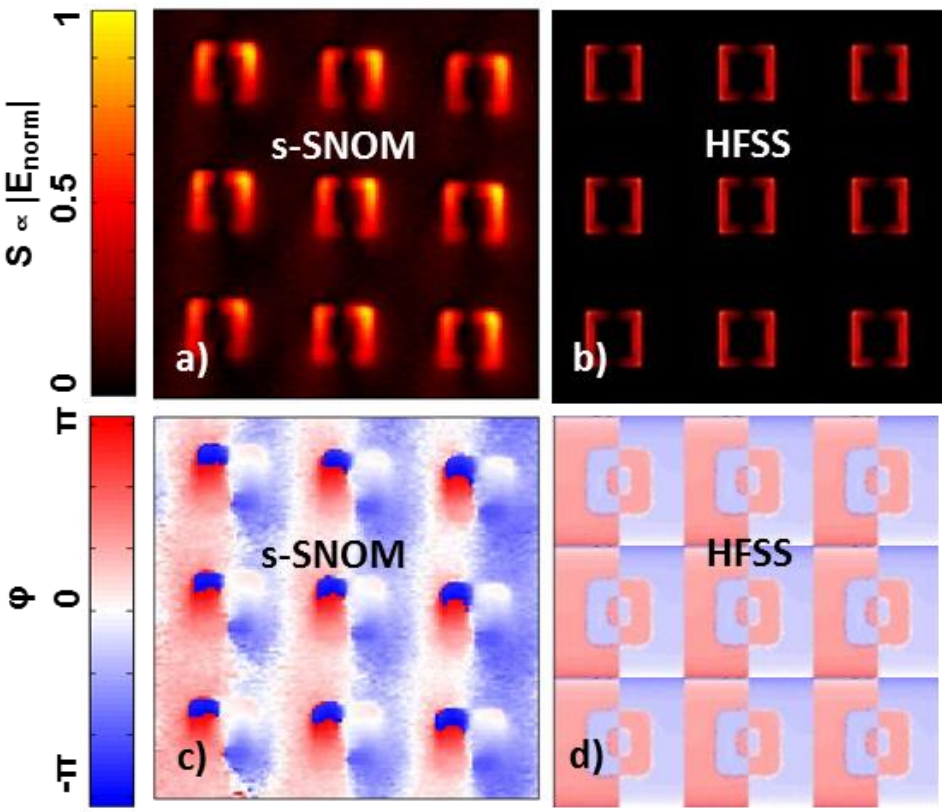

Figure 20. Measured amplitude (a) and phase (c) as well as simulated amplitude (b) and phase (d) near-field imagery corresponding to the 2.0 μm square-loop FSS design.

Figure 21 portrays the measured and simulated near-field amplitude and phase results for the 3.75 μm square-loop FSS design. Here, strong amplitude is observed at the four corners of each loop, with a minima near the center of each edge length. Accordingly, there is a phase transition toward the center of each loop in both the horizontal and vertical directions. This behavior in amplitude and phase is indicative of a quadrupolar mode which is excited at twice the frequency of the fundamental resonance of the structure, implying that the fundamental resonant frequency of the larger square-loop FSS exists somewhere in the far-infrared. Again, the measured results compare well qualitatively with the simulations. The presence of the quadrupolar mode was investigated in simulations. In the computations, this mode only exists

where the angle of incidence is 35° or greater from normal. (A weak dipolar pattern exists at smaller incident angles). This finding is consistent with the fact that the quadrupolar mode is a so-called *dark mode* that cannot be excited by a plane wave at normal incidence, but can be excited at larger incident angles.

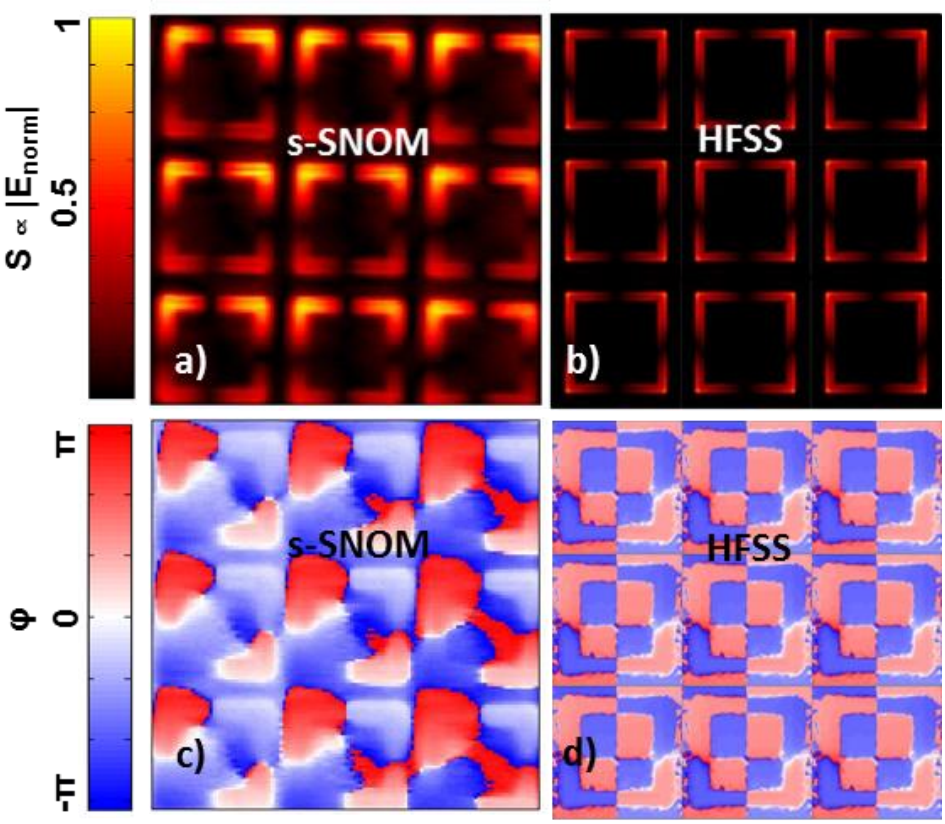

Figure 21. Measured amplitude (a) and phase (c) as well as simulated amplitude (b) and phase (d) near-field imagery corresponding to the 3.75μm square-loop FSS design.

4.3 Far-Field Results

The experimental and simulated absorptivity for both square-loop arrays is plotted in Figure 22. It is noted that these data sets were taken using the FTIR at the Advanced Light

Source, at Lawrence Berkley National Laboratory. This instrument is slightly different as compared to the FTIR discussed in Chapter Two. It has a 50 μm circular measurement area on the sample and uses a Schwarzschild objective, which measures an 18-40.5 degree angular distribution of reflectivity. For the small loops (plotted in blue), a broad absorptivity peak can be observed in the long wave infrared (LWIR), centered near 10 μm, with absorptivity tailing off toward the longer wavelengths. The spectra of the large loops (plotted in green) also shows a broad, although much weaker, absorptivity centered near 10 μm along with a strong absorptivity peak between 20 and 25 μm. For the small loops, the peak centered near 10 μm corresponds to the fundamental resonant mode of the structure. For the large loops, it is the peak centered near 24 μm that corresponds to the fundamental resonant mode, while the absorptivity spectra near 10 μm may offer some indication of the second harmonic mode that was observed in the near-field as well. The discrepancy for the large loops in the far-IR between theory and experiment are likely due to the sharp drop in system sensitivity at wavelengths greater than 20 μm. Because they are measured in an annulus centered at normal incidence, the reported resonances are shifted slightly from the optimized design that had strong resonance at 10.6 μm and 60 degrees off normal angle of incidence; it is noted that this behavior is consistent with simulated data at normal and 60 degrees off-normal incident angles.

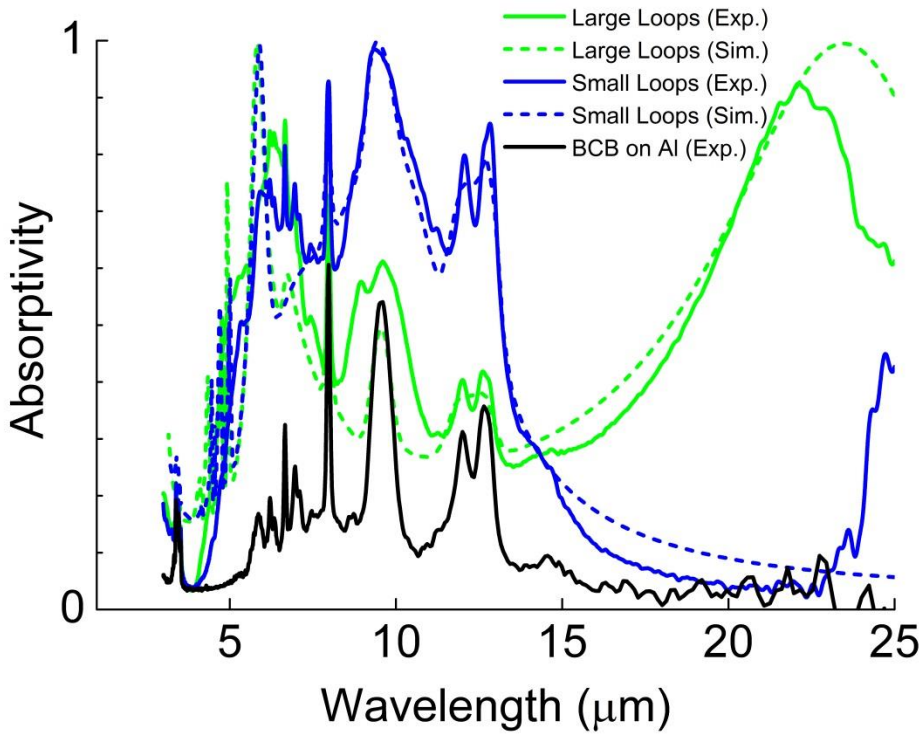

Figure 22. Measured and experimental spectral absorptivity for the 2.0 μm loops (blue), the 3.75 μm loops (green), and bare areas of the same including only BCB on Al (black).

To highlight the absorptive features observed in the square-loop arrays which emanate from material losses in the BCB layer, the spectra of the substrate (1.2 μm BCB on 150 nm Al) is plotted in Figure 22 (in black). Looking at the simulations corresponding to the square-loop arrays, it is clear that the optical properties derived from ellipsometry for BCB on Al, which were utilized in the modeling, depict the absorptivity peaks for the BCB polymer near 9.5 μm, 12 μm, and 12.4 μm. However, as seen in the amplitude and bandwidth of the peaks, the FEM simulations do not completely predict the complex interactions existing between the absorptive BCB layer and the square-loop FSS. While it is clear that the resonant absorptivity of the 2.0 μm square loops rises far above that of the substrate, it is difficult to determine whether the slightly enhanced absorptivity of the 3.75 μm loops near 10 μm over that of the bare substrate is due to weak excitation of the quadrupolar mode (owing to the 18-40.5 degree reflectance measurement

geometry) or some other mechanism. The difficulties in spectral identification of FSS resonances come about due to the absorptivity peaks observed in the BCB layer. Because the existence of the FSS elements spatially alters the interaction of light with the BCB layer, the substrate absorptivity cannot be conveniently subtracted from the FSS absorptivity to reveal the true FSS resonances.

4.4 Discussion

The results presented in this chapter depict near- and far-field measurements on two different square-loop infrared FSS designs. The designs were identical aside from the fact that the loop size in one design was 2.0 μm and in the other it was 3.75 μm. At 10.6 μm and 60 degrees off-normal angle of incidence, the smaller loop array displayed a fundamental resonance while the larger loop array displayed a harmonic resonance. This was confirmed in the far-field via FTIR since the fundamental mode was visible as an absorptivity peak for the small loops, while the fundamental mode and, possibly, the harmonic mode exhibited absorptivity peaks for the large loop structure. In the near-field, the small loops were observed to display a clear dipolar local electric field amplitude and phase relationship while the large loops displayed a convincing quadrupolar behavior.

Perhaps the most interesting result presented in this chapter is the quadrupolar behavior of the large loop array in the near-field at 10.6 μm, 60 degrees off-normal excitation. Looking at Figure 22, it is difficult to predict this quadrupolar (or any other mode) for the large loop array due to the predominance of the absorption bands in the BCB spacer layer. While the set of experiments discussed in this chapter show the utility of s-SNOM in the measurement of infrared FSS structures, observation of the quadrupolar mode shows explicitly that s-SNOM can be a

valuable tool to identify modes in resonant structures, where the material absorption and complex antenna-substrate interactions tend to hide the resonant behavior from far-field measurements.

CHAPTER FIVE: INVESTIGATION OF TRUNCATION EFFECTS IN INFRARED FREQUENCY SELECTIVE SURFACES

Classically, FSS are designed and simulated in the environment of an infinite array, which reduces the computational resources needed for simulation by greatly simplifying the mathematics involved. In most applications, the assumption of an infinite array is perfectly reasonable, considering that the fabricated arrays tend to be quasi-infinite with respect to a unit cell in the center of the patterned area. However, in the flake based coating discussed in this dissertation, the arrays are on the order of 20 μm × 20 μm, containing roughly 10×10 elements. Certainly, the reduction of the array dimension has some effect on the far-field spectral response; however, it is not intuitive how these truncation effects may alter the response. With that in mind, investigation of truncation effects in infrared FSS is beneficial for two reasons. First, it is advantageous to see the strength of these effects and the extent to which they must be included in the analysis. Second, it is useful in that the results may give insight in the form of design changes that may lead to a better final result in the eventual FSS flakes, or any other application using FSS sub-arrays.

During the research relevant to this dissertation, a thorough literature review has yielded no results concerning the effects of array truncation for resonant structures such as FSS at infrared frequencies. As this is the case, work in other regimes of the electromagnetic spectrum, where the implications of truncation on the far-field and near-field response are discussed, are worth studying for comparison. Several studies have been carried out at RF, which show that the resonant behavior of truncated FSS arrays is shifted toward shorter wavelengths as compared to

that of the infinite array [78, 79, 80, 81]. Also at RF, Ekpo, Batchelor, and Parker have shown experimental near-field mapping of the transmission through a 3x3 array [82].

There are a few examples in the literature that discuss truncation behavior at frequencies higher than LWIR. Shifting of the resonance condition in asymmetric metamaterial structures in the near-infrared has been shown by Fedetov et al. [83]. Red-shifting of the Fano resonance wavelength with respect to increasing number of particles in nanoclusters has been shown by Bao, Mirin, and Nordlander [84]. Red-shifting of the longitudinal mode plasmon resonance energy of nanoparticle chains with increasing chain-length was shown by Maier, Kik, and Atwater [85, 86], and then later by Willingham and Link [87]. While these examples do not completely replicate the resonant conditions and truncation effects of infrared FSS, the results presented in this chapter show similar behavior in terms of spectral shifting of resonance upon array truncation, as the collective resonant wavelength of finite arrays is seen to red-shift as the number of elements in the arrays is increased.

During the course of this dissertation, several experimental studies have been undertaken to investigate the effects of truncation in infrared FSS arrays. First, truncated arrays were fabricated using BCB as a dielectric standoff material, in a design similar to the square-loop FSS described in Chapter Three. Since these samples closely mimicked an organized version of the FSS flakes, which are the experimental baseline, proceeding in this way seemed valid. However, it soon became clear that the results of interest might be affected by the absorptivity peaks, which exist due to the BCB layer. To better understand the effects of truncation on the fundamental resonant mode, the BCB was replaced by ZnS as a dielectric for the design. To that end, a square-loop FSS was designed with fundamental resonance at 10.6 μm at an angle of incidence of 60 degrees from normal [88]. Patterned areas containing the original design, as well

as truncated arrays containing 11×11, 7×7, 5×5, 3×3, and isolated unit cells were fabricated on a single substrate. The patterned areas were characterized in the far-field at 60 degrees off normal utilizing FTIR as well as in the near-field using s-SNOM. The presented results show that in the far-field, the wavelength of peak resonance is blue-shifted upon truncation, while in the near-field, the effects of truncation manifest as spatial non-uniformities in the local electric field amplitude and phase [88].

5.1 Initial Observations of Truncation Effects

While the main emphasis of this chapter is on the investigation of truncation effects in infrared FSS using square loops on ZnS, an earlier experiment using BCB as the dielectric material is presented here both to motivate the choice to move to ZnS as the dielectric material for this portion of the research as well as to show that the shifting of resonant wavelength upon truncation is a general result. The experiment was carried out by patterning areas containing sub-arrays of N×N FSS unit cells (N being an integer). In particular, sub-arrays of 1×1, 3×3, 7×7, 11×11, 15×15, and "infinite" unit cells were fabricated. Each sub-array was placed with 4 μm separation (edge to edge) between the adjacent sub-arrays.

As always, simulations were carried out in HFSS, using frequency dependent optical constants of the constituent materials derived by ellipsometry. The simulations of the infinite arrays were carried out using the Floquet port method described previously. Attempts were made to simulate the N×N arrays by this method as well, but this proved to be impossible with the computational resources available locally. As this was the case, simulations were run by considering single finite arrays in the computational domain. This was accomplished using plane wave excitation at 10.6 μm and utilizing perfectly matched layers on the external boundaries of the simulation. It is noted that the simulations differ from what was measured experimentally,

since large patterned areas (arrays of truncated arrays) were needed for the far-field characterization.

Fabrication of the samples with BCB as the dielectric began with 150 nm Cr deposited by electron-beam evaporation on clean 3" Si wafers. Then, a 250 nm layer of BCB was deposited by spin coating and curing the polymer. The electron-beam lithography was carried out using the JEOL JBX-9300FS system described in Chapter Three. The square loops had line widths of 250 nm, edge lengths of 1.8 μm and periodicity of 2.18 μm. ZEP 520A-7 was used as a positive-tone electron-beam resist. For metallization, a 90 nm layer of Au was deposited by electron-beam evaporation, using a 2.5 nm Ti adhesion layer. Liftoff occurred in N,N-dimethylacetamide.

Far-field characterization for this initial result was done with FTIR at normal incidence using the microscope attachment, as described previously. As previously stated, for structures with a ground plane the absorptivity can be determined as unity minus the reflectivity. The far-field characterization focused on analysis of the spectra in the LWIR, spanning the wavelengths 8 – 12 μm, to include the fundamental resonance of the FSS. The structures using BCB as the dielectric layer exhibited two absorptivity peaks: a peak due to the resonance of the square-loop FSS and a peak due to a material loss band in the BCB polymer. The spectral absorptivity for the square-loop structures using BCB as the dielectric layer is shown in Figure 23. As can be seen in the figure, the full (infinite) array has an absorptivity peak near 10.6 μm corresponding to the resonance of the square-loop FSS and another peak near 9.2 μm corresponding to the BCB losses. Both the FSS resonance peak and the BCB loss peak display blue-shifting behavior upon array truncation. The infinite array is simulated using Floquet analysis, while the absorptivity of the truncated arrays is calculated using the volume loss density as described previously.

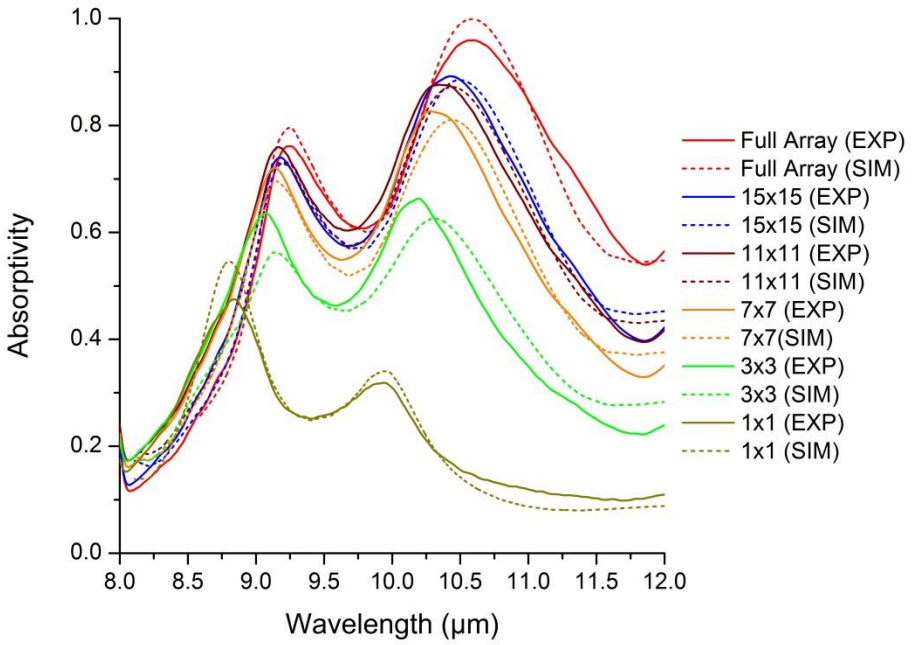

Figure 23. Measured and simulated absorptivity of full and truncated arrays of the square-loop infrared FSS design using BCB as the dielectric material.

5.2 Design and Fabrication

To mitigate any potential interaction between the wavelength of resonance of the FSS and the absorptivity bands in BCB, the square-loop FSS was re-designed using a ZnS dielectric layer. The motivation for this can be understood by observing the optical properties of the two materials, which are shown in Figure 24. The figure depicts thin film optical constants of the two materials as derived from ellipsometry. As can be seen in the figure, the extinction index for BCB exhibits strong absorption bands near 8 μm, 9.5 μm, and 12 μm, which lead to fluctuations in the propagation index. The optical constants of ZnS are relatively flat, with only slight dispersion appearing due to an absorption band in the far-infrared. Thus, designing the sample for the truncation effects experiment using ZnS allows an uncluttered observation of the spectral

shifting phenomena of the fundamental resonant mode, whereas on BCB the behavior of the truncated FSS response may be influenced by the rapid fluctuations in the refractive index in the spectral regions of interest.

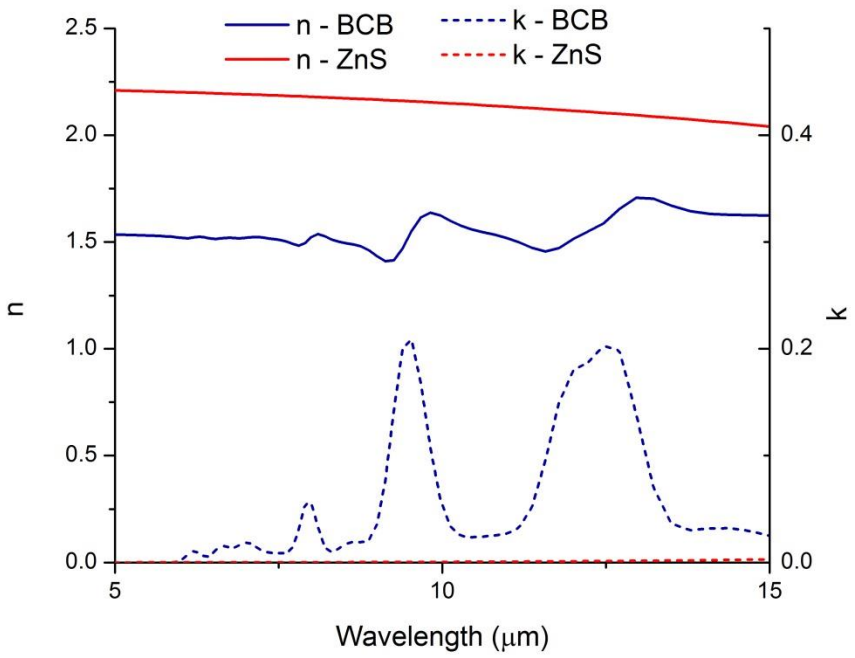

Figure 24. Optical constants of BCB and ZnS as derived by ellipsometry.

In iterative simulations via Floquet analysis in HFSS, the FSS design was optimized for use in the s-SNOM apparatus, with absorptivity at 10.6 μm at 60 degrees off-normal angle of incidence. As was the case in previous designs, the square loops were composed of Au and the structure was fabricated over a Cr ground plane. ZnS was used as the standoff layer due to its transparency over the wavelengths of interest, as was demonstrated in Figure 24. Good adhesion was observed between ZnS and Cr. The optimized design included a ZnS thickness of 320 nm

and a square-loop edge length and periodicity of 1.44 μm and 1.79 μm, respectively. The line width of the loops was 250 nm and their thickness was 75 nm.

To create truncated arrays for study, six areas roughly 3 mm × 8 mm were fabricated on the same substrate. Fabrication of all the samples on the same substrate eliminates the run-to-run discrepancies in the lithography and thin-film deposition that would otherwise exist. Of these patterned areas, one was the original "full array" design, and the others consisted of 11×11, 7×7, 5×5, and 3×3 sub-arrays, as well as isolated unit cells. In all cases, the spacing between adjacent truncated arrays (or isolated cells) was 6.35 μm, which was observed in simulations to have enough fill factor to yield a measurable absorptivity while providing enough isolation to restrict significant coupling between adjacent arrays.

The fabrication of the square-loop arrays was carried out using electron-beam lithography and liftoff. To begin, a clean 4" Si wafer was coated with 150 nm Cr using electron-beam evaporation. Next, the 320 nm ZnS layer was deposited via thermal evaporation from a baffled box. The patterns were defined using the JEOL JBX-9300FS system described previously, with PMMA-A7 as the electron-beam resist. Development took place in a solution of equal parts MIBK and IPA for 2 minutes. The loops were created by metallization of Au via electron beam-evaporation, using a 2.5 nm layer of Ti to promote adhesion. The sample was then placed in NMP for about 24 hours to achieve liftoff. Several exposure matrices were fabricated before the final sample; this was necessary due to so-called proximity effects in the lithography caused by the variation in pattern density with respect to the truncated arrays. These proximity effects were mitigated by varying the exposure for each patterned section as well as biasing the line width of the square loops. Figure 25 shows representative SEM images depicting the patterned sample areas.

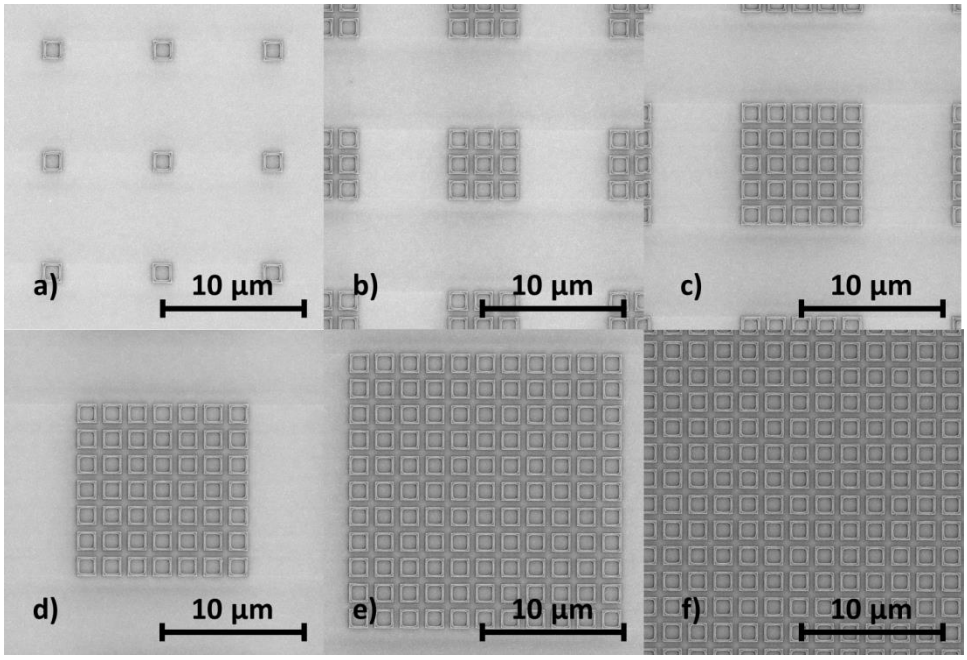

Figure 25. SEM micrographs corresponding to the patterned areas of square-loop FSS on ZnS fabricated to investigate truncation effects: (a) isolated square-loop unit cells, (b) 3×3 arrays, (c) 5×5 arrays, (d) 7×7 arrays, (e) 11×11 arrays, and (f) the quasi-infinite full array design.

5.3 Far-Field Results

The infrared ellipsometry apparatus as described previously was used to measure the spectral absorptivity of the patterned areas using s-polarized light at an angle of 60 degrees off normal. Due to the opaque ground plane, the absorptivity was calculated using the spectral reflectivity by way of Equation 39. Figure 26 shows the measured and simulated spectra, showing that the center wavelength of experimental absorptivity ranges from 10.25 µm for the full array to 9.35 µm for the isolated loops. The decrease in strength of absorptivity is an effect of the decreasing fill factor of unit cells within the measurement area. A similar trend is predicted by the simulations, although the simulated change in peak wavelength is much more abrupt for the 5×5 and 3×3 finite arrays. The full array simulations were calculated using Floquet

mode analysis while the finite array simulations calculated absorptivity via integration of the volume loss density within the computational domain.

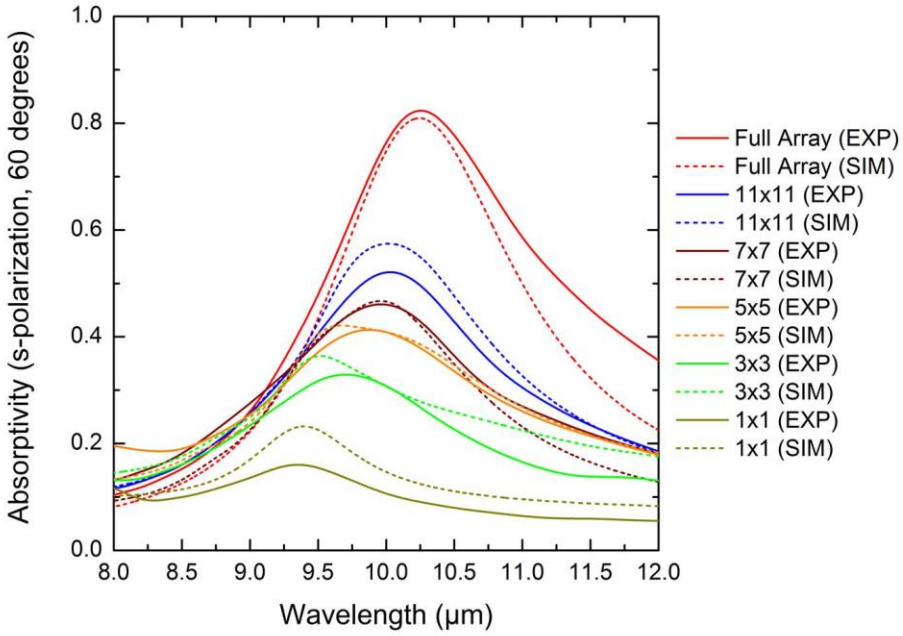

Figure 26. Experimental and simulated spectral absorptivity for the full array as well as the truncated arrays.

It should be noted that Figure 26 indicates a resonant wavelength of 10.25 μm for the original design while it was stated previously that the FSS design was optimized for absorptivity at 10.6 μm. The reasons for this were discovered via SEM: the square-loop structures were found to be slightly smaller than designed and additionally, the corners of the loops were found to be slightly rounded. These effects shifted the wavelength of maximum resonance since this parameter is directly related to the loop perimeter. To provide the proper simulated result, Figure 26 shows simulations that used a loop edge length of 1.39 μm rather than the 1.44 μm design (approximately that which was observed by SEM).

It is additionally noted that the full array absorptivity is seen in Figure 26 to be near 0.8 while the original simulations predicted a near-unity absorber. This discrepancy is due to the geometry of the mask that was used to aperture sections of the sample for FTIR measurement via the infrared ellipsometer. As earlier described, the measurement area of the ellipsometer apparatus is much larger than the 3 mm × 8 mm patterned sample areas, approximately 1 cm × 2 cm at 60 degrees off-normal angle of incidence. As a further complication, the interrogation light is not a uniform beam. Instead, it is an image of the glow-bar source with a "U" shaped intensity profile. This means that the beam cannot be efficiently reduced in size using an aperture to measure samples smaller than the interrogation area.

The intensity profile of the source impinging on the sample was observed with an infrared camera and rectangular masks of 0.008" thick stainless steel were fabricated with an opening in the approximate area where the highest source irradiance was observed. The masks were coated with Zynolyte Hi-Temp black paint to reduce reflections from the metallic mask surface. At 60 degrees angle of incidence, this coating reduced the reflectivity of the steel masks to less than 0.02 as measured directly on the IR-VASE. The smallest aperture mask with acceptable throughput had an opening of 4 mm × 10 mm. This area was slightly larger than the sample areas of interest (3 mm × 8 mm) and some spectral reflectivity of the sample outside of the measured area contributed to the observed results. The area not intended to be measured is approximated geometrically to be 20% of the total mask opening when the finite thickness of the mask is included. Thus, the simulations shown in Figure 26 have been adjusted to take into account the fill-factor of the patterned areas within the measurement as follows.

$$A(\lambda)_{Total} = FF \cdot A(\lambda)_{S.L.} + (1 - FF) \cdot A(\lambda)_{Substrate} \quad (53)$$

Here, $A(\lambda)_{Total}$ is the total simulated absorptivity, *FF* is the fill-factor, the portion of the square-loop patterned areas filling the measurement area, $A(\lambda)_{S.L.}$ is the simulated absorptivity of the arrays, and $A(\lambda)_{Substrate}$ is the simulated absorptivity of the substrate without any arrays. The simulated absorptivity of the bare substrate ranges gradually from 0.070 at 8μm to 0.044 at 12 μm. It is noted that the full array absorptivity was confirmed using near-normal incidence FTIR to have a maximum value of 0.98 near 10.6 μm, consistent with the simulated values.

Figure 27 highlights the spectral behavior seen in Figure 26, by expressing the data in terms of center resonant wavelength and full width at half maximum (FWHM) bandwidth. As can be seen in the figure, the blue-shifting of resonant wavelength upon truncation is quite gradual for both the experimental and simulated spectra. The observed disagreement between theory and experiment seen in the 3×3 and 5×5 arrays may be attributed to the simulations predicting interference effects caused by the perfect spatial and temporal coherence used in the simulated fields, which is not present in the experiment using FTIR with an incoherent glow-bar source. For the FWHM results, both the experimental and simulated values fluctuate upon truncation. The experimental FWHM values are seen to be consistently larger than the simulated values, presumably due to the inhomogeneities and deviations from perfect square-loop geometry which are inherent in the fabrication process.

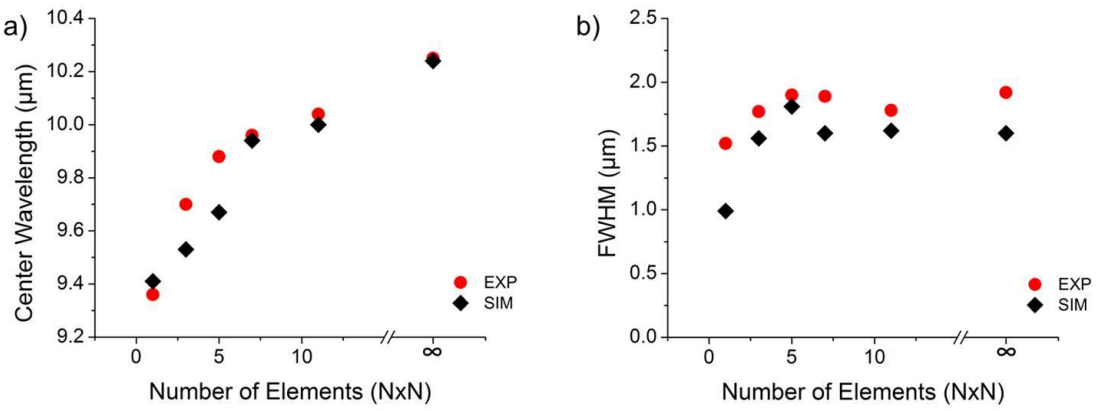

Figure 27. Experimental and simulated center wavelength (a) and FWHM (b) taken from the absorptivity plots shown in Figure 26.

5.4 Near-Field Results

As stated previously, the resonant wavelength of the quasi-infinite square-loop FSS was observed to be 10.25 μm rather than the intended 10.6 μm due to slight differences between the design and the fabricated sample. To more closely match this resonant wavelength, the CO_2 laser was tuned in the s-SNOM apparatus by adjusting the temperature of the recirculating chilled water. The potential range of tuning was observed to be 10.25 μm to 10.62 μm by varying the temperature between 15 and 30 degrees C in increments of 0.2 degrees C, waiting about 30 minutes for the laser to stabilize, and observing the wavelength of emission with a CO_2 laser frequency analyzer (Macken Instruments). Figure 28 shows the wavelength dependence observed in this experiment. It was found that a chilled water temperature of 27.0 degrees C led to a lasing wavelength of approximately 10.25 μm as measured by the frequency analyzer. This emission corresponds to the 10R20 CO_2 laser transition, which has a theoretical wavelength 10.247 μm. It is noted here that all of the experimental and simulated near field results in this

chapter have been obtained using 10.25 μm excitation, the stability of which was verified often using the frequency analyzer.

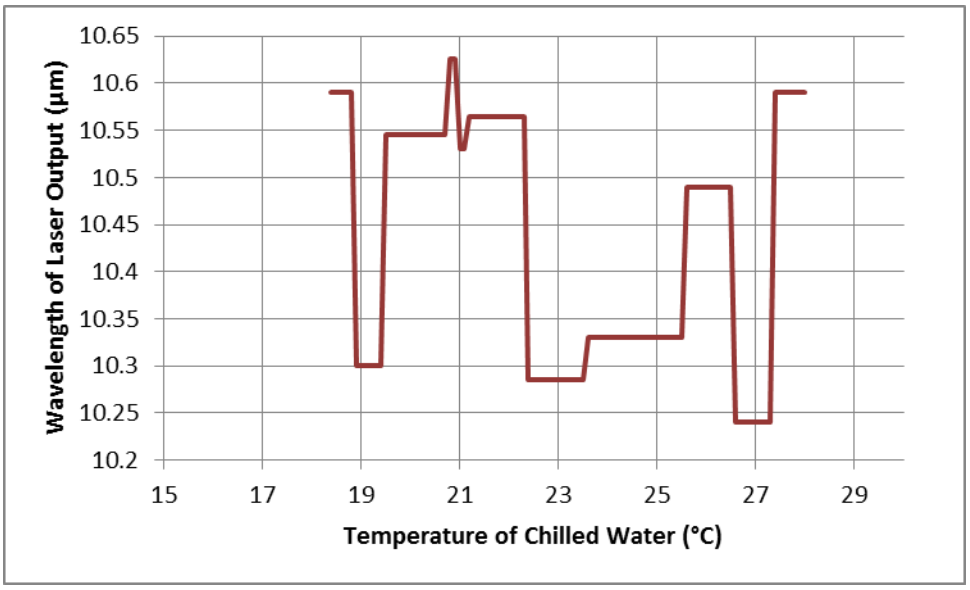

Figure 28. Dependence of laser output wavelength with respect to temperature of the cooling water, as measured by a CO_2 laser frequency analyzer.

Figure 29 depicts the experimental and simulated near-field amplitudes polarized in the direction normal to the sample corresponding to the full array, an 11×11 array, and a 7×7 array. Each data set includes 256×256 data points on a square grid of 22 μm per side. The full array results depict the anticipated symmetric dipole near-field pattern with a high degree of uniformity, for both theory and simulation. Truncation effects are observed as disruptions in this uniformity for the 11×11 and 7×7 arrays. This is seen both in the fact that the overall amplitude is non-uniform in both the horizontal and vertical directions as well as the fact that the dipole minima seen in many columns of the truncated square-loop arrays is shifted from the center as observed in the full array. Insets are included to help distinguish some of the differences more clearly; they depict the fact that the minima observed on the horizontal loop edges have shifted in

the truncated arrays. Due to the symmetry of the sample and the excitation, the field amplitude in the center columns of the truncated arrays is observed to be nearly symmetric. Overall, qualitative agreement is observed between theory and experiment. One example of good agreement is shown by the encircled area in Figure 29 (b) and the corresponding area in the simulation (e).

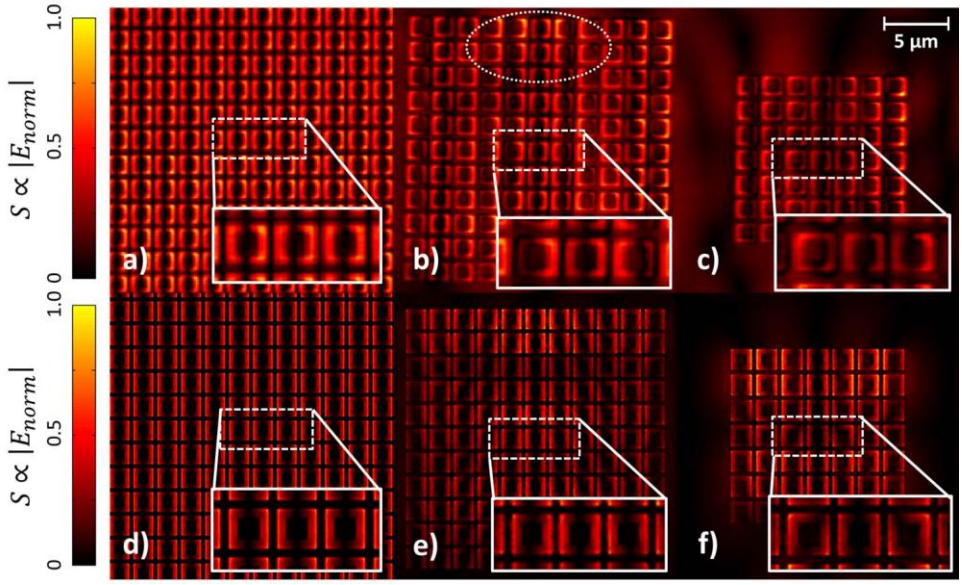

Figure 29. Experimental (a-c) and theoretical (d-f) near-field amplitude results for the full array (a,d), 11×11 array (b,e), and 7×7 array (c,f) patterned sample areas.

The near-field amplitudes polarized in the direction normal to the sample, corresponding to the 5×5, 3×3, and isolated loop structures are shown in Figure 30. As before, the results were obtained by sampling 256×256 data points, although here the sample area is a square with 11 µm per side. As was the case in Figure 29, the effects of truncation for the 5×5 and 3×3 arrays are observed as the disruption of the uniformity which was observed in the full array. For the 5×5 and 3×3 arrays, there is good qualitative agreement between the theoretical and measured images. For example, the experimental and theoretical near-field results for the 5×5 array both

show strong amplitude over the second row of loops. The isolated loop results show some disagreement between theory and experiment. It is believed that these discrepancies are due to background far-field interference, resulting from scattering off the sample and the shaft of the AFM probe. This is more noticeable in measurements of the less resonant structures, such as the 3×3 arrays and the isolated loops.

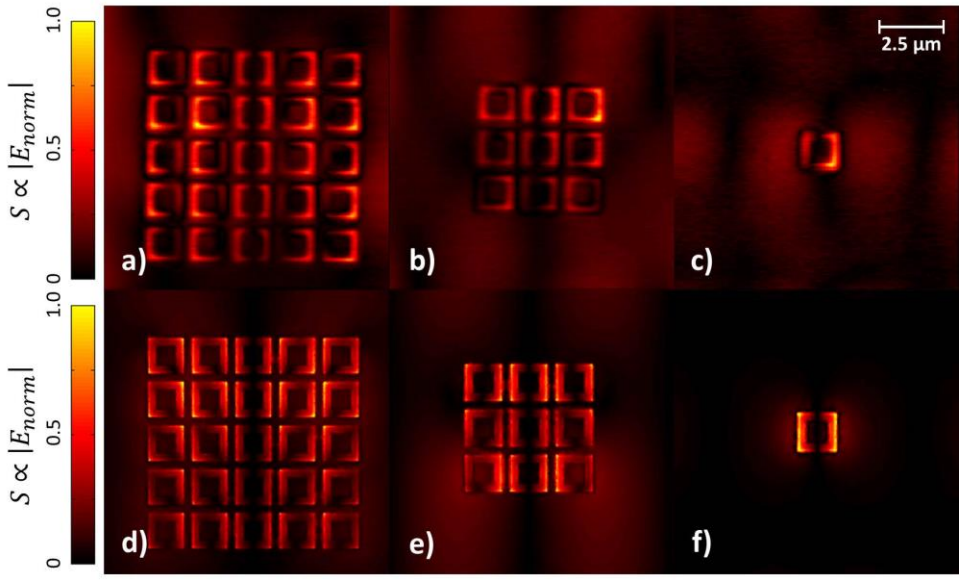

Figure 30. Experimental (a-c) and theoretical (d-f) near-field amplitude results for 5×5 array (a,d), 3×3 array (b,e), and isolated unit cell (c,f) patterned sample areas.

Figures 31 and 32 show the effects of array truncation in terms of the relative phase of the near-field polarized in the direction normal to the sample. Figure 31 shows the cosine of the relative phase for the infinite, 11×11, and 7×7 arrays on a 22 µm square sample area, while Figure 32 shows the cosine of the relative phase for the 5×5, 3×3, and isolated loop arrays on an 11 µm square sample area. The phase figures are taken from the same data sets, and thus correspond directly to the respective amplitude data presented in Figures 29 and 30. In both cases, the cosine of the relative phase is plotted to avoid the graphical anomalies that are typical

between +π and –π when wrapping the phase [89, 90, 91]. The figures depicting phase relationships show essentially the same behavior as the amplitude: a strongly correlated uniformity exists for the full array while truncation brings about disruptions in this uniformity. Additionally, it is noted that that phase images seem to show a collective oscillation for the truncated arrays, such that the truncated arrays themselves are oscillating as a united entity rather than single elements within an array.

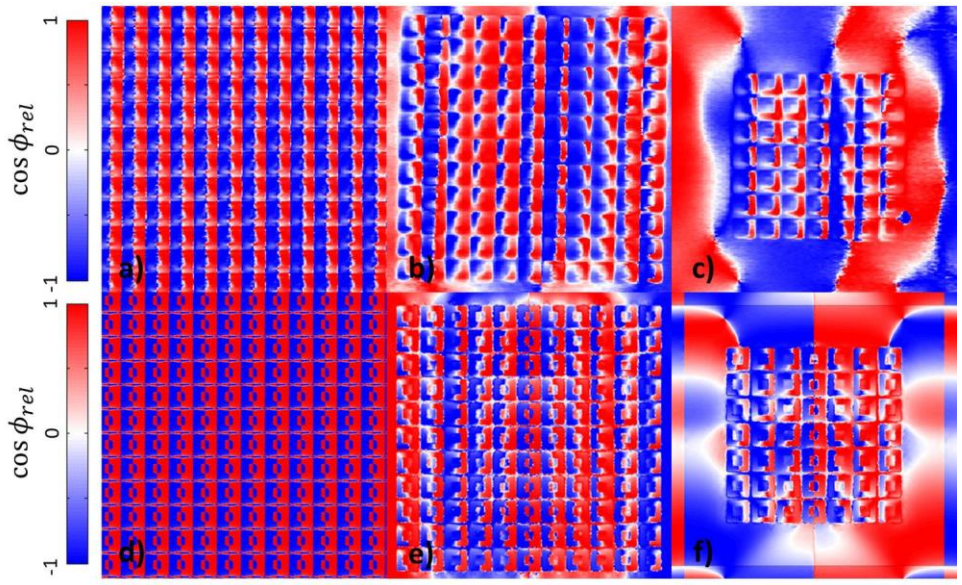

Figure 31. Experimental (a-c) and theoretical (d-f) near-field phase results for the full array (a,d), 11×11 array (b,e), and 7×7 array (c,f) patterned sample areas, plotted as the cosine of the relative phase.

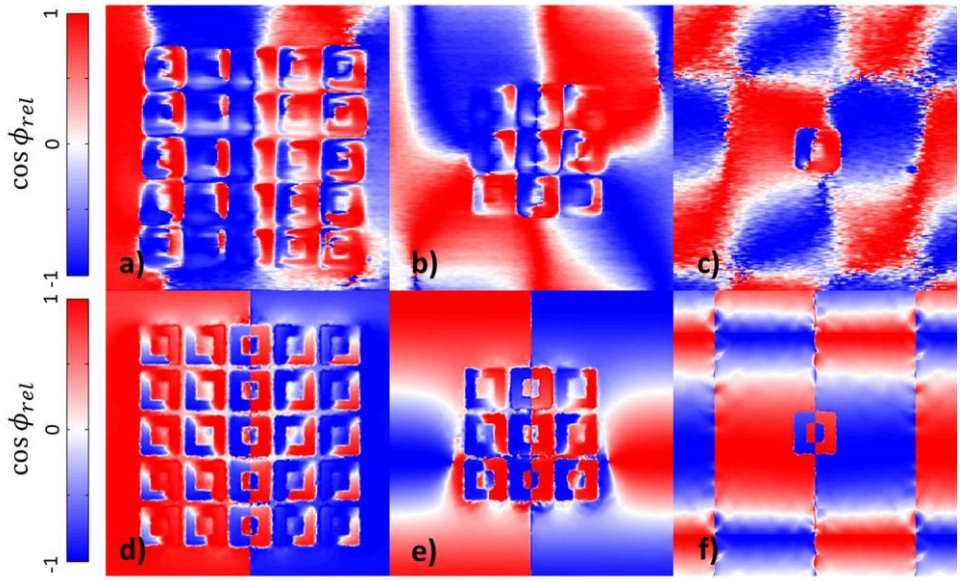

Figure 32. Experimental (a-c) and theoretical (d-f) near-field phase results for 5×5 array (a,d), 3×3 array (b,e), and isolated unit cell (c,f) patterned sample areas, plotted as the cosine of the relative phase.

5.5 Discussion

The most significant result presented in this chapter is the shifting of resonant wavelength upon truncation of the infinite array. In particular, a blue-shift is observed as the number of elements in the square-loop sub-arrays is reduced. Similar behavior has been observed and simulated for FSS and similar structures in prior literature, both at RF [80, 78, 81, 79] and in the optical regime [83, 84, 92, 93, 86, 87, 85], although infrared FSS have not been previously investigated in the manner shown here.

To assist in understanding the phenomena causing the shift in resonant wavelength for the square-loop FSS presented here, Figure 33 shows the peak resonant wavelength discretized over each unit cell. The figure was generated by integrating the volume loss density within the ground plane, dielectric spacer, and loop within each cell and recording the peak wavelength of absorptivity observed in the simulated spectra. Just as before, the structures are simulated with

s-polarized light (the electric field vector is horizontal with respect to the page) at an angle of 60 degrees off-normal. As can be seen in the figure, the overall average local absorptivity shifts gradually from longer to shorter wavelengths upon truncation, although the behavior is seen to be quite complex, due to the influences of truncation in both the horizontal and vertical dimensions. The fluctuations in the horizontal direction are due to coupling of the elements along the direction of polarization, while the fluctuations in the vertical direction are due to the 60 degree angle of incidence along with coupling of the elements in the direction opposite the polarization.

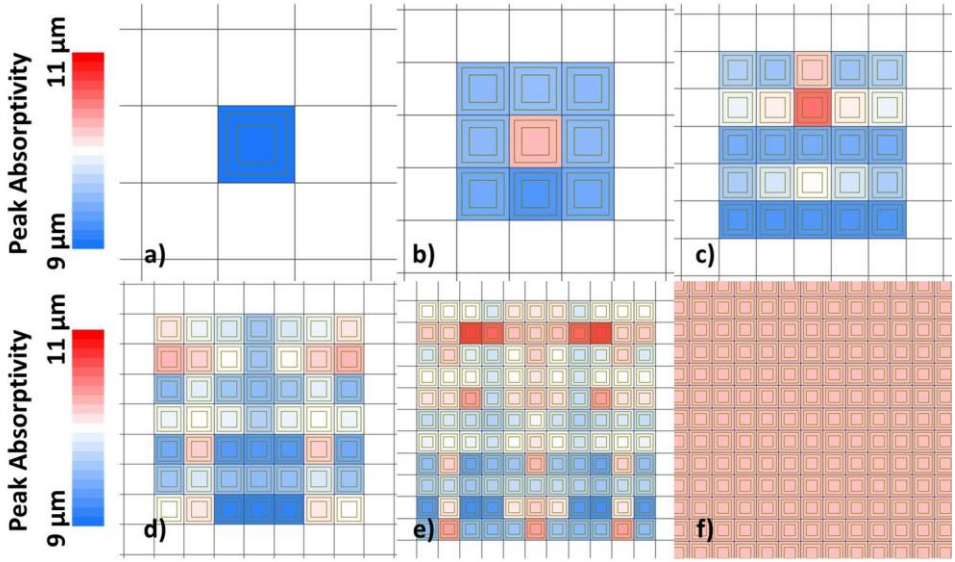

Figure 33. Spatially resolved spectral simulations showing the peak absorptivity for the full and truncated arrays: the isolated loops (a), 3×3 arrays (b), 5×5 arrays (c), 7×7 arrays (d), 11×11 arrays (e), and the full array (f).

The shift in overall resonant wavelength upon array truncation is due to a lack of nearest- and second-nearest-neighbor interactions at the edges of the array, although Figure 33 implies even more complicated interactions, caused by truncation in the vertical direction and further complicated by the 60 degree angle of incidence. It is expected that the edge elements will be

resonant at shorter wavelengths than the infinite design, as they converge toward the optical response of a single isolated square loop. This anticipated behavior is indeed observed for the 1×1, 3×3, 5×5, and infinite array since these show a longer wavelength of peak absorptivity within the array and a shorter wavelength of peak absorptivity at the edges. The detailed structure of the spatial absorptivity variations for the 7×7 and 11×11 arrays is interesting, although certain rows do show the expected spectral effect. It is noted that Figure 33 might be somewhat misleading, since the strength of absorptivity also varies from cell to cell, and this variation is not depicted graphically in the figure. The spatial fluctuation in resonant amplitude at 10.25 μm, which is correlated to the strength of absorptivity, can be observed in the near-field amplitude Figures 29 and 30.

The results depicting truncation effects in the near-field have shown that the quasi-infinite array has a uniform local electric field distribution in terms of amplitude and phase, while the truncated arrays have a disrupted local electric field. In all cases, the simulations and experiment bear a qualitative agreement, although the experimental results appear in many cases to show that the effects of truncation at the edges of the arrays are more significant than the simulations predict.

It is briefly noted here that the truncation effects discussed here are only directly comparable to the FSS design that was fabricated, although it is believed that the overall behavior observed would apply to any infrared FSS which is designed on a square grid with strong coupling between nearest neighbors. The results shown here are significant because they represent the first comprehensive investigation of array truncation effects in two-dimensional infrared FSS arrays, and could be used as a baseline comparison for future work where array truncation effects are a concern.

CHAPTER SIX: TUNING THE PEAK RESONANCE IN TRUNCATED INFRARED FREQUENCY SELECTIVE SURFACES

Chapter Five presented research involving the effects of array truncation on a square-loop infrared FSS design. In the far-field, the effects of truncation were observed as a blue-shifting of the peak wavelength of resonance as the number of elements in the truncated arrays was reduced. Building on the results from the previous chapter, this chapter presents designs for truncated arrays that attempt to tune the resonant wavelength back to that of the full array. Here, the design from the previous chapter and the corresponding 7×7 truncated array are used as a baseline and several design modifications are considered in an attempt to tune the center wavelength of resonant absorptivity.

A sample was patterned with the infinite array design, 7×7 sub-arrays of the infinite design, and two areas of 7×7 arrays which were geometrically altered to tune the peak wavelength of resonance. One of the altered 7×7 arrays had perimeter loops with a slightly increased size, while the other altered 7×7 array had a graded loop size increase from the center of the array to the perimeter. In the far-field, the altered finite array geometries were observed to have a tuned center resonance near the wavelength of the full array

6.1 Design Considerations and Sample Fabrication

Since the results reported in Chapter Five presented the consequences of array truncation and the lithographic exposure had been worked out to reduce proximity effects through dosing

and line width biasing, the baseline FSS design used here is identical to that which was presented in the last chapter. To summarize briefly, the Au square-loop elements were 1.44 μm per side, with 0.25 μm line width and a 1.79 μm periodicity. These were pattered via electron-beam lithography and liftoff on a 320 nm layer of ZnS with a 150 nm Cr ground plane. Fabrication of the full array and truncated 7×7 array sections of the sample was repeated for this experiment so that they would experience the same process variations as the rest of the patterns. The 7×7 array was chosen because it was observed to have a noticeable spectral shift in resonant wavelength due to truncation of approximately 0.3 μm, while still maintaining strong resonance which could be measured both in the near- and far-field.

Since a wide range of approaches to spectral tuning of the truncated arrays could be taken in the design stage, some common sense constraints were imposed. First, it was assumed that the tuning mechanism should be accomplished during the same step as the lithographic patterning, implying that only the x and y geometry of the elements could be altered, leaving their thickness and material properties unchanged. (It has been put forth that certain effects of truncation at RF can be altered by varying the impedance of some of the elements of the array [94]. For infrared FSS, this could be accomplished lithographically by using a different material for some of the elements. While interesting, such an approach is not taken here because of the increased complexity that would come along with the alignment of multiple layers). An additional restriction in the design stage was that the mechanism for tuning the resonant wavelength of the arrays should possess the same square symmetry as the truncated 7×7 arrays, which considers only changes in geometry that are applied evenly in the x and y direction. This is consistent with the requirements inherent in the potential application of FSS flakes that would be randomly oriented in practice.

Several design modifications were considered to reduce or eliminate the effects of array truncation on the center wavelength of spectral absorptivity. The designs that were simulated are as follows: the addition of a thin ring of Au around the truncated arrays, switching the perimeter elements to square patches with variable size, changing the perimeter elements to square loops of variable size, and altering the size of the square loops to vary gradually from the center element to the edges. Of these, the thin Au perimeter ring and changing the edge elements to square patches were found not to be of interest after initial simulations. The reasoning behind this decision was that the thin ring did not appear to have an effect on the far-field results at all and the square patches were observed in simulation to be too electrically large to shift the resonant frequency of the arrays while still fitting into the geometry.

The design modifications chosen for fabrication were the arrays with slightly larger perimeter loops and the arrays where the loops shift gradually in size from the center to the edge. The arrays where the dimensions of the loops was increased to bring the resonance back to longer wavelengths had geometries optimized in simulation which gave the truncated arrays a peak wavelength of 10.6 μm at 60 degrees off-normal, corresponding to the resonant frequency of the infinite FSS design. For the arrays with slightly larger edge loops, the loop edge length on the outside elements was increased by 50 nm. For the arrays in which the size of the loops increased gradually, the center loop was the same as the original design, the next ring of loops (closest to center) had a loop edge length increased by 12.5 nm, the ring of loops second in from the edge had a loop edge length increased by 25 nm, and the perimeter loops had a loop edge length which was increased by 37.5 nm.

The sample was fabricated using processes identical to that which was discussed in Chapter Five, in the form of 3 mm × 8 mm patterned sample areas. An additional dose matrix

was fabricated beforehand to fine-tune the dosing and line width bias in an attempt to fabricate the full array and truncated array loops with identical geometry as what was simulated. SEM micrographs of an unaltered 7×7 array and altered 7×7 arrays meant to tune the center wavelength of resonance are shown in Figure 34. Here, false color is applied to indicate changes in the geometry since these subtle differences are not distinguishable in monotone SEM micrographs. The top micrograph depicts an unaltered 7×7 array of the original design, where it is noted that the loops of the original size are shaded in blue. The center micrograph is that of a 7×7 array where the perimeter loops have been increased in edge length size by 50 nm; thus, the center loops are shaded in blue to reflect the original design and the perimeter loops are shaded in red to indicate the 50 nm increase in edge length. The bottom micrograph shows the 7×7 array where a gradient increase in edge length is applied from the center to the perimeter. Here, the center loop is shaded in blue to indicate the original design, the loops surrounding the center element are shaded in light blue to indicate that their edge length has increased by 12.5 nm, the next ring of loops (2^{nd} from perimeter ring) is shaded in green to represent a 25 nm increase in loop edge length, and the perimeter loops are shaded in orange, reflecting an increase in loop edge length of 37.5 nm. As was the case in Chapter Five, the truncated arrays were fabricated with 6.35 μm between adjacent loops in both directions.

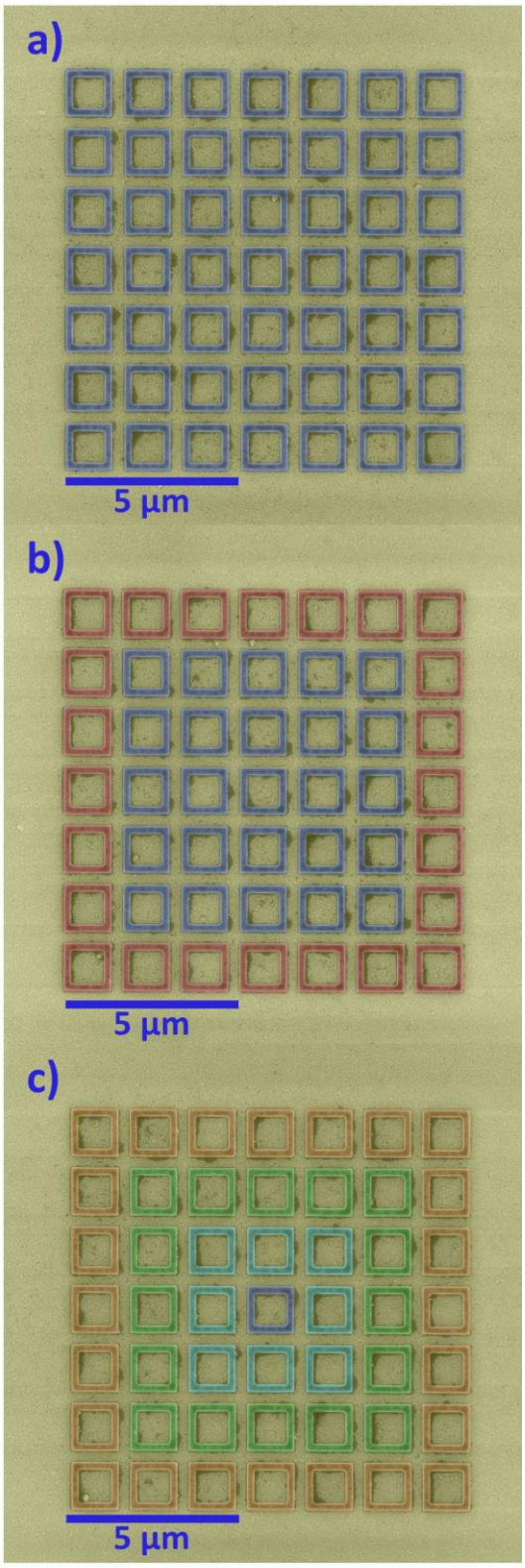

Figure 34. False color SEM micrographs of a) a 7×7 array of the original FSS design, b) a 7×7 array with an additional 50 nm added to the length of the perimeter loops, and c) a 7×7 array with a graded change in loop length from the center loop (original design) to the perimeter loops (37.5 nm added to the perimeter loop length).

It is noted that just as was the case for the structures fabricated in Chapter Five, the infrared FSS depicted in this chapter have square-loop edge lengths slightly smaller and more curved than the design dimensions. This was seen during careful analysis of the SEM micrographs and also observed in the far-field spectral reflectivity as a shift toward shorter wavelengths, consistent with the square-loop resonant condition that varies with loop perimeter. The discrepancies between the design and fabricated geometry highlight the need for fabricating the control samples (the infinite array and the unaltered 7×7 array) all on the same sample as was carried out in this experiment.

6.2 Tuning of Resonant Wavelength in Truncated Arrays

The 7x7 designs shown in Figure 34 were characterized using the HDR apparatus discussed previously. Figure 35 depicts the experimental SDR and simulated reflectivity (both s-polarized) at 60 degrees from normal incidence for the infinite array, the unaltered 7×7 array, and the two 7×7 array designs which were altered to shift the center wavelength of resonance. The dips in the SDR correspond to peaks in the absorptive resonance which was observed in the truncation effects investigation. As can be seen in the experimental results, the peak resonance of the infinite array appears at approximately 10.02 μm, while the unaltered 7×7 arrays have a center resonance at 9.64 μm. This finding is consistent with the observations in the previous chapter. The SDR of the truncated arrays which were altered to shift the resonant wavelength back to that of the original design shows that both geometrical modifications were effective: the arrays with slightly larger perimeter loops have a center resonance of 9.97 μm, while the arrays with a graded size increase have a center resonance of 9.93 μm. The decrease in strength of resonance seen between both the full array and the 7×7 arrays is attributed to the lack of square-

loop elements filling the measurement area due to the spacing between truncated arrays. The 7×7 arrays which were altered show a small increase in strength of resonance over that of the unaltered 7×7 arrays, in both theory and experiment.

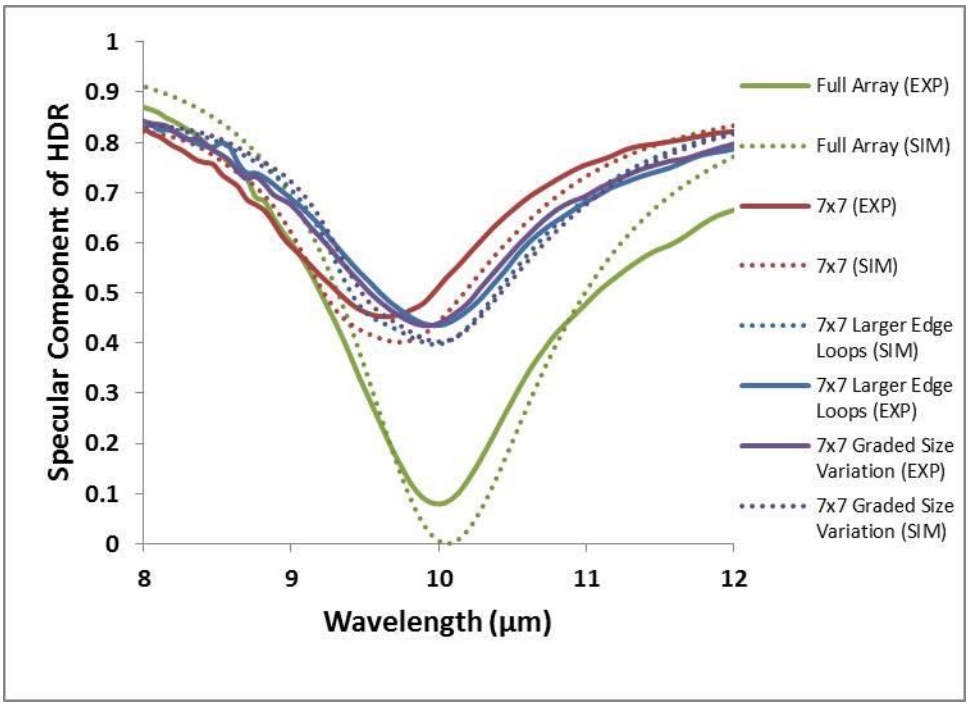

Figure 35. Experimental and simulated specular component of the HDR, taken at 60 degrees off-normal angle of incidence, for the full FSS array, unaltered 7×7 arrays, 7×7 arrays with larger perimeter loops, and 7×7 arrays with a graded loop size increase from the center to the edge.

The simulated results in Figure 35 compare well with the experiment, although the center wavelength of resonance is consistently simulated at slightly longer wavelengths and the amplitude of absorptivity is consistently greater in the simulations. The simulated reflectivity is taken as unity minus the simulated absorptivity due to the opaque ground plane. The infinite array and unaltered 7×7 arrays are simulated to be resonant at 10.06 μm and 9.74 μm, respectively. The finite arrays with larger perimeter loops are simulated to be resonant at 9.98 μm, while the finite arrays with a graded loop size variation are simulated to be resonant at

10.00 μm. As stated before, the fabricated loops were observed by SEM to be smaller than the design geometry. This discrepancy as well as a slight variation in the optical properties of the deposited Au led to a blue-shifting of the resonant wavelength of the infinite design. The simulated values shown in Figure 35 have included the smaller geometry as well as the optical constants derived from ellipsometry on a witness sample placed near the sample at the time of the Au metallization.

As was stated in Chapter Two, the HDR tool uses a 2π hemi-ellipsoidal reflector along with a moveable OAP reflector and a specular beam blocker to measure the HDR, DDR, and SDR. The reflected specular and diffuse components sum to equal the HDR and the solid angle of the specular and diffuse components sum to 2π steradians. The apparatus measures the HDR and DDR directly, and then computes the SDR as the difference between the two. The advantage of this approach over that which was shown in Chapter Five is that the HDR instrument is able to distinguish between the specular and diffuse components of the reflectivity.

Figure 36 shows the s-polarized HDR, DDR, and SDR as measured at 60 degrees off-normal corresponding to the samples with measured SDR shown in Figure 35. For the full array, it is observed that there is essentially no diffuse component of the HDR, such that the SDR and HDR are approximately equal. This is the expected result for an FSS array consisting of elements with sub-wavelength periodicity. In the case of the 7×7 arrays, a small but finite portion of the HDR is due to the diffuse component. The unaltered 7×7 arrays show a peak in the diffuse component of 0.073 at 9.75 μm, the 7×7 arrays with larger perimeter loops show a peak in the diffuse component of 0.063 at 9.90 μm, and the 7×7 arrays with a graded variation in size show a peak in the diffuse component of 0.071 at 9.90 μm, although these slight differences are difficult to compare near the noise level of the DDR measurement. Since the full array infrared FSS

shows no DDR at these wavelengths, the cause of the diffuse reflectance for the truncated arrays must be attributed to diffraction. However, it is unclear whether of the diffraction stems from the effects of array truncation or merely because the truncated arrays are placed periodically on the sample. At any rate, since the diffraction is observed here to be small, its effects on this experiment (as well as the experiments discussed in Chapter Five) are assumed to be small as well.

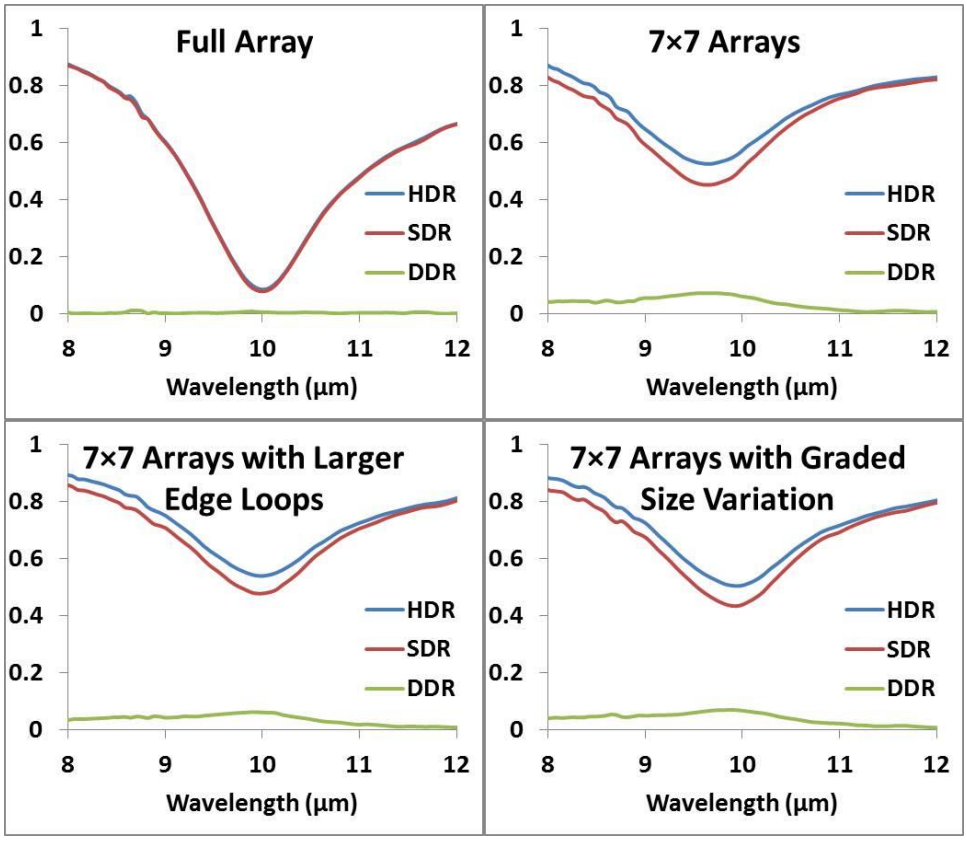

Figure 36. Experimental data sets showing the HDR, SDR, and DDR at 60 degrees off-normal angle of incidence for the full FSS array, unaltered 7×7 arrays, 7×7 arrays with larger perimeter loops, and 7×7 arrays with a graded loop size increase from the center to the edge.

6.3 Discussion

The reflectivity spectra presented earlier in this chapter showed that the peak resonant wavelength of the 7×7 truncated square-loop FSS arrays is blue-shifted from that of the infinite array design, and can be tuned to resonate near the center wavelength of the infinite array by making slight geometrical modifications. In two different examples, certain groups of square loops were made larger in the 7×7 arrays to alter the spectral response, relying on the proportional dependence of the square-loop wavelength of resonance with respect to the loop perimeter.

Experimentally, the SDR of the geometrically altered truncated arrays was observed to lead to tuning of the wavelength of resonance near that of the quasi-infinite array measurement, which was 10.02 μm. The arrays with slightly larger perimeter loops had an experimental resonant wavelength within 0.05 μm of the full array, while the arrays with a graded loop size increase from the center to the edge had a resonant wavelength within 0.09 μm of the full array. The results shown here imply that if exact tuning to the full array resonant wavelength were required, this could be accomplished by additional nm-scale corrections in the geometry of the truncated designs.

Aside from the two examples shown here, it is noted that many other approaches likely exist that would tune the center wavelength of resonance in truncated arrays. While the several possible methods for changing the resonant wavelength were simulated and discussed earlier in this chapter, there are certainly more exotic methods of obtaining similar results to those presented here. Alternatively, a very simple technique to tuning the resonant wavelength of truncated arrays could also be employed: given the somewhat quantitative predictive capability which has been shown in the spectral simulations of truncated arrays, one could merely start with

an infinite design resonant at a slightly longer wavelength than required for the application to offset the effects of truncation.

The diffuse component of the HDR was also measured for the patterned areas described in this chapter. The baseline full array FSS displayed a DDR of approximately zero, while the truncated arrays showed a DDR near 0.05. The DDR measurements are noteworthy, as they imply diffraction either due to array truncation of because the finite arrays are arranged periodically to construct a large-patterned area for the far-field measurements. (As verified by the lack of DDR observed for the full array FSS, the diffraction is not caused by the unit cell square-loops because they are sufficiently sub-wavelength). Although the main cause of the diffraction cannot be determined in this experiment, it is clear from the low DDR values that diffraction has not had a significant effect on the spectral shifting effects of truncation.

CHAPTER SEVEN: INFRARED FREQUENCY SELECTIVE SURFACE FLAKES REPRODUCIBLE BY OPTICAL LITHOGRAPHY

In Chapter Three, an etching procedure was introduced whereby a fully fabricated infrared FSS array could be transformed into releasable particles via wet and dry etching. These particles could be placed into a binder to create a large area conformal coating with engineered spectral properties at infrared frequencies. While the proposed process was shown to be feasible, the direct write electron-beam lithography used to pattern the FSS elements is prohibitively slow and therefore expensive. As an extension of this work, this chapter presents an infrared FSS fabricated with feature sizes that may be replicated on a commercially available optical-projection lithography tool, a parallel process that is much faster and cheaper than electron-beam lithography [95].

The FSS flakes shown in this chapter were fabricated by electron-beam lithography using a design suitable for optical-projection lithography. The design consisted of Au square patches immersed in BCB upon a Cr ground plane. As was shown in Chapter Three, the spectral reflectivity of the fabricated miniature arrays compared favorably with that of the undivided array as well as electromagnetic simulations, when the fill factor of the FSS particles in the measurement area is taken under consideration. As a final proof of feasibility, a full array of the square-patch design was fabricated using a 5× g-line (λ=436 nm) optical-projection lithography instrument, which yielded results comparable to that which was fabricated by electron-beam lithography.

7.1 Design and Fabrication

The goal of this design was to create a resonant FSS structure with dimensions reproducible with a commercially available optical-projection lithography tool. In particular, the g-line stepper was considered; these typically have a spatial resolution near 0.75 μm [53]. Line widths for standard infrared FSS structures such as crosses and loops are normally less than 0.5 μm; thus, only the solid plate-type elements were considered. The chosen design was a Au square-patch array encased in BCB with a Cr ground plane. A design of this type resonates strongly when electromagnetic modes are set up in the dielectric layer between the conductive patches and the ground plane; the resonant wavelength scales proportionally with the width of the patch. Simulations were carried out in HFSS, using the Floquet port method. The 150 nm Cr ground plane is considered to be optically thick such that the simulations need only to account for the top half of the structure. The geometrical dimensions of the FSS were parameterized in the simulation to give a strong resonance (low reflectivity) near 6.5 μm, which corresponded to a fundamental (dipolar) mode which was observed in the simulated local electric field. The final design had square-patch length and width equal to 1.28 μm, a Au patch thickness of 60 nm, a bottom BCB layer thickness of 0.22 μm, and an upper BCB layer thickness of 0.18 μm. The periodicity of the design was 2.07 μm such that the critical dimension was 0.79 μm, represented by the spacing between adjacent patches.

Fabrication of the releasable FSS particles has been described thoroughly in Chapter Three and will therefore be only briefly revisited here. The substrates consisted of Si wafers coated with 150 nm SiO_2 deposited by electron-beam evaporation. The patterns were symmetric about the 150 nm Cr ground plane that was also deposited via electron-beam evaporation. Each side contained the square-patch elements with layers of BCB both below and above. The square patches were fabricated by electron-beam lithography using ZEP 520A-7 as resist, metallization

of Au by electron-beam evaporation, and liftoff in N,N-dimethylacetamide. An etch mask of 150 nm SiO_2 and 75 nm Al (patterned by electron-beam lithography and liftoff) was placed over the entire structure to define the size and shape of the particles throughout the etching process. A schematic of a single FSS flake before etching in shown in Figure 37.

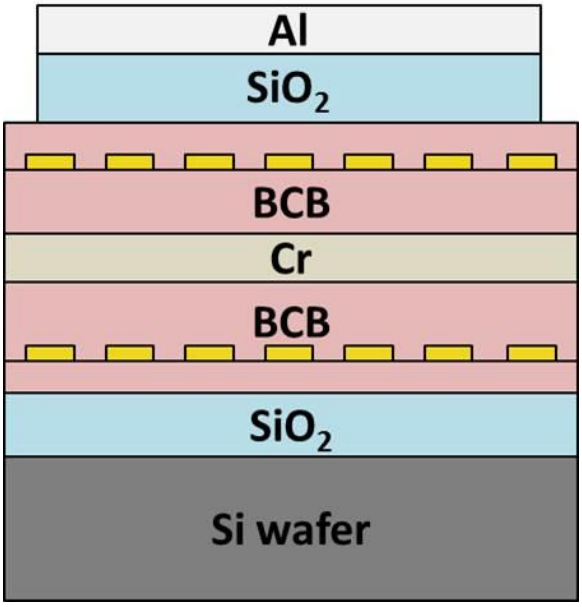

Figure 37. Schematic of a single square-patch flake before etching.

The plasma etching process was improved over the previous result by the use of a much more anisotropic method operating in RIE mode (Advanced Oxide Etcher, Surface Technology Systems). This technique used a mixture of O_2 and SF_6 that was 17:8, respectively. Al was found to etch slower than SiO_2 by this process, such that most of the SiO_2 remained after the BCB and Cr layers had been etched. As before, the Cr was etched as an intermediate step in Chrome Etch (Ashland Specialty Chemical Company). The flakes were released from the substrate as the SiO_2 was dissolved in a BOE solution, and then drawn from the solution using a filtered syringe. The

syringe was pressed upon a clean Si wafer, transferring most of the FSS particles for further characterization.

7.2 Square-Patch Flakes

An SEM image of a small collection of square-patch flakes is shown in Figure 38. This image was taken using a secondary electron detector to minimize the effects of charging. The figure shows that the particles display an improved degree of cleanliness in fabrication as compared to what has been previously shown in Figures 12, 13, 15, and 16. This improvement can be directly attributed to the improvements in the plasma etching process, both in terms of the straight flake edges as well as the fact that stray elements have been removed in the procedure.

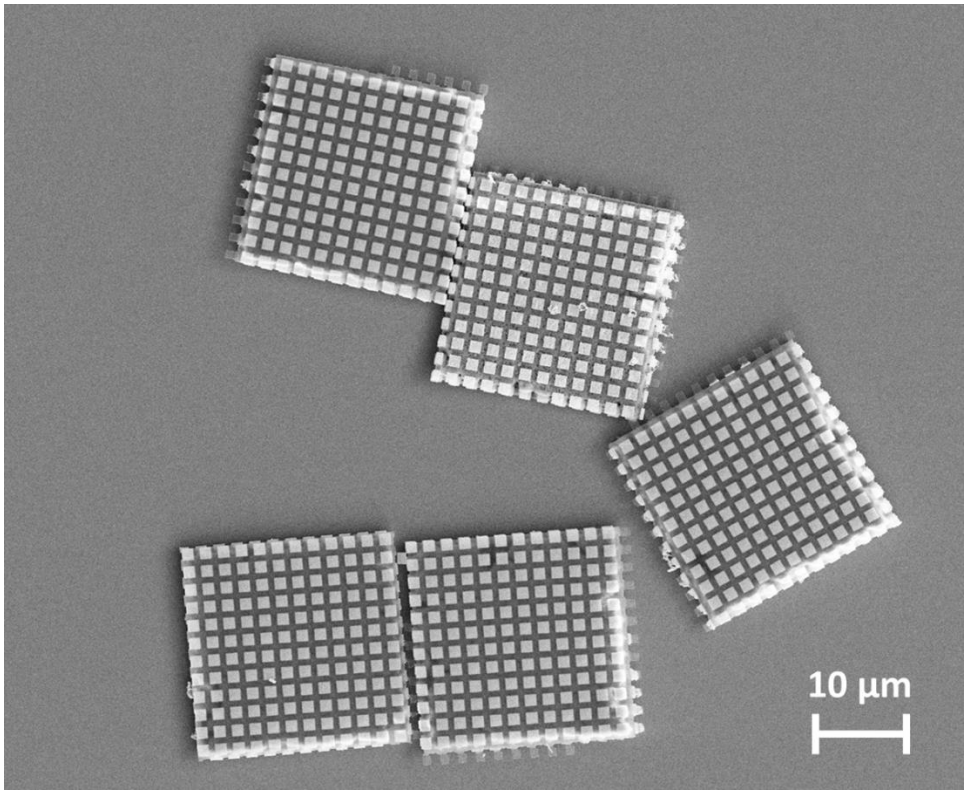

Figure 38. SEM micrograph of fabricated square-patch FSS particles.

The flakes as well as the full array FSS were characterized spectrally using the FTIR with 100 μm sample area microscope attachment that was described previously. Due to the collection method, the measurement of the areas containing the FSS particles is a mixture of the response of the particles as well as the Si wafer background. In an attempt to obtain the fill factor using the experimental data, the reflectivity of the full array and the Si wafer without flakes was measured. The expected reflectivity of the flake measurement can be approximated as a linear combination as follows.

$$\rho_{particles} = f \cdot \rho_{FSS} + (1 - f) \cdot \rho_{Si} \quad (54)$$

Here, the expected spectral reflectivity of the FSS particle measurement is $\rho_{particles}$, the measured spectral reflectivity of the full FSS array is ρ_{FSS}, the measured spectral reflectivity of the Si collection wafer is ρ_{Si}, and the proportion of particles in the measurement area, the fill factor, is given as *f*.

Figure 39 (top) shows the measured and simulated spectral reflectivity of the full array square-patch FSS, while the bottom shows the measurement of the FSS flakes as well as the best fit of the fill factor to Equation 54. For the full array, the theory and experiment are found to be in good agreement, with the dominant feature being the resonant absorptivity dip near 6.4 μm. The measurement of the flakes shows a dip in reflectivity near 6.2 μm which is shifted slightly toward shorter wavelengths when compared to that of the full array; this is consistent with the truncation effects results presented and discussed in Chapter Five. The best fit of the measured data to Equation 54 (yielding a fill factor of 0.22 by minimizing the summed mean squared

difference) shows a good qualitative match with the measurement of the FSS flakes, aside from the shift in resonant wavelength caused by array truncation. The small dips near 8 and 9.5 μm seen in all data sets are due to absorption features in the BCB layers [50, 74].

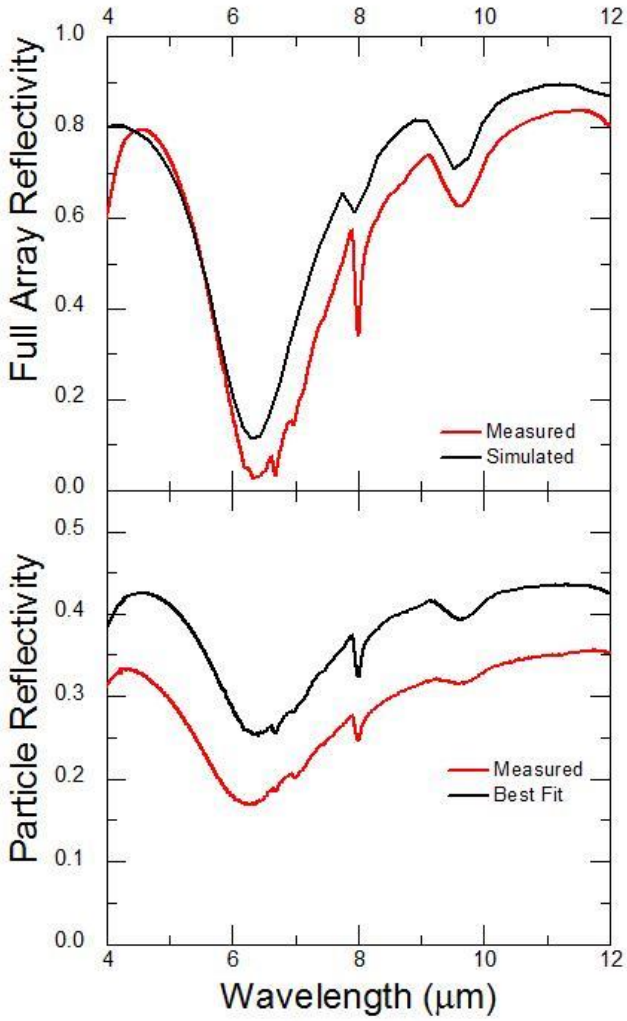

Figure 39. Spectral reflectivity of the square-patch FSS flakes versus the full array. Measured reflectivity of the full array (red) and simulated reflectivity of the full array (black) are plotted in the top graph, while the measured reflectivity of the FSS flakes (red) and the best fit of Equation 54 to the measured full array and Si background data (black) are plotted in the bottom graph.

The measurement of the FSS particles shown in Figure 39 is consistently less reflective than the best fit to Equation 54 by an amount averaging 9.1%. This difference is thought to arise mostly due to the fabrication process, which adds some surface roughness to the surface of the fabricated flakes as well as contamination of the open areas of the Si wafers between the FSS flakes. As an example depicting surface roughness is presented in Figure 40, a close-up SEM micrograph of a portion of a square-patch FSS flake. Here, porosity is observed as a result of the BOE etching process that releases the FSS particles from the substrate.

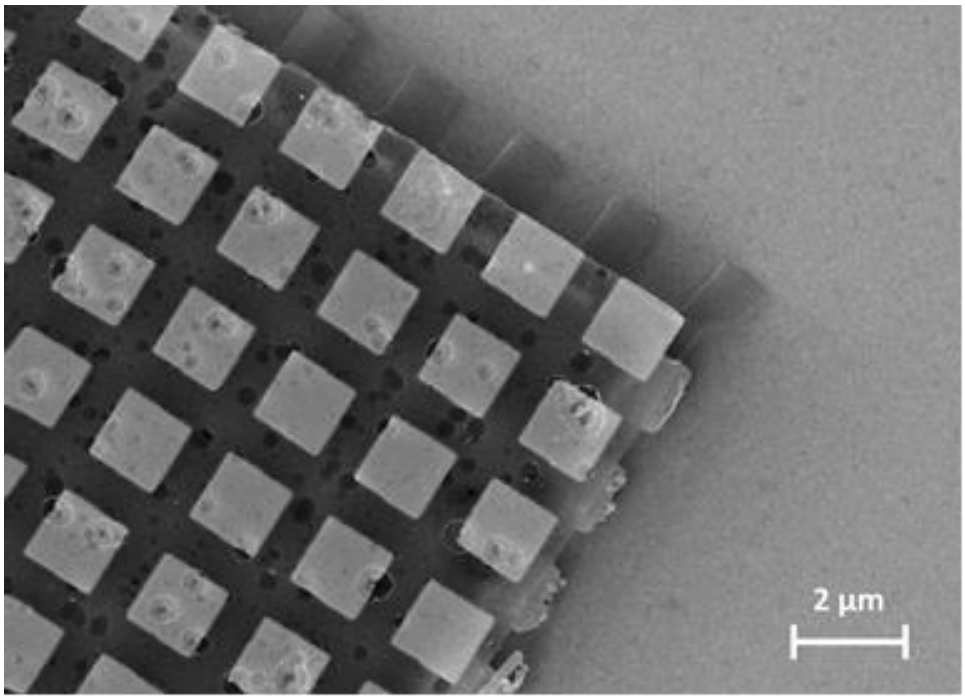

Figure 40. SEM micrograph of the corner of a square-patch FSS flake, showing porosity in the BCB surface layer.

7.3 Fabrication of Square-Patch Full Array by Optical-Projection Lithography

To experimentally demonstrate the achievability of fabrication of the structures presented in this chapter by optical lithography, a g-line 5× reduction optical stepper (GCA 6300C DSW

Wafer Stepper) was used to produce the full array square-patch infrared FSS. First, the CAD file that was used for electron-beam lithography was magnified 5× to create a binary reticle for the stepper tool (Photo Sciences, Inc.). For the photoresist, a 540 nm layer of S1805 was used. The substrate Cr and BCB as well as the BCB overcoat after metallization and liftoff were fabricated using the same process as was used for the full array fabricated by electron-beam lithography, which was described earlier in this chapter. Figure 41 is an SEM micrograph showing the results of the FSS array created by photolithography (left) as well as that which was created by electron-beam lithography (right). As can be seen in the figure, the patches fabricated by optical-projection lithography show rounded corners while those fabricated by electron-beam lithography have corners that are relatively square. This behavior was expected since the patch array design geometry has features quite close to the resolution limit of the g-line stepper tool. Aside from the noticeable curvature of the patches fabricated by optical-projection lithography, the horizontal and vertical dimensions of the patches as well as the spacing between them is found to be quite consistent for both plots shown in the figure.

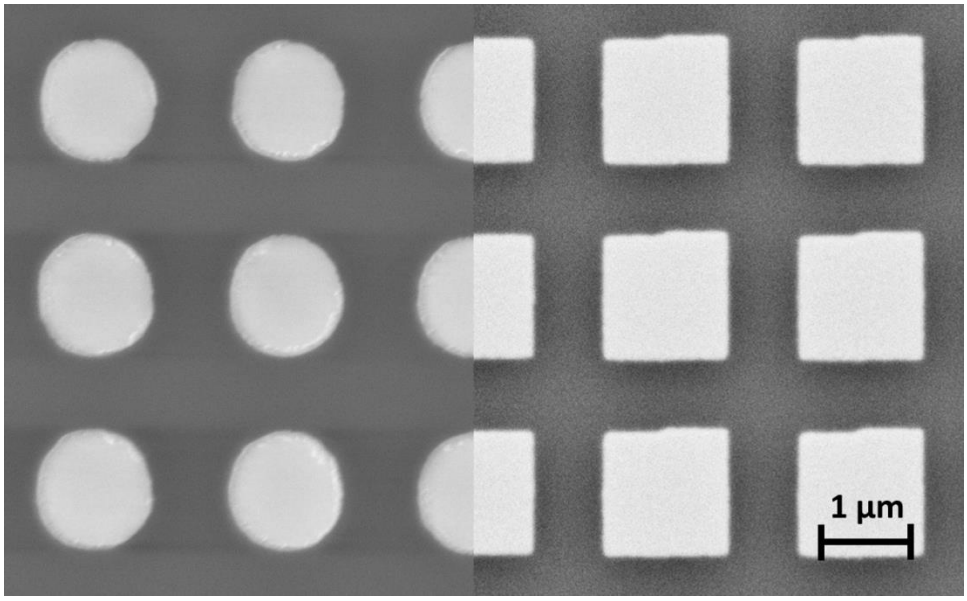

Figure 41. SEM micrograph comparison of the square-patch infrared FSS full array fabricated by g-line optical-projection lithography (left) as well as electron-beam lithography (right).

In Figure 42, a spectral comparison between the two fabrication methods is made, where the red line refers to the experimental reflectivity of the full array fabricated by electron-beam lithography (before etching it into flakes), the green line refers to the experimental reflectivity of the full array fabricated using the g-line stepper, and the black dotted line indicates the simulation of the stepper sample. The experimental reflectivity plots shown in the figure were measured using the FTIR apparatus with the microscope attachment described previously. The simulation of the curved surfaces was performed by altering the original simulation with the addition a 0.4 μm radius of curvature to each corner, which made the patches almost circular. Here, it is seen that the curved corners on the square patches affect the spectral response by shortening the resonant wavelength and reducing the amplitude of the absorptivity. Since the resonant condition of a square-patch FSS varies according to the edge length, adding curvature reduces the effective size of the patches and thus shortens the wavelength of resonance. Since the

peak of the resonant condition is optimized for a particular square-patch size, rounded corners increase the bandwidth of resonance and reduce the strength of resonance accordingly.

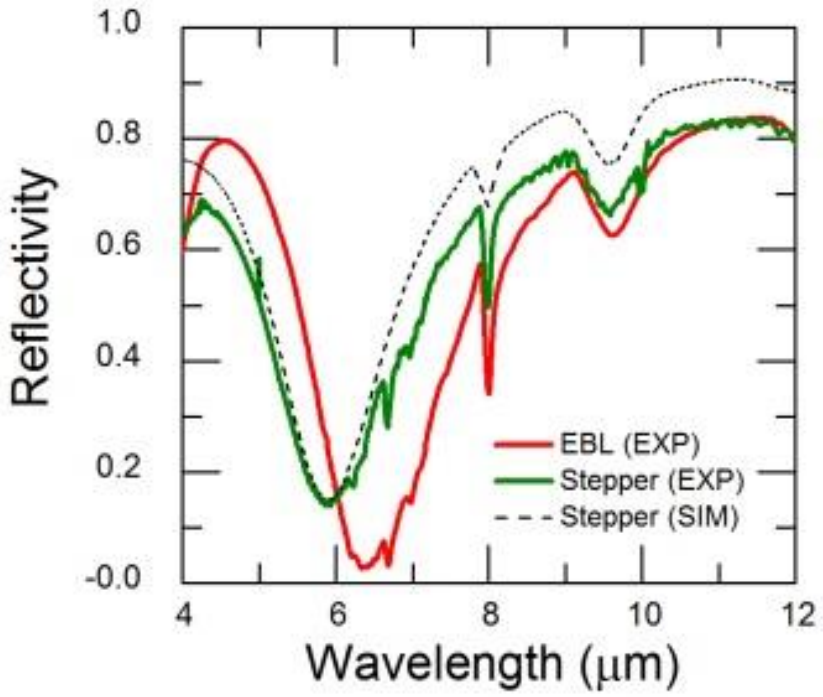

Figure 42. Experimental spectral reflectivity of the full array square-patch FSS fabricated by electron-beam lithography (red) compared to that of the full array fabricated by optical-projection lithography (green) as well as the simulated values which included a 0.4 μm radius of curvature on the corners to approximate observed curvature.

7.4 Discussion

The research presented in this chapter was concerned with the design, fabrication, and characterization of a square-patch infrared FSS with dimensions that could be produced using an optical lithography technique. The design was fabricated by electron-beam lithography, and used to create FSS particles by a process very similar to that which was shown in Chapter Three; the

only difference is that the plasma etching was greatly improved by implementation of an RIE process. As observed before, the spectral reflectivity of the FSS flakes compared well with that of the full array, when the proportion of flakes in the measurement area was taken into account. To further demonstrate the feasibility of the design for the purposes of optical lithography, fabrication of the full array was carried out using a g-line 5× reduction stepper tool. This produced a geometry with very rounded corners as opposed to the near-square geometry output by electron-beam lithography, with spectral properties blue-shifted slightly due to the roundness. While this work clearly showed that optical-projection lithography is a possible parallel approach for the formation of an FSS flake-based coating, it should be mentioned that the advantages afforded by this fabrication technique could be extended to other types of optical antenna-type structures as well. This is true especially considering that the design presented here was resonant near 6.5 μm; structures with resonance in the LWIR would be significantly larger and thus easier to fabricate. At slightly lower frequencies, even loop structures and waveguides could be fabricated with optical-projection lithography.

The square-patch array fabricated by photolithography demonstrates that the curvature induced by the limited resolution of optical-projection lithography merely shifts the resonance as compared to that of a more perfect square patch. If one were interested in fabricating patches that were squarer using the design presented here, there are possible options to achieve this. First, while several iterations of the fabrication occurred during the preparation of this dissertation, it is certainly possible that various combinations of resist thickness, exposure time, and depth of focus of the stepper could lead to a more square result. Additionally, somewhat improved resolution could be afforded by the use of an i-line (λ=365 nm) stepper simply due to the shortened exposure wavelength. Moreover, the reticle could be redesigned adding serifs to the

edges of each square-patch, a technique that is commonly used to create square corners when projection lithography is used for electronics [96]. As a final and important note, if a particular resonance was desired, simulations including the rounded edges could optimize the design by parametric iteration of the rest of the dimensions, such as the size of the patch, the periodicity, and the thickness of the dielectric layers.

CHAPTER EIGHT: CONCLUSION

8.1 Summary of Results

Due to rigid and relatively small substrates, the applicability of infrared FSS has been conventionally restricted to the implementation in optical systems or other applications smaller than the wafers upon which they are fabricated. As a method toward the creation of a large area conformal coating with customized spectral properties, a process in which infrared FSS arrays are fabricated bottom-up using electron-beam lithography and then selectively etched into small particles and released from the substrate was presented in Chapter Three, for both crossed-dipole and square-loop infrared FSS designs. The square-loop design contained a ground plane with the FSS fabricated symmetrically about either side to ensure that the final face up / face down orientation of the FSS particles did not affect the optical response.

In this dissertation, s-SNOM is used to spatially characterize the near-field of infrared FSS in terms of amplitude and phase of the electric field. Since this had not been carried out in the past on square-loop infrared FSS, Chapter Four presents initial measurements. Two separate designs are presented and fabricated on the same substrate. One of the designs has a loop edge length of 2.0 μm while the other has a loop edge length of 3.75 μm. Both are observed in simulations to have high absorptivity at 10.6 μm and 60 degrees off-normal incident angle (corresponding to the excitation scheme of the s-SNOM apparatus). The smaller loops display a dipolar near-field distribution at this wavelength while the larger loops display a quadrupolar distribution. The local field distributions were measured in terms of electric field amplitude and phase, with data qualitatively matching that which was simulated. The results were compared to

data taken in the far-field via FTIR, which showed evidence of the fundamental resonances involved in terms of peaks in spectral absorptivity.

The process of etching full infrared FSS arrays to create releasable FSS flakes inherently truncates the arrays, an issue which was addressed in Chapter Five. These truncation effects were studied both in the near- and far-field experimentally by designing a sample with a quasi-infinite array as well as various sized truncated arrays all on the same substrate. This square-loop FSS design used ZnS as the dielectric standoff layer to avoid the complicated situation of material absorption bands near the design wavelength. In the far-field, the effects of truncation were observed to shift the peak absorptivity toward shorter wavelengths, due to the decrease in local coupling of the edge elements as the array dimensionality is decreased. In the near-field, the effects of truncation were observed to disrupt the spatial uniformity of the local electric field amplitude and phase which was observed in the full array.

Building on the investigation of truncation effects presented in Chapter Five, infrared FSS designs were presented in Chapter Six which tuned the resonance of truncated arrays of 7×7 elements approximately back to the resonant wavelength of the infinite FSS design. This was accomplished in two different design modifications. The first altered only the size of the perimeter loops by a small amount and the second applied a graded size increase from the center loop to the perimeter loops. In both cases, these geometrical changes shifted the wavelength of resonance near that of the design wavelength of the full array, as was evidenced by control samples of unaltered 7×7 arrays as well as the infinite FSS design.

Since fabrication via electron-beam lithography is both slow and expensive relative to the needs for potential production of a large area FSS-based coating, Chapter Seven presented a square-patch design with dimensions that could be reproduced using optical-projection

lithography. Again, the spectral reflectivity of the FSS flakes was similar to that of the full array, when accounting for the proportion of flakes in the measurement area. While the square-patch array was fabricated using electron-beam lithography for the formation of releasable FSS particles, fabrication of the full array was successfully attempted using a g-line 5× reduction optical stepper tool. The results of fabrication via optical-projection lithography were comparable to that of electron-beam lithography, although the resonance was detuned slightly by the addition of rounded corners due to the reduced fabrication tolerance.

8.2 Future Work

The research discussed thus far has been focused on the feasibility of the FSS flake creation process, the characterization of flakes versus the full array, and the investigation of array truncation effects. At this point, the project may be advanced along several possible future directions. First, the angular dependence of the spectral response of the truncated arrays could be investigated using the HDR apparatus. Second, utilizing optical-projection lithography, the FSS particle production could be scaled up to create a much larger amount of flake material than has been fabricated by electron-beam lithography. Along these lines, characterization of larger areas of flake distributions could determine the optimum fill-factor. Lastly, more complex designs could be attempted, with an optical response geared toward potential applications.

The effects of array truncation on spectral absorptivity and near-field amplitude and phase were analyzed thoroughly in this dissertation; however, the effects of truncation on the angular response of the arrays remain uninvestigated at this time. The radiation pattern of the FSS designs will certainly vary as a function of the number of unit cell elements in each array, and this would likely have an impact on the performance of a large area coating consisting of

FSS flakes. To investigate these effects, one could fabricate a sample similar to that which was discussed in Chapter Five and measure this sample using the HDR apparatus, similar to that which was shown in Chapter Six for the 7×7 arrays. Two challenges currently stand in the way of this characterization being carried out. First, the patterned areas of the sample fabricated for the truncation effects experiment were cleaved into smaller sections for use in the s-SNOM tool and now have useable sample sizes smaller than the 2.5 mm interrogation beam of the HDR tool. Additionally, the characterization of interest would require angular discrimination of the diffuse components of reflectance. Currently, the tool only measures the integrated diffuse reflectance; however, it is believed that software modifications could allow the apparatus to measure diffuse scattering at arbitrary angles, which would allow for the desired measurement of the radiation pattern.

The results in the last chapter showed that certain infrared FSS designs could be easily fabricated using optical-projection lithography and subjected to wet and dry etching processes to generate FSS particles for use in large area coatings. The advantage of this fabrication technique is the significant reduction in time it takes for the lithographic patterning. Using this method, full 4” wafers of resonant patch FSS structures could be readily populated to create much larger amounts of the FSS flake material, which can be used to rigorously characterize the spectral dependence of the FSS flakes with respect to their angular and spatial distribution. Figures 15 and 16 showed that increasing the density of the FSS flakes will lead to an angular distribution of the flakes due to stacking effects. While an increased flake density should yield a spectral result closer to that of the infinite array, the effects of stacking on the angular distribution may lead to a diminished spectral result. It is possible that an optimized fill-factor of the FSS flakes exists or that the effects of flake stacking can be mitigated by additional processes. These issues would

much more easily be addressed using the generous amounts of FSS flake material afforded by a parallel lithography technique such as optical-projection lithography.

Likewise, the production of larger amounts of the FSS particles makes it possible to choose between possible candidate liquid binders. The patent [97] corresponding to published data presented in Chapter Three [48] additionally suggests that the FSS particles may be stored in a solvent which merely evaporates upon application. At any rate, substantial amounts of flake material would allow for thorough infrared spectral characterization of the effects of the binder or solvent as well as inspection of the effects of these liquids on the eventual distribution of the FSS flakes.

As an additional step forward, more complex infrared FSS designs could be explored for utilization in the FSS particles. For example, FSS flakes could be fabricated with the effects of truncation already factored in to the design, as implied by the work shown in Chapter Six. Also, more omnidirectional FSS designs could be implemented, which supports the goal of a large area, conformal coating. As an additional example, it has been shown that a stratified passive device containing an embedded linear polarizer, a thermal isolation layer, and a meanderline polarizer will emit circular polarization via thermal excitation [40]. Such an approach could be implemented for FSS flakes, although the additional layers would certainly enhance the difficulty of fabrication.

LIST OF REFERENCES

[1] R. Keiburtz and A. Ishimaru, "Scattering by a periodically apertured conducting screen," *IRE Transactions on Antennas and Propagation,* vol. 9, no. 6, pp. 506-514, 1961.

[2] C. C. Chen, "Transmission through a conducting screen perforated periodically with apertures," *IEEE Transactions on Microwave Theory and Techniques,* vol. 18, no. 9, pp. 627-632, 1970.

[3] B. Munk, R. J. Luebbers and R. Fulton, "Transmission through a two-layer array of loaded slots," *IEEE Transactions on Antennas and Propagation,* vol. 22, no. 6, pp. 804-809, 1974.

[4] C. C. Chen, "Scattering by a two-dimensional periodic array of conducting plates," *IEEE Transactions on Antennas and Propagation,* vol. 18, no. 5, pp. 660-665, 1970.

[5] R. H. Ott, R. G. Kouyoumijian and L. Peters, "Scattering by a two-dimensional periodic array of narrow plates," *Radio Science,* vol. 2, 1967.

[6] B. A. Munk, Frequency Selective Surfaces: Theory and Design, New York: Wiley and Sons, 2000.

[7] S. W. Lee, "Scattering by a dielectric-loaded screen," *IEEE Transactions on Antennas and Propagation,* vol. 19, no. 5, pp. 656-665, 1971.

[8] R. Pous and D. M. Pozar, "Frequency-selective surface using aperture-coupled microstrip patches," *Electronics Letters,* vol. 25, no. 17, pp. 1136-1138, 1989.

[9] A. Mitsuishi, Y. Otsuka, S. Fujita and H. Yoshinaga, "Metal mesh filters in the far infrared region," *Japanese Journal of Applied Physics*, vol. 2, no. 9, pp. 574-577, 1963.

[10] G. D. Holah and N. Morrison, "Narrow-bandpass interference filters for the far infrared," *Journal of the Optical Society of America*, vol. 67, no. 7, pp. 971-974, 1977.

[11] A. E. Costey, K. H. Hursey, G. F. Neill and J. M. Ward, "Free-standing fine-wire grids: their manufacture, performance, and use at millimeter and submillimeter wavelengths," *Journal of the Optical Society of America*, vol. 67, no. 7, pp. 979-981, 1977.

[12] G. R. Bird and M. Parrish, "The wire grid as a near-infrared polarizer," *Journal of the Optical Society of America*, vol. 50, no. 9, pp. 886-891, 1960.

[13] M. S. Durschlag and T. A. DeTemple, "Far-IR optical properties of freestanding and dielectrically backed metal meshes," *Applied Optics*, vol. 20, no. 7, pp. 1245-1253, 1981.

[14] R. Ulrich, T. J. Bridges and M. A. Pollack, "Variable metal mesh coupler for far infrared lasers," *Applied Optics*, vol. 9, no. 11, pp. 2511-2516, 1970.

[15] R. Ulrich, K. F. Renk and L. Genzel, "Tunable submillimeter interferometers of the Fabry-Perot type," *IEEE Transactions on Microwave Theory and Techniques*, vol. 11, no. 5, pp. 363-371, 1963.

[16] J. C. Vardaxoglou, "Frequency Selective Surfaces - Analysis and Design," Taunton, Sommerset, England, Research Studies Press Ltd., 1997.

[17] L. Huang, X. Chen, G. Muhlenbernd, G. Li, B. Bai, Q. Tan, G. Z. T. Jin and S. Zhang, "Dispersionless phase discontinuities for controlling light propagation," *Nano Letters*, vol. 12, no. 11, pp. 5750-5755, 2012.

[18] C. L. Holloway, E. F. Kuester, J. A. Gordon, J. O' Hara, J. Booth and D. R. Smith, "An overview on the theory and applications of metasurfaces: the two-dimensional equivalents of metamaterials," *Ant. Propagat. Mag.*, vol. 54, no. 2, pp. 10-35, 2012.

[19] Q. Feng, M. Pu, C. Hu and X. Luo, "Engineering the dispersion of metamaterial surface for broadband infrared absorption," *Optics Letters*, vol. 37, no. 11, pp. 2133-2135, 2012.

[20] C. Debus and P. H. Bolivar, "Frequency selective surfaces for high sensitivity terahertz sensing," *Applied Physics Letters*, vol. 91, p. 184102, 2007.

[21] D. J. Kern, D. H. Werner, M. J. Wilhelm and K. H. Church, "Genetically engineered multiband high-impedance frequency selective surfaces," *Microwave and Optical Technology Letters*, vol. 38, no. 5, pp. 400-403, 2003.

[22] F. Bayatpur and K. Sarabandi, "Tuning performance of metamaterial-based frequency selective surfaces," *IEEE Transactions on Antennas and Propagation*, vol. 57, no. 2, pp. 590-592, 2009.

[23] D. J. Shelton, K. R. Coffey and G. D. Boreman, "Experimental demonstration of tunable phase in a thermochromic infrared-reflectarray metamaterial," *Optics Express*, vol. 18, no. 2, pp. 1330-1335, 2010.

[24] X. Liu, T. Tyler, T. Starr, A. F. Starr, N. M. Jokerst and W. J. Padilla, "Taming the blackbody with infrared metamaterials as selective thermal emitters," *Physical Review Letters*, vol. 107, p. 045901, 2011.

[25] E. C. Kinzel, J. C. Ginn, R. L. Olmon, D. J. Shelton, B. A. Lail, I. Brener, M. B. Sinclair, M. B. Raschke and G. D. Boreman, "Phase resolved near-field mode imaging for the design on frequency-selective surfaces," *Optics Express*, vol. 20, no. 11, pp. 11986-11993, 2012.

[26] J. Ginn, D. Shelton, P. Krenz, B. Lail and G. Boreman, "Altering infrared metamaterial performance through metal resonance damping," *Journal of Applied Physics,* vol. 105, p. 074304, 2009.

[27] I. Puscasu, W. L. Schaich and G. D. Boreman, "Modeling parameters for the spectral behavior of infrared frequency-selective surfaces," *Applied Optics,* vol. 40, no. 1, pp. 118-124, 2001.

[28] W. L. Schaich, G. Schider, J. R. Krenn, A. Leitner, F. R. Aussenegg, I. Puscasu, B. Monacelli and G. Boreman, "Optical resonances in periodic surface arrays of metallic patches," *Applied Optics,* vol. 42, no. 28, pp. 5714-5721, 2003.

[29] I. Puscasu, D. Spencer and G. D. Boreman, "Refractive-index and element-spacing effects on the spectral behavior of infrared frequency-selective surfaces," *Applied Optics,* vol. 39, no. 10, pp. 1570-1574, 2000.

[30] I. Puscasu, W. Schaich and G. D. Boreman, "Resonant enhancement of emission and absorption using frequency selective surfaces in the infrared," *Infrared Physics & Technology,* vol. 43, no. 2, pp. 101-107, 2002.

[31] C. M. Rhoads, E. K. Damon and B. A. Munk, "Mid-infrared filters using conducting elements," *Applied Optics,* vol. 21, no. 15, pp. 2814-2816, 1982.

[32] D. M. Byrne, A. J. Brouns, F. C. Case, R. C. Tiberio, B. L. Whitehead and E. D. Wolf, "Infrared mesh filters fabricated by electron-beam lithography," *Journal of Vacuum Science and Technology B,* vol. 3, no. 1, pp. 268-271, 1985.

[33] K. D. Moller, O. Sternberg, H. Grebel and K. P. Stewart, "Inductive cross-shaped metal meshes and dielectrics," *Applied Optics,* vol. 41, no. 19, pp. 3919-3926, 2002.

[34] K. D. Moller, J. B. Warren, J. B. Heaney and C. Kotecki, "Cross-shaped bandpass filters for the near- and mid-infrared wavelength regions," *Applied Optics,* vol. 35, no. 31, pp. 6210-6215, 1996.

[35] B. Monacelli, J. B. Pryor, B. A. Munk, D. Kotter and G. D. Boreman, "Infrared frequency selective surface based on circuit-analog square loop design," *IEEE Transactions on Antennas and Propagation,* vol. 53, no. 2, pp. 745-752, 2005.

[36] J. S. Tharp, B. A. Lail, B. A. Munk and G. D. Boreman, "Design and demonstration of an infrared meanderline phase retarder," *IEEE Transactions on Antennas and Propagation,* vol. 55, no. 11, pp. 2983-2988, 2007.

[37] J. S. Tharp, J. Alda and G. D. Boreman, "Off-axis behavior of an infrared meander-line waveplate," *Optics Letters,* vol. 32, no. 19, pp. 2852-2854, 2007.

[38] S. L. Wadsworth and G. D. Boreman, "Analysis of throughput for multilayer infrared meanderline waveplates," *Optics Express,* vol. 18, no. 13, pp. 13345-13360, 2010.

[39] J. Ginn, D. Shelton, P. Krenz, B. Lail and G. Boreman, "Polarized infrared emission using frequency selective surfaces," *Optics Express,* vol. 18, no. 5, pp. 4557-4563, 2010.

[40] S. L. Wadsworth, P. G. Clem, E. D. Branson and G. D. Boreman, "Broadband circularly-polarized infrared emission from multilayer metamaterials," *Optical Materials Express,* vol. 1, no. 3, pp. 466-479, 2011.

[41] J. E. Raynolds, B. A. Munk, J. B. Pryor and R. K. Marhekfa, "Ohmic loss in frequency-selective surfaces," *Journal of Applied Physics,* vol. 93, pp. 5346-5357, 2003.

[42] D. J. Shelton, J. S. Tharp, G. Zummo, W. R. Folks and G. D. Boreman, "Fabrication of periodic microstructures on flexible polyimide membranes," *Journal of Vacuum Science and Technology B,* vol. 25, no. 6, pp. 1827-1831, 2007.

[43] H. Tao, A. C. Strikwerda, K. Fan, C. M. Bingham, W. J. Padilla, X. Zhang and R. D. Averitt, "Terahertz metamaterials on free-standing highly-flexible polyimide substrates," *Journal of Physics D: Applied Physics,* vol. 41, no. 23, p. 232004, 2008.

[44] S. Gupta, G. Tuttle, M. Sigalas and K. M. Ho, "Infrared filters using metallic photonic band gap structures on flexible substrates," *Applied Physics Letters,* vol. 71, no. 17, pp. 2412-2414, 1997.

[45] N. R. Han, Z. C. Chen, C. S. Lim, B. Ng and M. H. Hong, "Broadband multi-layer terahertz metamaterials fabrication and characterization on flexible substrates," *Optics Express,* vol. 19, no. 8, pp. 6990-6998, 2011.

[46] R. Ortuno, C. Garcia-Meca and A. Martinez, "Terahertz metamaterials on flexible polypropylene substrate," *Plasmonics,* 2014.

[47] X. G. Peralta, M. C. Wanke, C. L. Arrington, J. D. Williams, I. Brener, A. Strikwerda, R. D. Averitt, W. J. Padilla, E. Smirnova, A. J. Taylor and J. F. O'Hara, "Large-area metamaterials on thin membranes for multilayer applications at terahertz and higher frequencies," *Applied Physics Letters,* vol. 94, p. 161113, 2009.

[48] J. A. D' Archangel, G. D. Boreman, M. B. Shelton, M. B. Sinclair and I. Brener, "Releasable infrared metamaterials," *Journal of Vacuum Science & Technology B,* vol. 29, no. 5, p. 0510806, 2011.

[49] M. A. Ordal, L. L. Long, R. J. Bell, S. E. Bell, R. R. Bell, R. W. Alexander and C. A. Ward, "Optical properties of the metals Al, Co, Cu, Au, Fe, Pb, Ni, Pd, Pt, Ag, Ti, and W in the infrared and far infrared," *Applied Optics*, vol. 22, no. 7, pp. 1099-1119, 1983.

[50] W. R. Folks, J. Ginn, D. Shelton, J. Tharp and G. Boreman, "Spectroscopic ellipsometry of materials for infrared micro-device fabrication," *Physica Status Solidi C*, vol. 5, no. 5, pp. 1113-1116, 2008.

[51] J. Ginn, B. Lail, D. Shelton, J. Tharp, W. Folks and G. Boreman, "Characterizing infrared frequency selective surfaces on dispersive media," *ACES*, vol. 22, no. 1, pp. 184-188, 2007.

[52] Ansys, Inc., "Introduction to Ansys HFSS 2014: 15.0 Release," 2014.

[53] S. A. Campbell, The Science and Engineering of Microelectronic Fabrication, Oxford University Press, 2001.

[54] C. Vieu, F. Carcenac, A. Pepin, Y. Chen, M. Mejias, A. Lebib, L. Manin-Ferlazzo, L. Couraud and H. Launois, "Electron beam lithography: resolution limits and applications," *Applied Surface Science*, vol. 164, no. 1, pp. 111-117, 2000.

[55] S. Y. Chou, P. R. Krauss and P. J. Renstrom, "Nanoimprint lithography," *Journal of Vacuum Science & Technology B*, vol. 14, p. 4129, 1996.

[56] The Dow Chemical Company, "Processing Procedures for CYCLOTENE 3000 Series Dry Etch Resins," April 2008. [Online]. Available: www.dow.com/cyclotene. [Accessed 05 April 2011].

[57] H. G. Tompkins, A User's Guide to Ellipsometry, San Diego: Academic Press, 1993.

[58] R. L. Olmon, P. M. Krenz, A. C. Jones, G. D. Boreman and M. B. Raschke, "Near-field imaging of optical antenna modes in the mid-infrared," *Optics Express,* vol. 16, no. 25, pp. 20295-20305, 2008.

[59] P. M. Krenz, R. L. Olmon, B. A. R. M. B. Lail and G. D. Boreman, "Near-field measurement of infrared coplanar strip transmission line attenuation and propagation constants," *Optics Express,* vol. 18, no. 21, pp. 21678-21686, 2010.

[60] R. L. Olmon, M. Rang, P. M. Krenz, B. A. Lail, L. V. Saraf, G. D. Boreman and M. B. Raschke, "Determination of electric-field, magnetic-field, and electric-current distributions of infrared optical antennas: a near-field optical vector network analyzer," *Physical Review Letters,* vol. 105, p. 167403, 2010.

[61] L. Novotny and B. Hecht, Principles of Nano-Optics, Cambridge: Cambridge University Press, 2006.

[62] B. Deutsch, R. Hillenbrand and L. Novotny, "Near-field amplitude and phase recovery using phase-shifting interferometry," *Optics Express,* vol. 16, no. 2, pp. 494-501, 2008.

[63] F. Keilmann and R. Hillenbrand, "Near-field microscopy by elastic light scattering from a tip," *Philosophical Transactions of the Royal Society A,* vol. 362, pp. 787-805, 2004.

[64] B. Schoelson, "Image Registation App," MathWorks, 09 Jan. 2012. [Online]. Available: http://www.mathworks.com/matlabcentral/fileexchange/34510-image-registration-app.

[65] J. H. Bruning, D. R. Herriott, J. E. Gallagher, D. P. Rosenfeld, A. D. White and D. J. Brangaccio, "Digital wavefront measuring interferometer for testing optical surfaces and lenses," *Applied Optics,* vol. 13, no. 11, pp. 2693-2703, 1974.

[66] R. Hillenbrand and F. Keilmann, "Complex optical constants on a subwavelength scale," *Physical Review Letters,* vol. 85, no. 14, p. 3029, 2000.

[67] N. Ocelic, A. Huber and R. Hillenbrand, "Pseudoheterodyne detection for background-free near-field spectroscopy," *Applied Physics Letters,* vol. 89, no. 10, p. 101124, 2006.

[68] P. B. Chinoy, "Reactive ion etching of benzocyclobutene polymer films," *IEEE Transactions on Components, Packaging, and Manufacturing Technology, Part C,* vol. 20, no. 3, pp. 199-206, 1997.

[69] S. M. Hu and D. R. Kerr, "Observation of etching of n-type silicon in aqueous HF solutions," *Journal of the Electrochemical Society,* vol. 114, no. 4, p. 414, 1967.

[70] T. M. Stokich, C. C. Fulks, M. T. Bernius, D. C. Burdeaux, P. E. Garrou and R. H. Heistand, "Planarization with Cyclotene 3022 (BCB) polymer coatings," *Materials Research Society Proceedings,* vol. 308, 1993.

[71] J. S. Tharp, D. J. Shelton, S. L. Wadsworth and G. D. Boreman, "Electron-beam lithography of multiple-layer submicrometer periodic arrays on a barium fluorida substrate," *Journal of Vaccum Science and Technology B,* vol. 26, no. 5, pp. 1821-1823, 2008.

[72] J. A. Bean, B. A. Slovick and G. D. Boreman, "Influence of substrate configuration on the angular response pattern of infrared antennas," *Optics Express,* vol. 18, no. 21, pp. 21705-21713, 2010.

[73] T. A. Mandviwala, B. A. Lail and G. D. Boreman, "Characterization of microstrip transmission lines at IR frequencies - modeling, fabrication, and measurements," *Microwave and Optical Technology Letters,* vol. 50, no. 5, pp. 1232-1237, 2008.

[74] J. T. Beechinor, E. McGlynn, M. O'Reilly and G. M. Crean, "Optical characterisation of thin film benzocyclobutene (BCB) based polymers," *Microelectronic Engineering*, vol. 33, pp. 363-368, 1997.

[75] H. Y. Yang, S. X. Gong, P. F. Zhang, F. T. Zha and J. Ling, "A novel miniaturized frequency selective surface with excellent center frequency stability," *Microwave and Optical Technology Letters*, vol. 51, no. 10, pp. 2513-2516, 2009.

[76] A. Janhsen and V. Hansen, "Arrays of finite or infinite extent in multilayered media for use as passive frequency-selective surfaces," *Microwaves, Antennas, and Propagation, IEE Proceedings H*, vol. 138, no. 1, pp. 1-8, 1991.

[77] J. A. D' Archangel, E. Tucker, E. Kinzel, E. A. Muller, H. A. Bechtel, M. C. Martin, M. B. Raschke and G. Boreman, "Near- and far-field spectroscopic imaging investigation of resonant square-loop infrared metasurfaces," *Optics Express*, vol. 21, no. 14, pp. 17150-17160, 2013.

[78] P. W. Grounds and K. J. Webb, "Numerical analysis of finite frequency selective surfaces," in *Antennas and Propagation Society International Symposium*, APS Digest, 1988, pp. 746-749.

[79] C. Guclu, J. Sloan, S. Pan and F. Capolina, "High impedance surface as an antenna without a dipole on top," in *2011 IEEE International Symposium on Antennas and Propagation*, 2011.

[80] G. I. Kiani, L. G. Olsson, A. Karlsson, K. P. Esselle and M. Nilsson, "Cross-dipole bandpass frequency selective surface for energy-saving glass used in buildings," *IEEE Transactions on Antennas and Propagation*, vol. 59, pp. 520-525, 2011.

[81] S. B. Savia, E. A. Parker and B. Phillips, "Finite planar- and curved-ring-element frequency-selective surfaces," *IEE Proceedings on Microwave Antennas and Propagation,* vol. 146, pp. 401-406, 1999.

[82] I. T. Ekpo, J. C. Batchelor and E. A. Parker, "Transmitted power distribution across a minimal size FSS for long wavelength operation," in *2010 Loughborough Antennas and Propagation Conference*, 2010.

[83] V. A. Fedotov, N. Papasimakis, E. Plum, A. Bitzer, M. Walther, P. Kuo, D. P. Tsai and N. I. Zheludev, "Spectral collapse in ensembles of metamolecules," *Physical Review Letters,* vol. 104, p. 223901, 2010.

[84] K. Bao, N. A. Mirin and P. Nordlander, "Fano resonances in planar silver nanosphere clusters," *Appl. Phys. A. Mater. Sci.,* vol. 100, pp. 333-339, 2010.

[85] S. A. Maier, P. G. Kik and H. A. Atwater, "Observation of coupled plasmon-polariton modes in Au nanoparticle chain waveguides of different lengths: estimation of waveguide loss," *Applied Physics Letters,* vol. 81, pp. 1714-1716, 2002.

[86] S. A. Maier, P. G. Kik and H. A. Atwater, "Optical pulse propagation in metal nanoparticle chain waveguides," *Physical Review B,* vol. 67, p. 205402, 2003.

[87] B. Willingham and S. Link, "Energy transport in metal nanoparticle chains via sub-radiant plasmon modes," *Optics Express,* vol. 19, pp. 6450-6461, 2011.

[88] J. D' Archangel, E. Tucker, M. B. Raschke and G. Boreman, "Array truncation effects in infrared frequency selective surfaces," *Optics Express,* vol. 22, no. 13, pp. 16645-16659, 2014.

[89] M. L. M. Balistreri, J. P. Korterik, L. Kuipers and N. F. van Hulst, "Local observations of phase singularities in optical fields in waveguede structures," *Physical Review Letters*, vol. 85, pp. 294-297, 2000.

[90] M. L. M. Balistreri, J. P. Korterik, L. Kuipers and N. F. van Hulst, "Phase mapping of optical fields in integrated optical waveguide structures," *Journal of Lightwave Technology*, vol. 19, pp. 1169-1176, 2001.

[91] J. N. Walford, K. A. Nugent, A. Roberts and R. E. Scholten, "High-resolution phase imaging of phase singularities in the focal region of a lens," *Optics Letters*, vol. 27, pp. 345-347, 2002.

[92] J. B. Lassiter, H. Sobhani, M. W. Knight, W. S. Meilczarek, P. Nordlander and N. J. Halas, "Designing and deconstructing the fano lineshape in plasmonic metamolecules," *Nano Letters*, vol. 12, pp. 1058-1062, 2011.

[93] J. Ye, F. Wen, H. Sobhani, J. B. Lassiter, P. V. Dorpe, P. Nordlander and N. J. Halas, "Plasmonic nanoclusters: near field properties of the fano resonance nterrogated with SERS," *Nano Letters*, vol. 12, pp. 1660-1667, 2012.

[94] B. A. Munk, Finite Antenna Arrays and FSS, Wiley-Interscience, 2003.

[95] J. A. D' Archangel, D. J. Shelton, R. Hudgins, M. K. Poutous and G. D. Boreman, "Large area infrared frequency selective surface with dimensions reproducible by optical lithography," *Journal of Vacuum Science and Technology B*, vol. 32, no. 5, p. 051807, 2014.

[96] A. K. K. Wong, Resolution Enhancement Techniques in Optical Lithography, SPIE, 2011.

[97] D. Shelton, G. Boreman and J. D' Archangel, "Metamaterial Composition, Methods, and Application". US Patent 20130052463, 28 2 2013.